Picosecond Infrared Lasers (PIRL): Applications in Biodiagnostics and Towards Quantitative Mass Spectrometry

by

Jing Zou

A thesis submitted in conformity with the requirements
for the degree of Doctor of Philosophy

Department of Physics
University of Toronto

Picosecond Infrared Lasers (PIRL): Applications in Biodiagnostics and Towards Quantitative Mass Spectrometry

Jing Zou

Doctor of Philosophy

Department of Physics
University of Toronto

2016

Abstract

A new concept based on the Picosecond Infrared Laser (PIRL) has been introduced to selectively excite water to directly drive ablation of biological tissue faster than any competing energy dissipation process that could damage surrounding tissue. This thesis work showed that this mechanism can be exploited for a new form of spatially resolved mass spectrometry with the prospect of near instant biodiagnostics with mass spectroscopic sensitivity. The ion source for imaging mass spectrometer was based on PIRL ablation with an electrospray pick up source to entrain the ablated species. This hybrid Picosecond Infrared Laser Assisted Electrospray Ionization (PIR-LAESI) showed a limit of detection of 100 nM and a spatial resolution of ~ 100 μm, limited only by the current focusing optics. The longitudinal spatial resolution is approximately determined by the absorption depth. At the wavelengths of PIRL pulse, the light is absorbed within a few microns at the ablation threshold, resulting in removal of ~ 4 μm thick of material per pulse, which is the size of a single cell. Most importantly no additional treatment was needed as in Matrix Assisted Laser Desorption/Ionization (MALDI). Molecular images using PIR-LAESI for both plant and animal tissues could be collected directly and matched to optical images of the same region. The image quality was compared to nanosecond LAESI versions. Smaller crater size with PIR-LAESI was noted with similar molecular image quality,

indicating PIR-LAESI a more sensitive approach with higher spatial resolution. The question is how far the sensitivity can be improved. In principle, single protein detections is possible if there is no thermal fragmentation as shown in this work. New direct in vacuum sample presentation to mass spectrometry should enable this ultimate limit to single molecular detection, using an electric field for ion separation. Molecular dynamics simulation on the ablation process driven by PIRL on ionic polymer water solutions revealed the effect of electric field cannot be observed in the early stage of plume expansion but that the polymers stay intact with shedding of the water solvation layers. These results illustrate that selective excitation of the water provides the desired ablation physics.

Acknowledgments

Proverbs 20:24

A person's steps are directed by the LORD.

Here I am delighted to express my sincere gratitude to the people who helped me to complete this thesis. Great thanks firstly to my supervisor, Prof. Dwayne Miller, for his supervision, advice and support in every stage of this research. His great patience, passionate motivation and encouragement led me through all the frustrations and stresses. He taught me how to think critically and independently as a scientist. His generous expression of his excitation and happiness in every step I made helped me to establish self-confidence. Dwayne is also very active in networking with people from academic, industry and society, which makes me realize that science is not only the adventure of scientists themselves but of entire communities.

I would like to thank my collaborators Dr. Francis Talbot, Dr. Kresimir Franjic and Dr. Arash Zarrine-Afsar who went through all the challenges and failures with me. They are the happiest scientists that I know and we had a lot of fun in the lab. They passed their expertise (mass spectrometry from Francis, laser engineering from Kresimir, biomedical analysis from Arash) and all the other technical knowledge to me without any reservation. They taught me the most important thing a scientist should know: research is re-search until I find the answer. Francis contributed in making the control program for the lasers and translational stages as well as the molecular map construction program based on the mass spectrum. Kresimir built the water cooling system for the sample plate and Arash supplied animal samples for the tissue imaging experiments. Along with this academic support, they were all my advisers and psychological counsellors during my Ph.D.

Many thanks also given to Dr. Alessandra Tata. She did the molecular imaging of the same animal samples with other technology for comparison. She also contributed a lot in writing our paper.

Members in the machine shop in Department of Chemistry deserve my thousands of thanks, John, Johnny, Dave and Ahmed. The machine shop is the most fabulous one I know. As a

student whose Ph.D needed a lot of instrumentation design, I stepped in their office with problems from time to time and they always gave me the answer with the parts made in super high quality. Without their help, there is no way I could have had a working setup to do the final experiments.

I would also like to express my sincere appreciation to Prof. Leonid Zhigilei and Dr. Chengping Wu at the University of Virginia (UVA) for their support in the molecular dynamics simulation. They wrote the code and taught me how to modify the code to simulate the system of interest. They hosted me warmly during my stay in UVA last summer. We had a very good time together.

I would also like to thank the members of my committee members, Prof. Claudiu Gradinaru and Prof. David McMillen, for their guidance and valuable suggestions during my thesis work. Both of them made my very stressful Ph.D days much easier with their kindness and help.

Almost all of the many current and previous members of Dwayne Miller's research group have helped me by sharing their equipment and skills, and by making the research time enjoyable with laughter and good mood/food. I am grateful to all of them with special thanks to Dr. Gustavo Moriena for his patience and kindness in giving advice with respect to equipment needs and Dr. Etienne Pelletier for his advice in maintaining laser systems in the early stage of this project. A very special thanks to Dr. Wesley Robertson of the German branch of the Miller group for his constant encouragement in the last two years of my Ph.D and his meaningful advice in my thesis content.

I would also like to give thanks to my families in China and my friends in the Toronto Chinese Bible Church. Thanks to my grandfather, Prof. Hualing Zeng in China University of Geosicened for his caring and advising in my academic career. Thanks to Pastor Gong Mingpeng and Pastor Xu Chunping for their spiritual help in leading me to know our Lord and His unfailing love. Thanks to Yali, Lili, Clara, Holly, Lucy, Pauline and Chuling for their spiritual support and prayer in my hardest time.

A special thanks given to my boyfriend Qiaoning Wang. I am so grateful to meet you in my last year of my Ph.D. Even if we are across the Pacific Ocean, your love and word are the sweetest support in my thesis writing and the rest of my life.

Most of all, I would like to thank my parents who walked with me along the way and have always supported my dream. I know being away from you so far and so long brought you a lot of worries and pressure especially when my health had some troubles. I know you missed me greatly. Your unconditional love is the warmest shelter in my life. This thesis is dedicated to you.

It is already a long acknowledgment. But in the end, I still want to give the greatest thanks to my Heavenly Father. Thanks for your unfailing love to me! Thanks for your guidance in my life! Just as it is said in Proverbs 20:24 *A person's steps are directed by the LORD*. You loved me and directed me before I got to know you. You planted the dream in my heart when I was 16 years old ---- contribute my efforts in conquering cancer with laser technology. After so many years you led me to this right place, handed me the right project which matches the dream perfectly and provided all the support I mentioned above. The firm realization that I am on your path and I am in your hands became the final-power to raise me up at moments I wanted to give up. Thanks to God!

Table of Contents

List of Tables

List of Figures

List of Symbols

λ	laser pulse wavelength, m
t_p	laser pulse duration, s
α	penetration depth of laser beam in biological tissue, m
μ_a	tissue's absorption coefficient at incident laser wavelength, m^{-1}
ε	volumetric energy density due to laser energy deposition, J m^{-3}
ε_{th}	threshold ablation volumetric energy density, J m^{-3}
t_d	characteristic thermal diffusion time in biological tissue, s
k	thermal diffusivity of biological tissue, s m^{-2}
t_m	characteristic time of acoustic wave propagation, s
c_a	speed of sound in biological tissue, m s^{-1}
m/z	mass-to-charge ratio of molecules
M^2	quality factor of laser beam
F	irradiation fluence of laser pulse, J m^{-2}
ω_{actual}	radius of laser beam at lens focus, m
f	focal length of the lens, m

ω_0	input beam radius at lens position, m
$E_{p,c}$	intracavity pulse energy, J
$E_{SAT,L}$	gain saturation energy of the laser medium, J
$E_{SAT,A}$	saturation energy of SESAM, J
ΔR	modulation depth
F_r	repetition rate of pulsed laser, Hz
c	Speed of light in vacuum, m s^{-1}
L	total length of laser cavity, m
R_m	curvature radius of cavity mirror, m
ω_p	frequency of pump beam in optical parametric amplifier, Hz
ω_s	frequency of signal beam in optical parametric amplifier, Hz
ω_i	frequency of idler beam in optical parametric amplifier, Hz
T_D	time interval between laser pulse bursts, s
T_t	time interval between laser pulses, s
v	ion velocity inside the flight tube, m s^{-1}
$I.D$	inner diameter of electrospray capillary, m

$O.D$	outer diameter of electrospray capillary, m
x_{s-ms}	horizontal distance between laser focus and entrance of mass spectrometer, m
d_{s-ms}	horizontal distance between laser focus and entrance of mass spectrometer, m
x_{esi-ms}	Horizontal distance between electrospray capillary tip and entrance of mass spectrometer, m
F_{esi}	flow rate of electrospray, $m^3\ s^{-1}$
x_{start}, y_{start}	coordinates of the first pixel on the 2D translational stages
x_{stop}, y_{stop}	coordinates of the last pixel on the 2D translational stages
x_{step}, y_{step}	step size between pixels in 2D tissue imaging experiment
Δm	difference between measured and calculated monoisotopic masses, kg
R_i^0	equilibrium radius of particle *i* describing its breathing motion, m
R_i	instantaneous radius of particle *i* describing its breathing motion, m
d_0	equilibrium distances between the edges of the spherical particles, m
r_{ij}^s	instantaneous distances between the edges of the spherical particles, m
M_I	effective mass ascribed to the breathing degree of freedom, kg
k_1, k_2, k_3	parameters describing the breathing motion of spherical particles

U_R	potentials describing the breathing motion of spherical particles, J
D_e	well depth in Morse potential, J
β	width in Morse potential
r_e	equilibrium bond distance in Morse potential, m
M	mole mass of spherical particles, kg
U_r	Morse potential between spherical particles, J
$\vec{F}_1(r_i)$	forces applied on the translational motion of spherical particles, N
$\vec{F}_1(R)$	forces applied on the breathing motion of spherical particles, N
C^{HB}	heat capacity of heat bath ascribed to a spherical particle, J kg^{-1} K^{-1}
$C^{\exp}$	experimental specific heat capacity of the corresponding particles, J kg^{-1} K^{-1}
C^{TR}	contribution to the heat capacity from three translational degrees of freedom, J kg^{-1} K^{-1}
C^R	contribution to the heat capacity from the radial breathing motion, J kg^{-1} K^{-1}
k_B	Boltzmann constant, m^2 kg s^{-2} K^{-1}
$T_{HB}(i)$	heat bath temperature of particle *i*, K

$T_{BS}(i)$	temperature of the breathing motion of particle *i*, K
A	parameter controlling the energy exchange rate between heat bath and breathing motion
τ	characteristic time of the energy exchange between heat bath and breathing motion, s
$F_R(i)$	"friction" force applied on breathing motion of particle *i* due to energy exchange with heat bath, N
$v_R(i)$	speed of particle *i* describing the breathing motion, m s^{-1}
$\varepsilon(i)$	coefficient of friction force of particle *i*, N kg^{-1} m^{-1} s
ΔE	energy transferred to the breathing motion of particle *i*, J
ΔW	work done by the friction force due to energy transferred to the breathing motion from heat bath, J
ε_{ij}	coefficient of friction force of particle *j* due to energy transferred to the breathing motion of particle *i* from its heat bath, N kg^{-1} m^{-1} s
K_j	kinetic energy of particle *j*, J
E_j	total energy of particle *j*, J
E	strength of applied electric field, V m^{-1}

Chapter 1
Introduction

Soon after the invention of the ruby laser by Maiman in 1960, scientists were eager to examine the potential of pulsed laser radiation for medical applications. It was greatly anticipated that lasers would enable manipulation and destruction of biological tissue with unprecedented precision and selectivity [1][2]. However, after a half century since the birth of the laser, widespread adoption of lasers in surgery is still limited only to specific applications such as laser eye surgery and skin resurfacing. Two main reasons for the slow adoption of surgical lasers are lack of understanding of the fundamental mechanism of laser tissue interaction [3] and the various types of residual tissue damage after laser irradiation [4].

Surgical lasers nowadays are usually in the UV ($\lambda < 300\ nm$) and the IR ($\lambda = 1\sim15\ \mu m$) spectral range, which matches the absorption spectrum of the main molecules that constitute most of biological tissues. UV lasers interact with biological tissues via electronic excitation of molecules' chemical bonds leading to the fragmentation of the absorber molecules. Although they provide very precise cuts there is a concern of potentially dangerous mutagenic cell effects caused by the energetic UV photons since both proteins and DNA strongly absorb in that spectral region [4]. Thus, UV lasers are only limited in corneal surgery where there are no blood vessels thus the chemical risk is only localized in the interaction area and can be tolerated. IR lasers can be tuned to resonate with the vibrational modes of water in tissues ($\lambda = 2.94\ \mu m$). Pulsed IR lasers interact with tissue by triggering a phase transition process in the interaction zone, resulting in collective tissue removal, a process well known as ablation. In pulsed IR laser-tissue interaction, the pulse duration plays the most important role in determining the residual damage in the peripheral tissues. Currently, most commercial IR lasers have pulse durations in the microsecond and nanosecond time scale. The characteristic thermal diffusion time of most biological tissues is in microsecond time scale [3]. Therefore, energy deposited by microsecond IR laser can leak out the interaction zone to the surrounding tissue, resulting in violent thermal damage with the damage zone up to a hundred times larger than the interaction zone. Nanosecond pulsed IR lasers deposit energy much faster than microsecond IR lasers and therefore can drive a fast phase transition process. The pulse duration is less than the thermal

diffusion time, resulting in significant reduction of thermal damage compared to the microsecond IR lasers. The fast phase transition also induces acoustic waves into the biological tissues. The time for the acoustic wave to propagate out the interaction zone is in the nanosecond time scale. For nanosecond IR lasers, the pulse duration is longer or on the same time scale with the acoustic wave propagation time. As a consequence, within the pulse irradiation, pressures built up inside the interaction zone can travel to the surrounding area, resulting in mechanical tearing in the peripheral tissue. The mechanical damage of nanosecond IR lasers limits it from being the ideal choice for surgical lasers. IR lasers with ultrashort pulse duration in femtosecond time scale are also available on the market. However, the extremely high peak intensity of these pulses can easily trigger photo-induced plasma processes, releasing free electrons, which are chemically toxic to the human body. Due to these above mentioned limitations, IR lasers with pulse durations in the picosecond time scale seem to be the ideal choice for both a chemically and physically safe laser scalpel with respect to minimal damage to surrounding tissue. For this reason, the Picosecond IR Laser (PIRL) was developed in our group specifically for minimal invasive surgery based on IR pulses of $\lambda = 2.88\ \mu m$ with pulse durations $t_p \approx 100\ ps$ (*108 ps* more exactly) and tunable repetition rate up to 1 kHz.

The ablation process driven by PIRL is termed Desorption via Impulsive Vibrational Excitation (DIVE). The ablation mechanism of DIVE in pure liquid water has been studied in detail elsewhere [5]. In brief, the DIVE ablation mechanism exploits the direct coupling of the OH stretch mode through the hydrogen bond network of water into the O-O translations, the very motions needed to drive molecules into the gas phase. The energy transferred to O-O translations breaks the hydrogen bond network. Liquid water thus undergoes an explosive phase transition in which nucleation sites involve only a few water molecules. This bit of physics means the phase transition occurs without exponential nucleation growth and associated cavitation driven shockwaves. It is the collapse of nucleation bubbles that lead to massive shockwave damage to adjacent tissue using longer pulses. With picosecond pulses, there simply is no time for nucleation growth prior to the onset of the strongly driven phase transition. The resulting ablated plume leaves the ablation site as a bullet driving the “free” molecules such as proteins out into the gas phase. The impulsive character of DIVE ablation assures all the deposited energy is transferred into the O-O translations to drive ablation and thus DIVE is believed to lead to almost no thermal tissue damage outside the ablated zone. Experiments on porcine skin and mice with

the PIRL laser show minimal tissue ablation with less damage of surrounding tissues compared with microsecond Er:YAG lasers [6] [7]. Furthermore, ablation of biological material by PIRL has been shown to result in no loss of biological activity, as evidenced by recent works suggesting that native enzymatic activity and viral infectivity are retained in the plume of PIRL ablated material[8][9].

Besides the effort in the development of the PIRL scalpel for minimally invasive surgery, surgical guidance technology is also extremely important. Surgeons need to know what is being cut during operation, healthy tissue or tumor, bones or nerves in the case of spinal operation. In the case of brain surgery, the precision of distinguishing healthy and unhealthy brain tissue directly decides the quality of life for the patient after operation. Since the fundamental difference between healthy and unhealthy tissue is their molecular composition, mass spectrometry (MS) as the most sensitive molecular analysis technology becomes the first option for a surgical guidance tool. Till now the greatest success with such a tool is the invention of the iKnife by Dr. Zoltan Takats in Imperial College of London in 2013 [10]. By pumping the burned smoke from the electrocautery needle into a mass spectrometer, surgeons were able to tell for the first time whether there are cancer cells or not in the tissue they just burned during operation. However, the thermal damage of the electrocautery knife is huge and the precision of such a scalpel (several millimeters) is not comparable with laser scalpels. If laser scalpel can also be coupled with mass spectrometer, the development of such in vivo molecular guidance with high precision is not far.

Prof. Vertes in George Washington University invented the first MS interface that can perform imaging of tissue directly using lasers, the first step of developing in vivo laser surgical guidance. The interface is named as Laser Ablation Electrospray Ionization (LAESI) [11]. LAESI utilizes a nanosecond IR laser with $\lambda = 2.94\ \mu m$, pulse duration of sub-10ns and repetition rate of 10 Hz or 20 Hz. The pulse drives ablation of the tissue under investigation and the ablated plume intercepts with an electrospray where molecules in the plume are extracted and ionized by the charged droplets from electrospray. LAESI has shown its success by in situ molecular imaging of plant and brain tissues [12] [13]. Further development is being undertaken to upgrade the interface to be able to do in vivo molecular analysis of the ablated tissue during laser surgery.

The PIRL laser is believed to be the safest laser scalpel with surgical precision down to the single cell level with damage to adjacent tissue confined to a single cell layer and near absence of scar has been reported [14]. As the first step of applying PIRL laser in surgical guidance tool, a MS interface similar as LAESI, named as PIR-LAESI is developed and characterized in this thesis. The first issue is to determine whether PIRL ablation affects the molecular composition of the ablated material. This detail is essential for use in molecular contrast for tissue imaging and ensuring that PIRL really is free from ionization and fragmentation processes that could render the method chemically unsafe. In preliminary experiments, PIR-LAESI shows its ability in performing in situ molecular image experiment in both plant and animal tissues. The results show no loss of sensitivity of PIR-LAESI compared with the conventional nanosecond LAESI interface, especially considering the much smaller interaction zone and thus less abundant ablated tissue per pulse in PIRL. This is very encouraging for the invention of the PIRL scalpel coupled with MS for surgical guidance.

Besides the surgical application of PIRL laser, the unique soft ablation properties of the DIVE process driven by PIRL also provides a new mechanism for the development of a quantitative ion source for mass spectrometry (MS). The deciphering of human genome made us realize that genetic information alone is not enough in order to understand biological processes. To have a fuller understanding, we need to know what molecules are present and in what amount during a biological process. This means we need a technique to measure the molecular composition of a biological sample with high sensitivity and full quantification (we must know what amount of each molecule is in the sample). Currently there are no such technique available to scientists. Because some crucial molecule in a processes can be present in very low amount, it is essential for such technique to have high sensitivity. Mass spectrometry as the most sensitive molecular analysis technique is our best choice for now. The instrument, the mass spectrometer, is composed of two parts: the ion source where molecules from samples get vaporized and ionized and the mass analyzer where ions are separated and detected according to their mass-to-charge ratio (m/z). Thanks to the invention in the 1980’s of the most widely used ion sources today, Electrospray Ionization (ESI) [15] and Matrix Assisted Laser Desorption/Ionization (MALDI) [16][17], for the first time it is possible to measure molecular system of all sizes in mass from atoms to large proteins or even virus. However, ionization in ESI and MALDI are based on protonation or deprotonation of the analytes, where signal suppression is unavoidable. This

problem prevents ESI and MALDI based MS from being quantitative when the sample is composed by more than one molecule, which is unfortunately always the case of biological samples. Due to the great demand for quantitation, researchers have developed a handful of methods to achieve some extent of quantification (e.g., molecular labeling kits). These methods make the sample processing complicated and expensive. Furthermore, they are only limited to certain types of molecules. There are still a lot of efforts aiming to quantify ion sources more generally. At this moment, the discovery of the soft ablation process in DIVE gives us a hope for an inherently quantitative ion source for mass spectrometry. In DIVE, the energy deposition and phase explosion occurs in such a fast timescale that in principle, there should not be enough time for the deposited energy transferred to the proteins and thus the proteins should be desorbed into gas phase intact and relatively much colder compared with any other ablation process. If the protein molecules of interest is neutral in the solution or tissue, they will still be neutral when they are in the gas phase. In principle, there is not enough energy to ionize or fragment them. The neutral and intact gas phase proteins thus are ready for photo-ionization by depositing UV photons onto the electronic excitation to strip free electrons and leave the corresponding radical protein ions ready for MS analysis. Unlike in ESI and MALDI, desorption and ionization processes are decoupled here, which provides the ability to optimize both process independently to achieve 100% desorption and ionization efficiency. However, in most of the cases, proteins exist in native environment with charges attached on the most basic amino acids and counter ions nearby for charge balance. It is quite possible that the counter ions are stripped off during the DIVE ablation process, leaving the desorbed proteins with the charges still attached. Applying an external electric field can prevent the recombination of the counter ions with protein ions during the plume propagation before the protein ions become guided by the ion optics of the mass spectrometer for further analysis. The entire ionization process is deterministic thus should be inherently quantitative. However, to extract information such as how strong the external electric field is needed to prevent recombination requires understanding the DIVE ablation process down to the molecular level. Molecular dynamics calculation was therefore performed on the DIVE process using a charged protein water solution as the system as discussed at the end of this thesis in order to give guidance for the design of quantitative mass spectrometer.

The thesis is organized as follows:

Chapter 2 discusses the background and current status of lasers in surgeries and mass spectrometers in medical application. A brief introduction of the PIRL system and the DIVE process is also given in this chapter.

Chapter 3 describes the design of the PIRL system and the characterization of its performance. The scheme for the PIR-LAESI interface as well as the optimal geometry parameter are also given here.

Chapter 4 characterizes the performance of PIR-LAESI as an imaging mass spectrometer interface. The ablation process of DIVE on different samples are also discussed here.

Chapter 5 presents the experimental results of PIR-LAESI in the molecular imaging of plant tissue and mice kidney tissue. A simple comparison of PIR-LAESI and the conventional nanosecond LAESI also shown here for plant tissues.

Chapter 6 presents the molecular dynamics simulation results of the DIVE ablation process for a model of a charged protein aqueous solution to establish the physics of the ablation process and provide guidelines for the development of a quantitative mass spectrometer.

References of Chapter 1

[1] L. R. Solon, R. Aronson, and G. Gould, “Physiological Implications of Laser Beams,” Science, vol. 134, no. 3489, pp. 1506–1508, Nov. 1961.

[2] M. M. Zaret, G. M. Breinin, H. Schmidt, H. Ripps, I. M. Siegel, and L. R. Solon, “Ocular lesions produced by an optical maser (laser),” Science, vol. 134, no. 3489, pp. 1525–1526, Nov. 1961.

[3] A. Vogel and V. Venugopalan, “Mechanisms of Pulsed Laser Ablation of Biological Tissues,” Chem. Rev., vol. 103, no. 2, pp. 577–644, Feb. 2003.

[4] M. H. Niemz, Laser-Tissue Interactions: Fundamentals and Applications. Springer Science & Business Media, 2007.

[5] K. Franjic and R. J. D. Miller, “Vibrationally excited ultrafast thermodynamic phase transitions at the water/air interface,” Phys. Chem. Chem. Phys., vol. 12, no. 20, pp. 5225–5239, 2010.

[6] N. Jowett, W. Wöllmer, A. M. Mlynarek, P. Wiseman, B. Segal, K. Franjic, P. Krötz, A. Böttcher, R. Knecht, and R. J. D. Miller, “Heat Generation During Ablation of Porcine Skin With Erbium:YAG Laser vs a Novel Picosecond Infrared Laser,” JAMA Otolaryngol. Neck Surg., vol. 139, no. 8, p. 828, Aug. 2013.

[7] S. Amini-Nik, D. Kraemer, M. L. Cowan, K. Gunaratne, P. Nadesan, B. A. Alman, and R. J. D. Miller, “Ultrafast Mid-IR Laser Scalpel: Protein Signals of the Fundamental Limits to Minimally Invasive Surgery,” PLoS ONE, vol. 5, no. 9, p. e13053, Sep. 2010.

[8] M. Kwiatkowski, M. Wurlitzer, M. Omidi, L. Ren, S. Kruber, R. Nimer, W. D. Robertson, A. Horst, R. J. D. Miller, and H. Schlüter, “Ultrafast extraction of proteins from tissues using desorption by impulsive vibrational excitation,” Angew. Chem. Int. Ed Engl., vol. 54, no. 1, pp. 285–288, Jan. 2015.

[9] L. Ren, W. D. Robertson, R. Reimer, C. Heinze, C. Schneider, D. Eggert, P. Truschow, N.-O. Hansen, P. Kroetz, J. Zou, and R. J. D. Miller, “Towards instantaneous cellular level bio diagnosis: laser extraction and imaging of biological entities with conserved integrity and activity,” Nanotechnology, vol. 26, no. 28, p. 284001, Jul. 2015.

[10] J. Balog, L. Sasi-Szabó, J. Kinross, M. R. Lewis, L. J. Muirhead, K. Veselkov, R. Mirnezami, B. Dezső, L. Damjanovich, A. Darzi, J. K. Nicholson, and Z. Takáts, “Intraoperative tissue identification using rapid evaporative ionization mass spectrometry,” Sci. Transl. Med., vol. 5, no. 194, p. 194ra93, Jul. 2013.

[11] P. Nemes and A. Vertes, “Laser Ablation Electrospray Ionization for Atmospheric Pressure, in Vivo, and Imaging Mass Spectrometry,” Anal. Chem., vol. 79, no. 21, pp. 8098–8106, Nov. 2007.

[12] P. Nemes, A. A. Barton, Y. Li, and A. Vertes, “Ambient Molecular Imaging and Depth Profiling of Live Tissue by Infrared Laser Ablation Electrospray Ionization Mass Spectrometry,” Anal. Chem., vol. 80, no. 12, pp. 4575–4582, Jun. 2008.

[13] P. Nemes, A. S. Woods, and A. Vertes, “Simultaneous Imaging of Small Metabolites and Lipids in Rat Brain Tissues at Atmospheric Pressure by Laser Ablation Electrospray Ionization Mass Spectrometry,” Anal. Chem., vol. 82, no. 3, pp. 982–988, Feb. 2010.

[14] M. Hess, M. D. Hildebrandt, F. Müller, S. Kruber, P. Kroetz, U. Schumacher, R. Reimer, M. Kammal, K. Püschel, W. Wöllmer, and D. Miller, “Picosecond infrared laser (PIRL): an ideal phonomicrosurgical laser?,” Eur. Arch. Otorhinolaryngol., vol. 270, no. 11, pp. 2927–2937, Nov. 2013.

[15] J. B. Fenn, M. Mann, C. K. Meng, S. F. Wong, and C. M. Whitehouse, “Electrospray ionization for mass spectrometry of large biomolecules,” Science, vol. 246, no. 4926, pp. 64–71, Oct. 1989.

[16] M. Karas, D. Bachmann, U. Bahr, and F. Hillenkamp, “MATRIX-ASSISTED ULTRAVIOLET-LASER DESORPTION OF NONVOLATILE COMPOUNDS,” Int. J. MASS Spectrom. ION Process., vol. 78, pp. 53–68, Sep. 1987.

[17] K. Tanaka, H. Waki, Y. Ido, S. Akita, Y. Yoshida, T. Yoshida, and T. Matsuo, “Protein and polymer analyses up to m/z 100 000 by laser ionization time-of-flight mass spectrometry,” Rapid Commun. Mass Spectrom., vol. 2, no. 8, pp. 151–153, Aug. 1988.

[18] “The top 10 leading causes of death in the US,” Medical News Today. [Online]. Available: http://www.medicalnewstoday.com/articles/282929.php. [Accessed: 15-Aug-2015].

Chapter 2
Surgical Application of Lasers and Mass Spectrometer

2.1 Application of Lasers in Surgery

The laser was greatly appreciated immediately after its invention to have the ability of manipulation and destruction of biological tissue with unprecedented precision and selectivity through control of the laser spectrum in relation to the absorption properties of the targeted tissue [1][2]. The non-contact approach of cutting tissues minimized the surgical tools that needed to be sterilized and the risk of infection to the patients from the surgical scalpel relative to traditional surgery process. Besides, laser surgery can achieve single cell precision in principle, the fundamental resolution limit to a surgical process. However, despite this great promise, widespread adoption of lasers in surgery has been limited only to a few specific applications like laser eye surgery and skin resurfacing. There are several reasons for the slow adoption of surgical lasers. First, biological tissue is a complicated system to study itself, which together with the dynamic variation in its properties with respect to response to laser irradiation makes the fundamental mechanism of laser tissue ablation a complex problem to work on. Second, even with great progress in understanding the ablation mechanism in the past two decades, current laser surgery techniques still suffer from various types of residual tissue damage making these techniques attractive only if such damage can be tolerated and if such damage is smaller compared to alternative techniques. In this section, a review on the laser tissue ablation mechanism based on Ref [3] and the tissue damage induced by various surgical lasers will be summarized [3][4].

Surgical lasers currently are usually in the UV ($\lambda < 300\ nm$) and the IR ($\lambda = 1\sim15\ \mu m$) spectral range. This is due to the absorption peak of the main molecules that constitute most of biological tissues lie in these ranges, as indicated in Figure 2.1.1. By mass, most soft tissue is dominated by water (65-99%) and collagen (0-35%) and the rest is mainly cell adhesive proteins. Laser irradiation usually interacts with tissue via photothermal, photomechanical, photochemical, photon induced plasma process or a combination of them [5]. Laser parameters such as wavelength, pulse duration, irradiation fluence, repetition rate, as well as the interacting tissue's

optical, mechanical and thermal properties define the mechanism in the ablation process and thus the surgical precision as well as the source and extent of tissue damage. Continuous wave lasers are out of the discussion here due to the severe thermal damage.

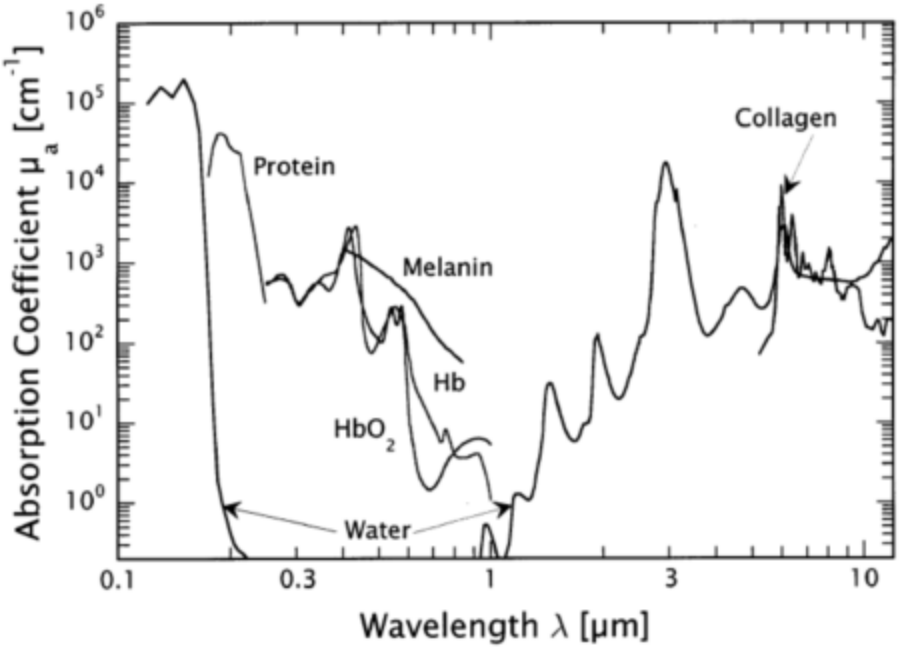

Figure 2.1.1 Absorption spectrum of the main molecules in biological systems. Reprinted with permission from ref. [3]. Copyright © 2003 American Chemical Society.

Precision of the laser surgery is mainly determined by the thickness of the removed layers per pulse, which relates to the penetration depth of the laser beam in the tissue $\alpha = 1/\mu_a$, where μ_a is the absorption coefficient [3]. The absorption coefficient depends on the laser wavelength as shown in Figure 2.1.1. For UV and IR wavelength with μ_a > *10000 cm*$^{-1}$, the penetration depth is on the order of ~ 1 μm which is comparable to the wavelength of light used. Thus light scattering can be ignored. Laser pulses in the visible to near-IR range experience very low absorption and deep penetration depth inside the tissue with far too excessive energy needed to achieve ablation thresholds for such large volumes. These wavelengths are out of the scope of discussion here. In pulsed laser tissue ablation, the interaction zone is the volume confined by the irradiation area and the penetration depth [3]. The energy deposited by the laser pulse is firstly confined within this zone to drive the ablation process. For a given penetration depth, the irradiation fluence determines the volumetric energy density ε deposited in the confined volume. The minimum volumetric energy density required for ablation is called the threshold ablation

energy density ε_{th}. In principle. ε_{th} is the energy required for complete vaporization of the materials inside the confined volume. However, it is not always the case since processes such as thermal dissipation also consume some of the deposited energy, or in the case of mechanically weak tissues ablation occurs without complete vaporization of the material, as will be discussed below. In general, lower threshold ablation energy density ε_{th} means less thermal damage. If all the deposited energy is consumed in completely vaporizing the material inside the confined volume, no energy is left to damage the peripheral tissue. However, it is difficult to achieve this ideal case because the absorption of the irradiation in the rising and falling edges of the spatial profile of the absorbed laser pulse where the fluence is below the ablation threshold is unavoidable, as well as the propagation of acoustic wave from the confined volume to the rest of the tissue [4].

Besides the tissues physical and chemical properties, pulse duration of the laser sources plays the most important role in the laser-tissue interaction process. Laser-tissue ablation can be characterized in two regimes: thermal confinement and stress confinement, depending on the pulse duration compared with the time for heat dissipating out of the confined volume via thermal diffusion or the time for acoustic wave propagating out of the confined volume. The characteristic thermal diffusion time is given by $t_d = 1/k\mu_a$, where k is the thermal diffusivity [3]. When pulse duration t_p is comparable to the characteristic thermal diffusion time $t_p / t_d \le 1$, the deposited energy is mainly localized inside the confined volume during the laser irradiation, and this regime of ablation is called thermal confinement. The characteristic thermal diffusion time in biological tissue is usually on time scale of a few μs. Laser-tissue interactions with pulse durations longer than t_d will result in a larger thermal damage zone than the heated volume and thus not the optimal option for most medical applications [3]. The fast energy deposition process by pulsed laser radiation also induces acoustic waves, which originate from the pressure build-up within the confined volume due to the phase transition of the material. Stress confinement is thus achieved when the pulse duration is comparable to the characteristic time for the acoustic wave to propagate across the heated volume, which is defined by $t_m = 1/\mu_a c_a$, where c_a is the speed of sound in the medium. Experimental measurement of the acoustic wave found on this time scale is a few ns to a few tens of ns in most biological tissue. Laser-tissue interaction with pulse duration $t_p / t_m \le 1$ is defined as in the stress confinement regime. Ablation in the stress

confinement regime can reduce the ablation threshold and thus minimize the thermal damage of the tissue to some extent. This is because the pressure built up in the confined volume weakens the mechanical strength of the tissue resulting in material fractionation into small particulates that are ejected by recoil. Particulates or clusters thus dominates in the ablated plume for the ablation in this regime [3]. Depending on the clinical purpose of medical application, lasers with different parameters can be selected to achieve the best precision and minimum damage to the peripheral tissues.

UV lasers possess the best precision among all the available lasers due to the high absorption coefficient (μ_a ~ 20000 cm^{-1}) of biological tissues in this range, resulting in a penetration depth μ_a less than 1 μm. In addition, smaller beam diameter is more readily achievable with convenient working distances. Commercial UV lasers cover the spectral range from 190 ~355 nm. The main chromophore in the UV range is the peptide bond (O=C-N-H) present in the backbone of all proteins (λ = *190 nm*) and the aromatic nucleotide bases in DNA (λ = *280 nm*). UV lasers interact with biological tissue mainly via photochemical processes interplaying with photothermal processes. The photon energy is first deposited in the peptide bond via electronic excitation, leading ultimately to chemical bond cleavage in proteins, or in the case of aromatic absorption in aromatic groups and ionization potential mutation in DNA [5]. The deposited energy will also transfer to the neighboring tissue molecules like water via intermolecule interactions, resulting in photothermal processes. If the UV pulse duration is in sub-100 ns range, the thermal damage to the residual tissue is negligible since the ablation is in the thermal confinement regime. Further, photomechanical damage can also be neglected in UV laser-tissue interaction. This is because the fragmentation of the absorbing molecules breaks up the solid properties of the tissue inside the irradiation zone, resulting in a ‘fluid’ like tissue and thus the acoustic wave is attenuated if not reflected when it propagates to the solid like peripheral tissue. Even with the advantage of high precision and almost no physical damage, the potential chemical risk can never be neglected when applying UV lasers in clinical treatment. The free peptide or amino acid residues from the cleavage of the absorber molecule may activate chemical process that can generate toxic products. Moreover, the mutation of DNA increases the probability of tumor development because the biological process is highly nonlinear and only a few mutated DNA sites are enough to trigger tumor growing processes. Due to the long development period from the state of a few mutated DNA to detectable tumor (up to several

years), it is difficult to completely rule out this risk in using UV laser sources. Based on the above discussion, UV lasers are limited in their application only primarily to corneal surgery where there are no blood vessels in the tissue thus the chemical risk is only localized in the interaction area and can be tolerated, especially when compared with the benefits of high precision and minimum physical damage.

Current IR lasers in medical use are mainly CO_2 lasers ($\lambda = 10.6\ \mu m$) with pulse duration of sub-100 ns, Q-switched Er:YAG or Nd:YAG pumped OPO (Optical Parametric Oscillators) ($\lambda = 2.94\ \mu m$) and Q-switched Er:YSGG ($\lambda = 2.79\ \mu m$) with pulse duration for the Q-switched laser in sub-100ns and the OPO sub-10ns. Tissue ablation driven by these lasers are in the thermal confinement regime, but not always in stress confinement regime depending on the type of ablated tissue. In most cases, the target chromophore is the tissue's water which has the lowest phase transition temperature and undergoes phase explosions for short pulsed irradiation. The hot pressurized water vapor fractures the tissue and leads to ablation. Thus, the ablation threshold of these lasers is at least the sum of enthalpic and latent energy required to complete the vaporization process of water in tissue. Despite the energy needed for phase transitions, intermolecular interactions between tissue water and other tissue molecules like collagen or proteins can also take up some of the deposited energy, which further increases the ablation threshold and leads to thermal damage to the peripheral tissue. This intermolecular interaction occurs on a time scale of a few tens of picoseconds thus lasers with pulse durations in the nanosecond timescale are not short enough to avoid the thermal damage from intermolecular interactions. Typically these lasers have ablation precision of a few μm but the thermal damage zone can be as deep as a few hundred microns depending on the pulse duration and tissue type. Only in some rare cases is the thermal damage desired. For example, surgery with CO_2 lasers usually has less bleeding from the patient because the thermal damage of the vessel tissue minimizes or even ceases the blood flow due to burning of the tissue and cauterization, resulting in a clearer view of the unhealthy tissue for the surgeon. Since thermal accumulation can further enlarge the damage zone, laser scalpels of ns pulses usually operate at low repetition rate (< 50 Hz) which decreases the tissue removal rate and prolongs duration of the surgery.

Laser scalpels with pulse durations in the femtosecond time scale have attracted a lot of attention recently because they possess the outstanding ability of ablating tissues that are transparent at low irradiance or covered by layers of transparent tissues at the irradiation wavelength. They

have been used in intraocular surgery [6] and intracellular surgery [7]. The high peak power of femtosecond laser triggers the multiphoton ionization process releasing energetic free electrons which serve as seed electrons of avalanching ionization in the tissue. The degree of disruption and the amount of mechanical peripheral damage is determined by the plasma energy density. Energy gained by the electrons is transferred to heavy plasma particles through collision and recombination which occurs on the time scale of several tens of picoseconds, resulting in a heating of the atomic and ionic plasma constituents. At constant electron density, the number of collisions and recombination events is proportional to the pulse duration, and therefore plasma energy density. Since the pulse duration of femtosecond lasers is shorter than the collision and recombination time scale, there is no energy transfer within the pulse duration and the ablation is only driven by the heating of the plasma, which occurs after the pulse irradiation. Thus, almost all the energy is consumed in the ablation plume with minimal energy left behind in the vicinity of the laser focus. Hence, the femtosecond laser scalpel provides almost no damage and extremely high precision in surgery. However, since plasmas are only generated at the focal point of the laser, the position of the focal point must be carefully controlled to avoid plasma generation in healthy tissue when the operation is not on tissues with exposed surfaces to the air [3]. Furthermore, a few studies have indicated that the generated plasma may cause biochemical damage to surrounding cells by creating transient molecular species that could be reactive and toxic free radicals [8].

In general, IR lasers, especially mid-IR of $\lambda \sim 2940\ nm$ are chemically safer than UV lasers and femtosecond lasers because the wavelength is resonant with the vibrational modes of water molecules. The nanosecond time scale pulse duration of commercial lasers in this spectral range makes the thermal damage the main limitation for the application of these lasers. Telfair and co-workers [9] have reported a small thermal damage zone produced with Nd:YAG OPO ($t_p = 6\ ns$) that is even comparable to the UV ArF excimer laser used for corneas. Vogel and Venugopalan attribute this as a consequence of some degree of stress confinement ablation ($t_p / t_m = 6$) [3]. For other tissues rather than cornea, stress confinement with $t_p / t_m < 1$ is required to achieve such a small damage zone. This requires the pulse duration of $\lambda \sim 2940\ nm$ pulse to be in the picosecond time scale. Picosecond-InfraRed-Lasers (PIRL) developed by our group can generate such pulses with pulse duration of 100 ps or less. The ablation process driven by PIRL lasers is called

Desorption via Impulsive Vibrational Excitation (DIVE), which will be discussed in detail in Section 2.3 whereas the PIRL system will be illustrated part by part in Chapter 3.

Before closing this section, a short review of the various surgical guidance systems for laser scalpels are presented here to pave the way to the discussion of medical applications and required sampling sources for mass spectrometers in the next section. When the removal of tissue layers that exhibit pathologic changes from underlying healthy tissue is desired, or when a sensitive tissue structure adjacent to the target structure must be protected (for example, neural tissue in microspinal surgery), it is necessary to confine the ablation to the target structure. Online monitoring and active feedback techniques were introduced for this purpose to discriminate between different tissue types and to automatically stop the ablation procedure when the transition between the layers is reached. Such techniques include the analysis of acoustic transients in air generated during ablation, fluorescence spectroscopy and plasma spectroscopy to distinguish between bone and nerve tissue, etc. [3]. The precise removal of cancerous tissue from healthy tissue directly determines the patient's quality of life after surgery. The online feedback techniques mentioned above are not sensitive and reliable enough for the surgeons to distinguish cancerous tissue from healthy tissue. This is because in most of the cases, cancerous tissue possesses quite similar physical properties as the healthy tissue for the aforementioned surgical guidance technologies to distinguish. In most circumstances, the only difference between cancerous tissue and healthy tissue is their fundamental chemical composition, which can only be analyzed with a chemical analytical tool. Mass spectrometers as the most sensitive analytical instrument become the only possible general solution. In the next section, a brief review of the mass spectrometer technology and its status with respect to applications for surgical guidance will be summarized.

2.2 Mass Spectrometer and Its Medical Application

Soon after the human genome had been sequenced [8], it was realized that phenotypic expression and cell differentiation cannot be determined by the genome alone. It is actually the proteins and their actions that are responsible for the functional diversity of cells, and it is proteins that perform most biological processes [10]. A new research branch to decipher the cell proteome thus came out in the last two decades and is concerned with determining the set of all expressed cell proteins at a given time under defined conditions [11]. The field of biology that attempts to

accomplish complete qualitative and quantitative characterization and understanding of an organism's proteome and its dynamics under various conditions is called proteomics. Proteomics research represents a much more complex endeavor for researchers due to the complicated biological processes involved. While genomes have a fixed structure characterized with a sequence of only ~20,000 genes, the cell proteome is a highly dynamic system consisting of several millions of proteins whose concentrations and forms are constantly changing in time and space due to mutual interactions and environmental influence. Moreover, the concentrations of different proteins cover a huge dynamic range of $\sim 10^{10}$, where proteins in small concentrations may have disproportionally important influence through various metabolic pathways. Though these facts are not the entire picture of the role that proteins play in life processes, they are enough to illustrate how arduous the task is to do proteomics studies of biological systems. Yet, the understanding and characterization of the proteome and its dynamics are essential for understanding the processes of life needed to cure and prevent almost all diseases. Such studies require ultrasensitive detection approaching the detection sensitivity in the order of a few hundred molecules or even one single molecule -- the ultimate detection limit in biological analysis.

Apart from the study of mechanisms involved in disease developing processes, finding a biomarker for a certain disease as an early diagnostic strategy is another research topic that needs an urgent break through, especially when cancer has become the second leading cause of death in the USA according to the latest survey in June 2015 [12]. In principle, biomarkers can be any variable describing a biological process that differentiates the healthy biological system from a disease developing system. It may not only be the difference in molecular composition, but also the concentration of targeted molecules. Given that proteins are the biological endpoints that control most biological processes, it is not surprising that proteins have gained the most attention as potential biomarkers. However, despite the intensified interest and tens of thousands of publications in the past 30 years about cancerous protein biomarkers, only over 20 of these biomarkers are confirmed by the Food and Drug Administration (FDA) of the USA [13] [14] at the present time. One of the reasons is the lack of a reproducible quantitative analytical method, which has led to the relatively high false-positive rate of cancer detection [14]. To break the bottleneck in biomarker identification, reliable analytical tools that can provide quantitative molecular analysis from biological systems with complex molecular composition are necessary.

Over the last two decades, mass spectrometry has become a ubiquitous tool in the structural and composition analysis of biochemical samples. The mass spectrometer is an instrument that can provide the mass-to-charge ratios (*m/z*) of all the analytes placed in the instrument. It is mainly composed of an ion source, mass separator, and ion detector. The data is analyzed by software to generate a mass spectrum, which is the ion count distribution along the *m/z* axis. With the proven technique in mass separation and ion detection, the performance of modern mass spectrometers mainly depends on the ion source, where neutral molecules are ionized and collected. In the first few decades after the invention of the mass spectrometer, the technique was only limited to the analysis of volatile molecules because they are easier to ionize. In the 1980s, Fenn and coworkers invented ElectroSpray Ionization (ESI) [15] that is capable of ionizing large molecules like proteins upto a few hundred kDa. At the same time, Karas and Hillenkamp invented another ionization method, Matrix Assistant Laser Desorption/Ionization (MALDI) [16], that can also ionize large molecules but in vacuum. There can never be overestimation of the importance of their inventions to present research as they opened the door to the study of the most important molecules in our life -- proteins. Although the ionization mechanism of ESI and MALDI is still under debate in the mass spectrometry community 30 years after their invention, it never holds back the fast adoption of application for the instruments in bio-medical research. Commercial mass spectrometers usually can provide a detection sensitivity of attomoles and an ultra-sensitive mass spectrometer is also reported in the literature possessing zeptomole sensitivity, that is, only a few hundreds of molecules [17].

Current proteomics studies are mainly mass spectrometer based for its high sensitivity and capability of protein analysis. Ionization of large molecules includes two processes: (1) desorption, i.e., moving the molecules of interest from the condensed phase into the gas phase, and (2) ionization. Generally, both of these processes represent significant challenges since any excess energy that is put into system to initiate either process can easily lead to fragmentation or unwanted modifications of large proteins and their complexes. Additionally, it is desirable to obtain high reproducibility as well as relative and absolute quantitative capabilities. As the two most commonly used ion sources, both ESI and MALDI are only partially quantitative in their basic forms due to the chemical nature of the ionization processes and also the coupled ionization and desorption process. In both ESI and MALDI , analytes get ionized by protonation or deprotonation, which makes the quantitative analysis of

complex biomolecules challenging [18]. Such ionization inherently suffers from ion suppression when some abundant chemicals like salts are present, completely obliterating the signal from other analytes. While ESI generates multiply charged species, MALDI mostly produces singly-charged protonated and deprotonated ions which enables a simpler and less ambiguous mass spectral interpretation. Nonetheless, the technique also suffers from signal suppression and has issues of its own such as low shot-to-shot reproducibility, and strong dependence on the sample preparation method [18].

Despite these drawbacks and disadvantages, ESI and MALDI based mass spectrometers are fast expanding their applications in research facilities, hospital work and industries. There are also applications of mass spectrometers in clinic for either in vitro or in vivo work. Among the in vitro applications, Imaging Mass Spectrometry (IMS) technology has been developed to construct 2D or 3D molecular distributions -- molecular map, of the biological tissue. Moreover, if the ion source is under ambient condition, IMS can also be an in vivo instruments by coupling into surgical tools to provide molecular guidance to surgeons on what tissue he/she is cutting, healthy or unhealthy. Thus, IMS has drawn intensive attention in the past decades so that over ten different ion sources has had their own IMS version [19], among which Desorption Electrospray Ionization (DESI) [20] [21], Laser Ablation Electrospray Ionization (LAESI) [22] and MALDI dominate the research [23].

MALDI is mostly a vacuum based ion source that can singly ionize large molecules. In MALDI, analyte molecules are first mixed with some matrix material and are deposited on a metal plate. Pulsed laser irradiation of the sample ablates and desorbs the analytes and matrix material. The analytes are ionized by protonation or deprotonation processes in the hot ablated plume. Despite the chemical ionization character, matrix-dependent features further limit MALDI's quantification ability because some molecules are ionized better with certain matrix materials while others are not [24]. The complicated sample preparation process in MALDI is another factor that limits it from becoming a general analytical tool. The lasers used in MALDI can be either UV or IR, usually depending on the matrix material in use. MALDI-IMS has shown the ability to image MRI contrast agents in mouse liver [25] and tumor margins in renal carcinoma [26] etc.

The vacuum-based feature of MALDI limits its application only in ionizing non-volatile molecules. To overcome this bottleneck, Atmospheric Pressure （AP）-MALDI was invented in 2000 by Laiko, etc. [27]. In AP-MALDI, the transfer of the ions from the atmospheric pressure ionization region to the high vacuum is pneumatically assisted by a stream of nitrogen. Sample preparation is identical to that for conventional vacuum MALDI and uses the same matrix compounds. The limit of detection of AP-MALDI is in the low femtomole range. Peptides spectrum from AP-MALDI with much less fragmentation indicates that AP-MALDI is a softer ionization source than vacuum MALDI. This is due to the rapid thermalization of the ions by collision with ambient gas before fragmentation can occur [28]. The soft ionization character of AP-MALDI can significantly simplify the spectrum when analyzing complex samples such as biological tissues. Thus imaging mass spectrometry based on AP-MALDI has been well developed [29] and a fair amount of molecular images from different biological tissues has been studied [30] [31]. Sample consumption of AP-MALDI is usually higher than that for conventional vacuum MALDI, as the transfer of ions into the vacuum system from the ambient environment is relatively inefficient. AP-MALDI ion source nowadays has been commercialized by MessTech (www.apmaldi.com) and the exchange of such an ion source with other atmospheric ion source such as ESI can be done in a few minutes. However, as for the conventional vacuum MALDI, the complexity of sample preparation is still a limit factor for the application of AP-MALDI. Especially when using AP-MALDI as an image mass spectrometry ion source, the sample preparation time can range from hour to days in order to get a meaningful molecular image [32] [33]. Thus, though AP-MALDI is a more versatile ion source compared with conventional MALDI, significant simplification of the sample preparation procedure is still in need to extend its application as an in vivo surgical guidance tool.

ESI is an ion source where ionization occurs under room temperature at atmospheric pressure. The mechanism of ESI will be discussed in detail together with LAESI in Chapter 3. Briefly speaking, in ESI, solutions containing the analyte molecules flow through a capillary with high voltage applied, which charges the droplets that spray out of the capillary. The charged droplets shrink to charged molecules via a cascade of solvent evaporation and coulomb explosion processes. Both DESI and LAESI are ESI based IMS ion sources. In DESI [21], the ESI occurs a few millimeters above the sample surface so that the mist of charged droplets splashes out the molecules on the surface. The analyte on the surface thus are carried out and ionized by the ESI

droplets and then collected by the mass spectrometer. If the sample is placed on translational stages, it is easy to perform a 2D scan of the sample surface to construct a molecular map. The spatial resolution of DESI is usually a few hundred μm but can be improved to ~40 μm under certain conditions. DESI has been used to construct the lipid map of rat brain sections [34] and identify human brain tumors [35], breast cancer [36] as well as capabilities for intraoperative molecular guidance [37]. However, without a laser involved in DESI, it can only serve as an analytic tool, not as a scalpel. Other drawbacks include the high voltage applied very close to the patient and the introduction of chemicals into the human body such as methanol, acid etc.

LAESI in contrast is an ion source where a pulsed laser irradiates the sample surface, driving the ablation process. The ablated plume carries the molecules from the tissue and intercepts with the mist of charged droplets from electrospray. The charged droplets solvate and ionize the analyte molecules in the plume and the cascade ESI process continues until protonated/deprotonated analyte ions form. LAESI has been first successfully demonstrated in imaging plant tissues [22] and then extended its application to animal tissues, including rat brain [38] and living fish [39]. Attempts of converting LAESI to an in vivo analysis tool has also been made this year [40]. The laser used in LAESI is a Nd:YAG pumped OPO with $\lambda = 2.94\ \mu m$, pulse duration below 10ns and repetition rate of 10 ~ 20 Hz, which can serve as laser scalpel while being part of the ion source. Another advantage of LAESI over DESI is that the distance between the electrospray and the sample surface can be on centimeter scale which makes LAESI a safer IMS interface. The spatial resolution of LAESI is on the order of ~ 300 μm limited by the beam quality of the OPO.

To give a general picture of how important the feature of LAESI as a laser scalpel and analytical tool at the same time is, it is worth taking a look at the impact and success of the iKnife. In 2013, Dr. Zoltan Takats in Imperial College of London announced their innovation of iKnife, which is a mass spectrometer coupled with surgical electric cautery [41]. Inserting the cautery needle into a tube which is connected with a vacuum pump, the smoke from the burning tissue can be sucked out and delivered in front of the mass spectrometer for ionization and analysis. To surgeons, this looks like they have a nose to smell what they are burning during operation. The smoke is actually chemical products of the molecules within the tissue being cut during the burning process and even these combustion products are able to help the surgeons to find the margins of tumor/healthy tissues. Despite the precision of electric cautery in cutting tissues in the order of millimeters, the thermal damage to the peripheral healthy tissue is huge since the electric cautery

cuts the tissue via a burning process. Even so, there is general excitement over the innovation of iKnife to the point that the reports have spread out in the mass media including the BBC [42]. Only one year later, one of the largest mass spectrometer companies, Waters, started the commercialization of iKnife in 2014 [43]. One can image how big the impact will be if the ablated plume from laser scalpels can be "smelled" by a mass spectrometer with much better surgical precision and much less thermal damage, needless to say the molecules detected by the mass spectrometer are the original molecules in the tissue rather than the chemical products from some chemical reaction such as burning as in iKnife. LAESI is believed to be the only promising technique till now to achieve this ambitious goal.

As discussed in the previous section, the sub-10ns pulse duration of the mid-IR lasers used in LAESI is still too long to drive an ablation process in the stress confinement regime. To increase ionization efficiency, it requires the ablation process to desorb also as many molecules into the gas phase as possible whereas in most of the cases in stress confinement ablation, the ablation threshold is less than the energy needed to completely vaporize the ablated tissue resulting in ejection of particulates. The lateral precision of scalpels with the laser that is used in LAESI is limited to a few hundred of μm by the beam quality of the OPO. To overcome these drawbacks, an ablation mechanism that provides more vaporization efficiency with the least energy deposited to the analyte molecules as possible is desired to keep the marker proteins in their native states. It also requires that the lasers driving the ablation process have better beam quality so they can be easily focused down to ~ 10 μm which is the size of a single cell in most biological systems, the ultimate precision that a surgical scalpel can reach. The Picosecond Infra-Red Laser (PIRL) developed in our group has a beam quality close to diffraction limit, i.e., $M^2 = 1$ and can drive the ablation process called Desorption via Impulsive Vibrational Excitation (DIVE). This mechanism is believed to be the softest and most efficient ablation process to bring biological molecules such as proteins into gas phase.

2.3 Picosecond Infrared Laser (PIRL) and Desorption via Impulsive Vibrational Excitation (DIVE)

As discussed above, IR lasers operating at $\lambda = 2.94\ \mu m$ are the most chemically safe option for a laser scalpel. However, if the energy is not deposited into water molecules fast enough, there are still chances for the energy to be transferred into proteins via intermolecular interaction. This

extra energy may not result in protein fragmentation, but it can be enough to change the proteins' conformation state [44]. Since the proteins function is highly related to its conformation states, it is better to keep the conformation states of proteins during ablation/ionization to prevent the releasing of proteins with wrong conformation states entering into biological functioning process, which could lead to disease development process. The time scale of protein conformational change is on longer time scales than PIRL, from milliseconds to seconds but recent 2D-IR vibrational spectroscopy study observed the fast switch between two conformational states on 50 ps time scale [45] and the time scale for the energy diffusion via intermolecular interaction is on the order of picoseconds to a few tens of picoseconds [3]. The pulse duration for IR lasers is better if it is longer than the picosecond timescale of intermolecular interactions for efficient thermalization of the deposited energy in the entire excited volume but the pulse duration ideally should be shorter than the timescale of protein conformation switching. Thus nanosecond Nd:YAG OPO used in current LAESI interface is still too long. Besides, nanosecond lasers cannot drive ablation processes that are in the stress confinement regime for most biological tissues. Stress confinement is a necessary requirement to minimize the physical injury in the peripheral tissues. Reducing the pulse duration of IR lasers is the only approach to satisfy these requirements.

In addition to the requirement of high precision laser scalpels with the least chemical and physical side effect as possible, there is an equally important requirement for IR lasers with shorter pulse durations for the design of quantitative mass spectrometers which are urgently needed by the proteomics community. The ion source must possess close to 100% efficiency in desorption and ionization of proteins. Desorption and ionization processes also need to be decoupled so we can control the two processes separately. This requires that the ablation mechanism is capable of bringing the proteins from its condensed state to the gas phase intact and ideally capable of being post-ionized afterward. In the case salt adduction ions of proteins, the ablation process is soft enough to bring the protein salt adduction ions into gas phase but vigorous enough to stripe off counter ions and prevent the recombination of protein ions with counter ions. Ablation process driven by PIRL pulse make the design of such an ion source possible as will be discussed below.

Based on these reasons and due to the photo-plasma effect for femtosecond lasers, IR lasers with picosecond pulse duration seems the only options for laser scalpels for both chemical and

physical safe operation. It should be further noted that pulses on the picosecond timescale also avoid explosive nucleation growth and associated cavitation induced shock waves that are very damaging to surrounding material/tissue. Picosecond Infrared Laser (PIRL) was thus developed in our lab, and the ablation process driven by PIRL was previously studied by Dr. Kresimir Franjic for a simple liquid water system. This work focused primarily on the physics of the coupling of the selective deposition of the energy into water molecules and ensuring ultrafast phase transition leading to ablation. The ablation process was coined Desorption via Impulsive Vibrational Excitation (DIVE) in this work.

This present thesis work extends PIRL applications to spatial imaging of tissue under in vitro conditions. This work required extensive modification of the laser and optical systems as well as studies of the DIVE mechanism for such highly heterogeneous systems. The specific PIRL system used in this thesis work will be illustrated part by part in Chapter 3. Here I only present a brief review of the DIVE process and PIRL application in surgery. In so far as it is relevant to complement the above review of conventional physics for ablation.

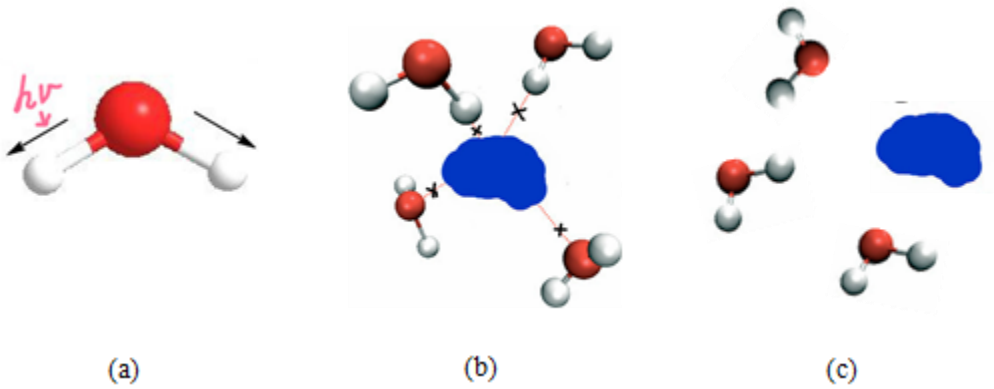

Figure 2.3.1 Scheme of ablation process in DIVE.

Figure 2.3.1 illustrates the ablation process of DIVE. PIRL pulses drive the ablation by depositing the energy into the OH symmetric stretching mode of water molecules, which lie in the 3 μm vicinity in the spectrum (Figure 2.3.1 (a)). In order to give rise to ablation, the absorbed laser energy must ultimately be transduced into translation motions. The DIVE ablation mechanism exploits the effectively direct coupling of the OH stretch mode through the hydrogen bond network of water into the O-O translation, the very motions needed to drive molecules into the gas phase（Figure 2.3.1 (b)）. The previous study of the dynamics of hydrogen bonding

network of liquid water reveals the relaxation time from the individual excited OH stretching mode to its coupled O-O translational mode is about 200 fs while complete thermalization occurs within 1 ps [46][47]. The breakup of the hydrogen bond network releases solvated proteins and the ablated plume leaves the ablation site as a bullet thus driving the "free" protein out into the gas phase (Figure 2.3.1 (c)). Due to the short pulse duration of PIRL, DIVE ablation occurs faster than any loss mechanism to this transduction such as thermal diffusion or acoustic propagation outside the excited zone, which assures all the deposited energy is transferred into the O-O translation to drive ablation resulting in much less thermal and mechanical damage to the surrounding tissues relative to all other laser sources.

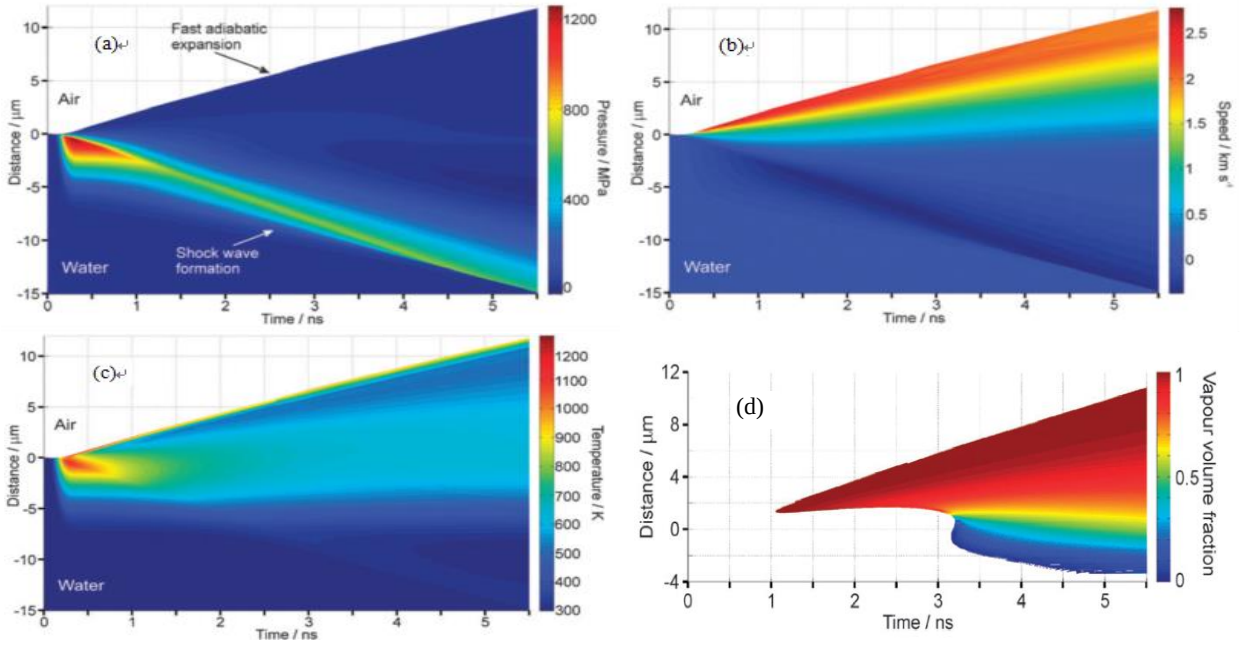

Figure 2.3.2 Numerical Simulation of DIVE ablation in pure water. (a) Pressure evolution; (b) Propagation speed of ablation plume; (c) Temperature evolution; (d) vapour volume fraction evolution. Reprinted with permission from ref. [48]. Copyright © 2010, Royal Society of Chemistry.

Results of numerical simulations of the ablation process in pure water based on fluid dynamics and thermal dynamics are shown in Figure 2.3.2 [48]. The pictures show the model predictions for distributions of pressure, speed and temperature in the excited water volume after absorption of a laser pulse with $t_p = 105\ ps$ duration and $F = 0.7\ J/cm^2$ fluence at a wavelength $\lambda = 2.96\ \mu m$. Due to the strong stress confinement conditions, high initial pressure amplitudes of 1GPa are created in the excited volume within 100 ps, driving the fast volume expansion and generating a strong recoil shock wave into the bulk liquid (Fig. 2.3.2a). Rapid volume expansion at a speed of

2.3 km/s (Fig. 2.3.2b) results in strong adiabatic cooling (Fig. 2.3.2c) of the top 2 μm deep layer within 1 ns after the pulse absorption. Figure 2.3.2d shows the vapor volume fraction in the ablated plume as a function of space and time, which indicates a rapid and thorough vaporization on the top several μm thick layers of water.

Since the absorbed energy goes directly into the ablation process, the DIVE process is believed to lead to almost no thermal tissue damage outside the ablated zone. Experiments on porcine skin and mice with PIRL laser have borne this out. Studies show minimal tissue ablation to the point of single cell precision with less damage of surrounding tissues compared with microsecond Er:YAG lasers. Near absence of scar formation was also observed with the PIRL scalpel [49] [50]. Furthermore, ablation of biological material by PIRL has been shown to result in no loss of biological activity, as evidenced by recent works suggesting that native enzymatic activity and viral infectivity are retained in the plume of PIRL ablated material[51][52]. All these reports indicate PIRL as the softest laser scalpel and that for the first time we can drill down to surgical precision of a single cell without physical and chemical injuries to the peripheral tissues. With these findings, an ion source based on PIRL for image mass spectrometer has more advantages as an on-line surgical guidance to PIRL scalpel over other surgical guidance techniques. Such an ion source could also further examine the ablated tissue at the molecular level whether proteins and other biomarkers are indeed ejected intact, i.e. PIRL provides a faithful fingerprint for the excised tissue. If so, this new concept opens a whole new modality for achieving simultaneously the fundamental (single cell) limits to both minimal invasive surgery and biodiagnostics.

Ultimately the PIRL-DIVE process needs to be quantitatively correlated to molecular composition of tissue and biopsies. The design of quantitative ion sources based on PIRL-DIVE requires the understanding of the ablation process down to molecular level. A molecular dynamics simulation regards on this was performed on a system with lysozyme dissolved in water while single positive charge was put on lysozyme and single negative charge was put on water molecules in the vicinity of lysozyme charged site. The simulation was performed when the ablation is under an electrical field to extract positive lysozyme ions from the negative charged water molecules. The model is to help us find the optimal parameters for maximum desorption and ionization efficiency in DIVE process, which is the key to design intrinsic quantitative ion source for mass spectrometer.

References of Chapter 2

[1] M. M. Zaret, G. M. Breinin, H. Schmidt, H. Ripps, I. M. Siegel, and L. R. Solon, "Ocular lesions produced by an optical maser (laser)," Science, vol. 134, no. 3489, pp. 1525–1526, Nov. 1961.

[2] L. R. Solon, R. Aronson, and G. Gould, "Physiological Implications of Laser Beams," Science, vol. 134, no. 3489, pp. 1506–1508, Nov. 1961.

[3] A. Vogel and V. Venugopalan, "Mechanisms of Pulsed Laser Ablation of Biological Tissues," Chem. Rev., vol. 103, no. 2, pp. 577–644, Feb. 2003.

[4] K. Franjic, "STUDIES OF LASER ABLATION OF LIQUID WATER UNDER CONDITIONS OF IMPULSIVE HEAT DEPOSITION THROUGH VIBRATIONAL EXCITATIONS (IHDVE)," 2010.

[5] M. H. Niemz, Laser-Tissue Interactions: Fundamentals and Applications. Springer Science & Business Media, 2007.

[6] J. D. Jagger, "The Nd-YAG Laser in Ophthalmology: Principles and Clinical Applications of Photodisruption," Br. J. Ophthalmol., vol. 70, no. 1, p. 79, Jan. 1986.

[7] T. Juhasz, F. H. Loesel, R. M. Kurtz, C. Horvath, J. F. Bille, and G. Mourou, "Corneal refractive surgery with femtosecond lasers," IEEE J. Sel. Top. Quantum Electron., vol. 5, no. 4, pp. 902–910, Jul. 1999.

[8] E. S. Lander and others, "Initial sequencing and analysis of the human genome," Nature, vol. 409, no. 6822, pp. 860–921, Feb. 2001.

[9] W. B. Telfair, C. Bekker, H. J. Hoffman, P. R. Yoder, R. E. Nordquist, R. A. Eiferman, and H. H. Zenzie, "Histological comparison of corneal ablation with Er:YAG laser, Nd:YAG optical parametric oscillator, and excimer laser," J. Refract. Surg. Thorofare NJ 1995, vol. 16, no. 1, pp. 40–50, Feb. 2000.

[10] I. E. deVera, J. E. Katz, and D. B. Agus, "Clinical proteomics: the promises and challenges of mass spectrometry-based biomarker discovery," Clin. Adv. Hematol. Oncol. HO, vol. 4, no. 7, pp. 541–549, Jul. 2006.

[11] B. Domon and R. Aebersold, "Review - Mass spectrometry and protein analysis," Science, vol. 312, no. 5771, pp. 212–217, Apr. 2006.

[12] "The top 10 leading causes of death in the US," Medical News Today. [Online]. Available: http://www.medicalnewstoday.com/articles/282929.php. [Accessed: 15-Aug-2015].

[13] D. Li and D. W. Chan, "Proteomic cancer biomarkers from discovery to approval: it's worth the effort," Expert Rev. Proteomics, vol. 11, no. 2, pp. 135–136, Apr. 2014.

[14] M. P. Pavlou, E. P. Diamandis, and I. M. Blasutig, "The Long Journey of Cancer Biomarkers from the Bench to the Clinic," Clin. Chem., vol. 59, no. 1, pp. 147–157, Jan. 2013.

[15] J. B. Fenn, M. Mann, C. K. Meng, S. F. Wong, and C. M. Whitehouse, “Electrospray ionization for mass spectrometry of large biomolecules,” Science, vol. 246, no. 4926, pp. 64–71, Oct. 1989.

[16] M. Karas, D. Bachmann, U. Bahr, F. Hillenkamp, “Matrix-assisted ultraviolet laser desorption of non-volatile compounds,” Int. J. Mass. Spectrom. Ion. Process., vol. 78, pp. 53–68, Sep. 1987.

[17] M. E. Belov, M. V. Gorshkov, H. R. Udseth, G. A. Anderson, and R. D. Smith, “Zeptomole-sensitivity electrospray ionization--Fourier transform ion cyclotron resonance mass spectrometry of proteins,” Anal. Chem., vol. 72, no. 10, pp. 2271–2279, May 2000.

[18] M. Wilm, “Quantitative proteomics in biological research,” Proteomics, vol. 9, no. 20, pp. 4590–4605, Oct. 2009.

[19] P. Nemes and A. Vertes, “Ambient mass spectrometry for in vivo local analysis and in situ molecular tissue imaging,” TrAC Trends Anal. Chem., vol. 34, pp. 22–34, Apr. 2012.

[20] J. M. Wiseman, D. R. Ifa, Q. Song, and R. G. Cooks, “Tissue Imaging at Atmospheric Pressure Using Desorption Electrospray Ionization (DESI) Mass Spectrometry,” Angew. Chem., vol. 118, no. 43, pp. 7346–7350, Nov. 2006.

[21] R. Cooks, B. Gologan, J. Wiseman, N. Talaty, H. Chen, and I. Cotte-Rodriguez, “DESI (desorption electrospray ionization): Ambient mass spectrometry from explosives to proteins to in vivo analysis,” Abstr. Pap. Am. Chem. Soc., vol. 230, p. 256–ANYL, Aug. 2005.

[22] P. Nemes and A. Vertes, “Laser Ablation Electrospray Ionization for Atmospheric Pressure, in Vivo, and Imaging Mass Spectrometry,” Anal. Chem., vol. 79, no. 21, pp. 8098–8106, Nov. 2007.

[23] D. S. Cornett, M. L. Reyzer, P. Chaurand, and R. M. Caprioli, “MALDI imaging mass spectrometry: molecular snapshots of biochemical systems,” Nat. Methods, vol. 4, no. 10, pp. 828–833, Oct. 2007.

[24] J. Hankin, “Sublimation as a method of matrix application for mass spectrometric imaging,” J. Am. Soc. Mass Spectrom., vol. 18, no. 9, pp. 1646–1652, Sep. 2007.

[25] M. Aichler, K. Huber, F. Schilling, F. Lohöfer, K. Kosanke, R. Meier, E. J. Rummeny, A. Walch, and M. Wildgruber, “Spatially resolved quantification of Gadolinium(III)-based magnetic resonance agents in tissue by MALDI imaging mass spectrometry after in vivo MRI,” Angew. Chem. Int. Ed., vol. 54, no. 14, pp. 4279–4283, Mar. 2015.

[26] S. R. Oppenheimer, D. Mi, M. E. Sanders, and R. M. Caprioli, “Molecular Analysis of Tumor Margins by MALDI Mass Spectrometry in Renal Carcinoma,” J. Proteome Res., vol. 9, no. 5, pp. 2182–2190, May 2010.

[27] V. V. Laiko，S. C. Moyer and R. J. Cotter, “Atmospheric Pressure MALDI/Ion Trap Mass Spectrometry,” Anal. Chem., vol.72, no.21, pp. 5239-5243, Sep. 2000.

[28] V. V. Laiko, M. A. Baldwin and A. L. Burlingame, “Atmospheric Pressure Matrix-Assisted Laser Desorption/Ioniation Mass Spectrometry,” Anal. Chem., vol. 72, no. 4, pp. 652-657, Jan. 2000

[29] M. Koestler, D. Kirsch, A. Hester, A. Leisner, S. Guenther and B. Spengler, "A high-resolution scanning microprobe matrix-assisted laser desorption/ionization ion source for imaging analysis on an in trap/Fourier transform ion cyclotron resonance mass spectrometer," Rapid. Commun. Mass Spectrom., vol. 22, no. 20, pp. 3275-3285, Oct. 2008.

[30] S. Guenther, A. Rompp, W. Kummer and B. Spengler, "AP-MALDI imaging of neuropeptides in mouse pituitary gland with 5 μm spatial resolution and high mass accuracy," Int. J. Mass Spectrom., vol. 305, no.2-3, pp. 228-237, Aug. 2011.

[31] D. R. Bhandari, M. Schott, A. Rompp, A. Vilcinskas and B. Spengler, "Metabolite localization by atmospheric pressure high-resolution scanning microprobe matrix-assisted laser desorption/ionization mass spectrometry imaging in whole-body sections and individual organs of the rove beetle Paederus riparius," Anal. Bioanal. Chem., vol.407, no. 8, pp 2189-2201, Mar. 2015 .

[32] N. Lauzon, M. Dufresne, V. Chauhan and P. Chaurund, "Development of Laser Desorption Imaging Mass Spectrometry Methods to Investigate the Molecular Composition of Latent Fingermarks," J. Am.Soc. Mass Spectrom., vol.26, no. 6, pp. 878-886, Jun. 2015.

[33] W. Bouschen, O. Schulz, D. Eikel and B. Spengler, "Matrix vapor deposition/recrystallization and dedicated spray preparation for high-resolution scanning microprobe matrix-assisted laser desorption/ionization imaging mass spectrometry (SMALDI-MS) of tissue and single cells," Rapid. Commun. Mass Spectrom., vol. 24, no. 3, pp. 355-364, Feb. 2010.

[34] J. Wiseman, D. Ifa, Q. Song, and R. Cooks, "Tissue imaging at atmospheric pressure using desorption electrospray ionization (DESI) mass spectrometry," Angew. Chem. Int. Ed Engl., vol. 45, no. 43, pp. 7188–7192, Nov. 2006.

[35] L. S. Eberlin, I. Norton, A. L. Dill, A. J. Golby, K. L. Ligon, S. Santagata, R. G. Cooks, and N. Y. R. Agar, "Classifying human brain tumors by lipid imaging with mass spectrometry," Cancer Res., vol. 72, no. 3, pp. 645–654, Feb. 2012.

[36] D. Calligaris, D. Caragacianu, X. Liu, I. Norton, C. J. Thompson, A. L. Richardson, M. Golshan, M. L. Easterling, S. Santagata, D. A. Dillon, F. A. Jolesz, and N. Y. R. Agar, "Application of desorption electrospray ionization mass spectrometry imaging in breast cancer margin analysis," Proc. Natl. Acad. Sci. U. S. A., vol. 111, no. 42, pp. 15184–15189, Oct. 2014.

[37] S. Santagata, L. S. Eberlin, I. Norton, D. Calligaris, D. R. Feldman, J. L. Ide, X. Liu, J. S. Wiley, M. L. Vestal, S. H. Ramkissoon, D. A. Orringer, K. K. Gill, I. F. Dunn, D. Dias-Santagata, K. L. Ligon, F. A. Jolesz, A. J. Golby, R. G. Cooks, and N. Y. R. Agar, "Intraoperative mass spectrometry mapping of an onco-metabolite to guide brain tumor surgery," Proc. Natl. Acad. Sci. U. S. A., vol. 111, no. 30, pp. 11121–11126, Jul. 2014.

[38] P. Nemes, A. S. Woods, and A. Vertes, "Simultaneous Imaging of Small Metabolites and Lipids in Rat Brain Tissues at Atmospheric Pressure by Laser Ablation Electrospray Ionization Mass Spectrometry," Anal. Chem., vol. 82, no. 3, pp. 982–988, Feb. 2010.

[39] B. Shrestha, R. Javonillo, J. R. Burns, Z. Pirger, and A. Vertes, “Comparative local analysis of metabolites, lipids and proteins in intact fish tissues by LAESI mass spectrometry,” The Analyst, vol. 138, no. 12, p. 3444, 2013.

[40] L. R. Compton, B. Reschke, J. Friend, M. Powell, and A. Vertes, “Remote laser ablation electrospray ionization mass spectrometry for non-proximate analysis of biological tissues: Non-proximate analysis of biological tissues by LAESI-MS,” Rapid Commun. Mass Spectrom., vol. 29, no. 1, pp. 67–73, Jan. 2015.

[41] J. Balog, L. Sasi-Szabó, J. Kinross, M. R. Lewis, L. J. Muirhead, K. Veselkov, R. Mirnezami, B. Dezső, L. Damjanovich, A. Darzi, J. K. Nicholson, and Z. Takáts, “Intraoperative tissue identification using rapid evaporative ionization mass spectrometry,” Sci. Transl. Med., vol. 5, no. 194, p. 194ra93, Jul. 2013.

[42] J. G. Health, S. Reporter, and B. B. C. News, “Cancer surgery: Tumour ‘sniffing’ surgical knife designed,” BBC News. [Online]. Available: http://www.bbc.com/news/health-23348661. [Accessed: 19-Aug-2015].

[43] Sam Wong, “Waters Corporation acquires iKnife technology,” Jul. 2014.

[44] J. Kuriyan, B. Konforti, and D. Wemmer, The Molecules of Life: Physical and Chemical Principles. Garland Science, 2012.

[45] H. Ishikawa, K. Kwak, J. K. Chung, S. Kim, and M. D. Fayer, “Direct observation of fast protein conformational switching,” Proc. Natl. Acad. Sci., vol. 105, no. 25, pp. 8619–8624, Jun. 2008.

[46] M. L. Cowan, B. D. Bruner, N. Huse, J. R. Dwyer, B. Chugh, E. T. J. Nibbering, T. Elsaesser, and R. J. D. Miller, “Ultrafast memory loss and energy redistribution in the hydrogen bond network of liquid H2O,” Nature, vol. 434, no. 7030, pp. 199–202, Mar. 2005.

[47] D. Kraemer, M. L. Cowan, A. Paarmann, N. Huse, E. T. J. Nibbering, T. Elsaesser, and R. J. D. Miller, “Temperature dependence of the two-dimensional infrared spectrum of liquid H2O,” Proc. Natl. Acad. Sci. U. S. A., vol. 105, no. 2, pp. 437–442, Jan. 2008.

[48] K. Franjic and R. J. D. Miller, “Vibrationally excited ultrafast thermodynamic phase transitions at the water/air interface,” Phys. Chem. Chem. Phys., vol. 12, no. 20, pp. 5225–5239, 2010.

[49] N. Jowett, W. Wöllmer, A. M. Mlynarek, P. Wiseman, B. Segal, K. Franjic, P. Krötz, A. Böttcher, R. Knecht, and R. J. D. Miller, “Heat Generation During Ablation of Porcine Skin With Erbium:YAG Laser vs a Novel Picosecond Infrared Laser,” JAMA Otolaryngol. Neck Surg., vol. 139, no. 8, p. 828, Aug. 2013.

[50] S. Amini-Nik, D. Kraemer, M. L. Cowan, K. Gunaratne, P. Nadesan, B. A. Alman, and R. J. D. Miller, “Ultrafast Mid-IR Laser Scalpel: Protein Signals of the Fundamental Limits to Minimally Invasive Surgery,” PLoS ONE, vol. 5, no. 9, p. e13053, Sep. 2010.

[51] M. Kwiatkowski, M. Wurlitzer, M. Omidi, L. Ren, S. Kruber, R. Nimer, W. D. Robertson, A. Horst, R. J. D. Miller, and H. Schlüter, “Ultrafast extraction of proteins from tissues using desorption by impulsive vibrational excitation,” Angew. Chem. Int. Ed Engl., vol. 54, no. 1, pp. 285–288, Jan. 2015.

[52] L. Ren, W. D. Robertson, R. Reimer, C. Heinze, C. Schneider, D. Eggert, P. Truschow, N.-O. Hansen, P. Kroetz, J. Zou, and R. J. D. Miller, “Towards instantaneous cellular level bio diagnosis: laser extraction and imaging of biological entities with conserved integrity and activity,” Nanotechnology, vol. 26, no. 28, p. 284001, Jul. 2015

Chapter 3
Construction of a Picosecond Laser Ablation Electrospray Ionization (PIR-LAESI) Imaging Mass Spectrometer Interface for Molecular Mapping of Biological Tissue

3.1 Picosecond Infred Lasers (PIRL)

Ablation under DIVE condition requires laser systems with a wavelength of $\lambda = 2.94\ \mu m$ to match the 3400 cm^{-1} absorption band of water. According to previous studies, in order to drive the DIVE process more efficiently, laser pulses with a pulse duration less than 1 ns and fluence of > 1.0 mJ/cm^2 are needed, corresponding to pulse energy of > 80 μJ for a beam diameter of 100 μm [1]. Since the pulsed laser-tissue interaction is a dynamic process, the dynamic optical properties of water within tissue will also affect the ablation efficiency with IR irradiation. Figure 3.1.1 shows the changes of the absorption coefficient of liquid water versus deposited energy density at $\lambda = 2.94\ \mu m$ and $\lambda = 2.79\ \mu m$ respectively [2]. In Figure 3.1.1, it can be noticed that the absorption coefficient of liquid water at $\lambda = 2.94\ \mu m$ starts to decrease from energy density of 0.03 kJ/cm^3 whereas at $\lambda = 2.79\ \mu m$ the absorption coefficient starts to increase at energy density of 1.0 kJ/cm^3. This is due to the weakening of the hydrogen bond network at higher energy density, resulting in a blue-shift of the absorption spectrum of liquid water. Given an irradiation pulse at $\lambda = 2.94\ \mu m$, the energy deposited by the leading edge of the pulse will reduce the absorption of water in the peak of the pulse. However, when using an irradiation pulse at $\lambda = 2.79\ \mu m$, the absorption in the leading part of the pulse will not be efficient. In order to enhance the absorption of the entire incident pulse, the wavelength of the irradiation should be in between of 2.94 μm and 2.79 μm. For this reason, our PIRL system was designed with the output IR pulse centered at $\lambda = 2.88\ \mu m$.

In the present application of developing an imaging mass spectrometer based on laser ablation, the scanning duration of the sample with the laser should be as short as possible, which requires the material removal rate and thus the repetition rate of laser system to be as high as possible. The stability of laser pulses is another critical requirement for practical application. A molecular map is constructed based on the ion abundance and spatial distribution of molecules of interest.

For accurate construction of the molecular map, the variation of ion abundance from pixel to pixel (laser shot to laser shot) should only reflect the concentration distribution of the molecules in the tissue. However, there are many other parameters that can also affect the detected ion abundance, such as the variation of laser pulse energy which leads to a variation in the efficiency of DIVE process. As well, variation and instability in the ionization and ion collection efficiency and sample integrity (no degradation during experiment) contribute to molecular mapping artifacts. The design of the PIRL system is therefore required to be robust and simple for solid performance.

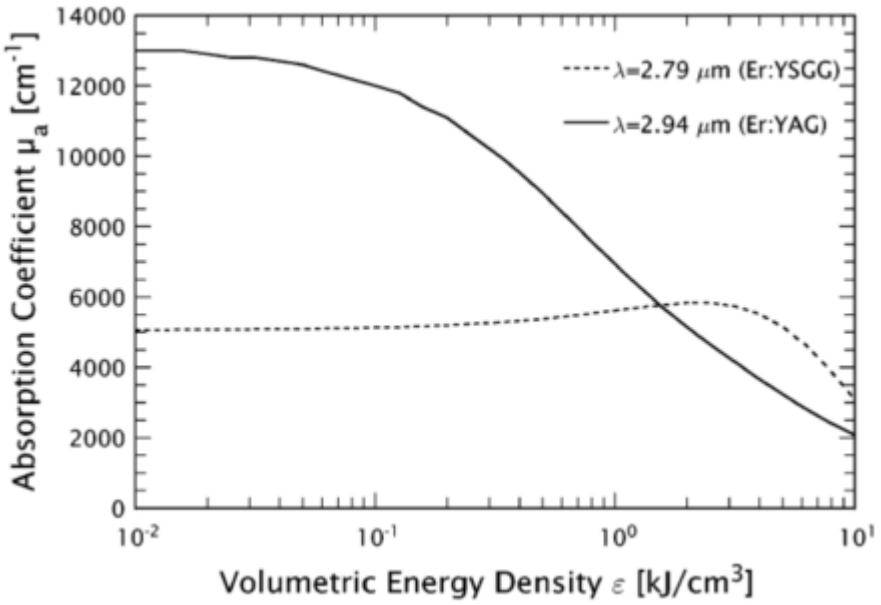

Figure 3.1.1 Dynamics of absorption coefficient of liquid water under different volumetric energy density at wavelength $\lambda = 2.94\ \mu m$ and $\lambda = 2.79\ \mu m$. Reprinted with permission from ref. [2]. Copyright (1993) American Institute of Physics.

Generally, construction of laser devices utilizing infrared wavelengths is more complicated than construction of their counterparts in the near infrared and visible part of the spectrum. The laser gain materials that can be directly pumped with practical sources are scarce (with two important exceptions of Er:YAG and CO_2), the gain cross sections are typically smaller and the scattering and absorption losses in the resonators higher [1]. These effects result in the large thermal load associated with these laser systems. So far, the lasers of choice for the infrared ablation of water and water rich materials have been based on Er:YAG crystals. To reduce the thermal effect, practical implementations require pulsed pumping with large pump pulse energies and low

repetition rates. Another difficulty is that Er:YAG is not easy Q-switched electro-optically due to the strong absorption of most electro-optical crystals in the 3 μm wavelength range. Mechanical Q-switching has been reported with outputs of 30 mJ pulse energy, 290 ns pulse duration and repetition rate of 25 Hz [3]. Generating higher peak power pulses with these lasers will lead to the multimode operation of the cavity and thus an output beam that is highly divergent and of low fluence. Typically, the output of Er:YAG lasers consists of 1 ~ 100 mJ of pulse energy with repetition rates less than 100 Hz and a pulse duration from a few tens to hundreds ns [4].

Alternatively, the desired infrared wavelengths can also be produced using nonlinear frequency conversion by using optical parametric amplifiers (OPA) and optical parametric oscillators (OPO) [1]. High nonlinear conversion efficiency in the OPA or OPO is in need to generate infrared pulses with the required high pulse energy. This demands a nonlinear crystal with a high nonlinear coefficient for the particular phase-matching conditions. Significant progress has been made in the development of nonlinear crystals in recent years, Potassium Titanyl Arsenate (KTiOAsO4 or KTA) [5] appears to be one of the most favorable crystals for the design of mid-IR nonlinear laser systems due to its large nonlinear coefficient (up to 3.6 pm/V in the phase matching direction) and infrared transparency (up to $\lambda = 4\ \mu m$). It also has a high damage threshold which allows pumping with large peak powers up to 10 GW/cm^2 thus offsetting the disadvantage of low gain for mixing long wavelengths in the IR region.

The KTA based OPO system pumped by a Q-switched Nd:YAG laser has been commercialized, e.g the IR Opolette 2940 system from Opotek Inc, CA, US. This laser system is utilized in the nanosecond version of Laser Ablation Electrospray Ionization (LAESI) imaging mass spectrometers. The output pulse of this type of laser system usually has pulse energy of a few mJ, pulse duration of sub-10ns and repetition rate of ~20 Hz. Compared with Er:YAG, the pulse duration of OPO is much shorter though still longer than the DIVE required version of a few picosecond to sub-ns and the repetition rate on the same order of Er:YAG, only a few tens Hz. The beam quality of the OPO system is usually not good and is described by the M2 factor, which measures the divergence of a laser beam and thus determines the minimal focused spot size available to the laser output. The spot size of Gaussian beam on focus is proportional to its beam quality factor M^2 as [6]

$$\omega_{actual} = \frac{M^2 \lambda f}{\pi \omega_0} \tag{3.1}$$

where ω_{actual} is the radius of the beam at the focus of the lens, λ is the wavelength of the beam, f is the focal length of the lens and ω_0 is the input beam radius at the lens. Both experimental and numerical investigation has been performed to understand the effects of cavity parameters on the M^2 of ns-pumped OPO output [7] [8]. The result shows that the minimum M^2 that can be achieved for ns-pumped OPO is around 2 with the condition that the pump energy is just above the threshold energy of OPO process, which means both the stability and the pulse energy of the OPO output is reduced. For the commercial OPO from Opotek Inc, the M^2 is around 8 with the output beam diameter at about 3 mm. Given a focusing lens of focal length, $f = 100\ mm$, and that the lens is placed immediately at the output of the OPO, the beam can be focused to a spot of 250 μm in diameter. For applications such as microsurgery and imaging mass spectrometry, the spatial resolution of the technique is primarily limited by the ablation spot size on the sample. The large M^2 of the Nd:YAG pumped OPO output limits the spatial resolution to a few hundred micrometers.

To satisfy the requirement of the DIVE ablation condition, Picosecond Infrared Lasers (PIRL) was designed via KTA-based optical parametric amplifiers (OPA) pumped with high power diode pumped solid stated lasers (DPSS) with a wavelength of $\lambda = 1.053\ \mu m$. Such DPSS lasers are an industrial standard with proven technology and mature designs [9]. Pulses with sub-nanosecond durations and mJ pulse energies corresponding to peak power of several GW/cm^2 can be routinely generated by amplifying the mode-locked pulses using regenerative amplifiers [9]. By using a CW seeded OPA, the solid performance of DPSS insures the stability of the mid-IR pulse outputs from the OPA which is a critical requirement for practical application as discussed above. The repetition rate of the system is also adjustable by controlling the repetition rate of the regenerative amplifier and can be as high as a few kHz.

The PIRL laser system used a passively mode-locked Nd:YLF Oscillator, a Nd:YLF regenerative amplifier and an Optical Parametric Amplifier (OPA). Due to the non-linear parametric amplification process, the instability in the pump beam will result in more violent fluctuation in the OPA's output pulse energy, thus a characterization of the three components of the PIRL laser

was performed and the stability of both pump and the output of OPA was monitored. This chapter will introduce their working scheme and the characterization of each output respectively with a layout of the entire PIRL system as well as the control electronics.

3.1.1 Passively Mode-Locked Nd:YLF Oscillator

The pump of the OPA was generated by amplifying the pulse from a passively mode-locked Nd:YLF (Neodymium-doped yttrium lithium fluoride) oscillator with an output wavelength $\lambda=1.053\ \mu m$ and pulse duration 108.25 ps. The technology for building such an oscillator has been very well established and the mechanism has been discussed in detail both theoretically and experimentally [10]–[12]. With the development of Semiconductor Saturable Absorber Mirror (SESAM) [12], the construction of the cavity used for passive mode-locking is achieved by replacing one of the end mirrors with a SESAM. The saturable absorption of SESAM introduces Q-switching to the cavity so that Q-switching and mode-locking can occur simultaneously. This working regime of the cavity is called Q-switched mode-locking (QML) which results in the output mode-locked pulse under a Q-switching envelope as shown in Figure 3.1.2. However, the critical requirement for the stability of pulse energy in practical applications requires the cavity to operate under the continuous-wave mode-locking (CWML) regime (Figure 3.1.2). The cavity dynamics of those two mechanism has been fully described with the criteria [12]

$$E_{p,c}^2 > E_{SAT,L} E_{SAT,A} \Delta R \tag{3.2}$$

where $E_{p,c}$ is the intra-cavity pulse energy, $E_{SAT,L}$ is the gain saturation energy of the laser medium, $E_{SAT,A}$ is the saturation energy of SESAM and ΔR is its modulation depth. When the intra-cavity pulse energy is above this threshold, the cavity is working in the CWML regime with the repetition rate of the output pulse only determined by the cavity length $F_r = c/2L$.

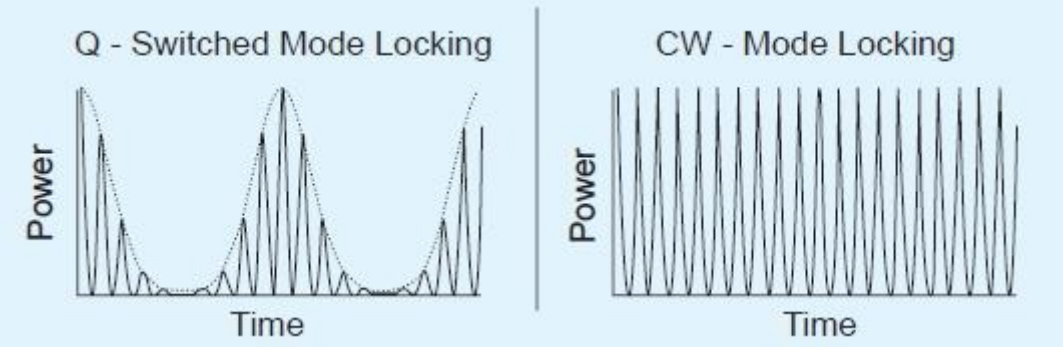

Figure 3.1.2 Different operation modes of a laser with SESAM. Q-Switched Mode Locking and CW mode-locking. Reprinted with the permission of Ref. [12]. Copyright © 1996, IEEE.

The disadvantage of SESAM is that the damage threshold is typically not very high. If the intra-cavity pulse energy is too close to the critical value determined by equation 3.2, the Q-switch instability will drive the cavity to fluctuate between QML and CWML regimes. However, if the intra-cavity pulse energy is too high, it is possible to damage the SESAM. Many techniques have been developed to expand the CWML regime by increasing the stability of CWML and protecting the SESAM. One technique is to insert a two-photon absorber (e.g Indium phosphide—InP) into the cavity to suppress the Q-switch. The role of the two-photon absorber has been theoretically studied [13] and experiments prove such an absorber can reduce the CWML threshold by a factor of 2 [14].

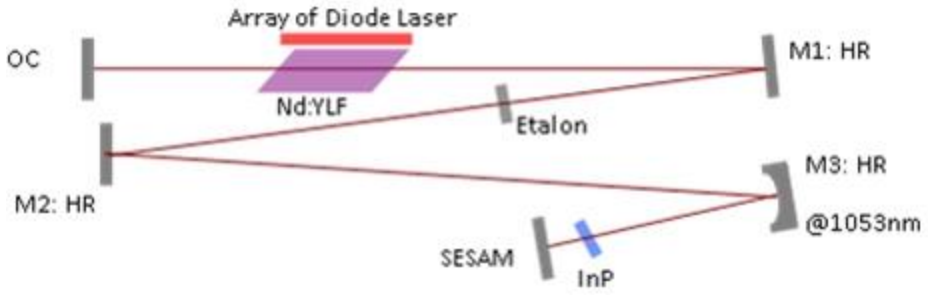

Figure 3.1.3 Layout of passively mode-locked oscillator. OC, output coupler, HR, high-reflective coated at $\lambda = 1.053\ \mu m$.

In our system, the Passively mode-locked Nd:YLF oscillator was built based on the design discussed above. The layout of the cavity is shown in Figure 3.1.3. An output coupler (OC) with transmission of 2% at $\lambda = 1.053\ \mu m$ was used as one end mirror and the other end mirror was a SESAM (Batop, Germany) with a reflection modulation depth of 2%. The laser medium Nd:YLF was 110 mm long and was cut at the Brewster angle to ensure the emission of 1.053 μm. The crystal was side-pumped by an array of diode lasers at its absorption range of 790 nm ~ 810 nm.

Both the crystal and diode laser array were mounted on a water-cooling copper block. The distance between the OC and the crystal was 210 mm. The beam was focused onto the SESAM by an $R_m = 150\ mm$ curved mirror with high reflective coated (HR) at 1.053 μm. To suppress Q-switching, an InP plate was inserted into the cavity at a position ~ 15 mm away from the SESAM so that the pulses hitting the InP had enough intensity to stimulate the two-photon absorption process while maintaining that the energy left by the InP was capable of saturating the SESAM. To further protect the SESAM, an Etalon was also inserted into the cavity to broaden the pulse duration thus reducing the peak intensity. Other parameters of the cavity geometry were: distance from output coupler to the first cavity folding mirror (M1) was 700 mm, from M1 to M2 was 590 mm, from M2 to the curved mirror M3 was 510 mm, and from M3 to SESAM was 80 mm. The total cavity length was 1880 mm.

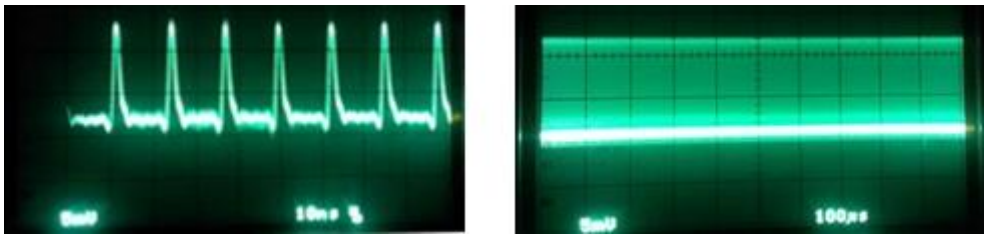

Figure 3.1.4 Screenshot on the oscilloscope of output pulse train from the passively mode-locked Nd:YLF oscillator. Left – 10 ns/div; right – 100 μs/div.

Using this design, the threshold of CWML was 57.40 mW of output power corresponding to intracavity power of 2.87 W. The repetition rate of the output pulses is determined only by the length of the cavity which in this case was 79.73 MHz, corresponding to a pulse-to-pulse interval 12.54 ns. For stable CWML, the oscillator was usually operated with an electrical pump power of ~ 40 W, an output power of 76.50 mW and pulse energy 0.96 nJ/pulse. Screen shots of the output pulse train is presented in Figure 3.1.4 with a short time scale (10 ns/div, left) and a long time scale (100 μs/div, right). The top line on the screen shot of the long time scale one shows how stable the CWML output was.

The pulse duration of the output was measured by autocorrelation and the results are shown in Figure 3.1.5. The data were analyzed with OriginLab 9 with the fitting performed by using the GaussianAmp function (insert in Figure 3.1.5) within the software. The values of the fitting parameters are shown in Figure 3.1.5. The actual pulse duration was the product of the measured autocorrelation FWHM and a deconvolution factor, which is $\sqrt{2}/2$ for Gaussian pulses [15].

According to the autocorrelation measurement, the FWHM was 153.10 ps resulting in a pulse duration of 108.25ps.

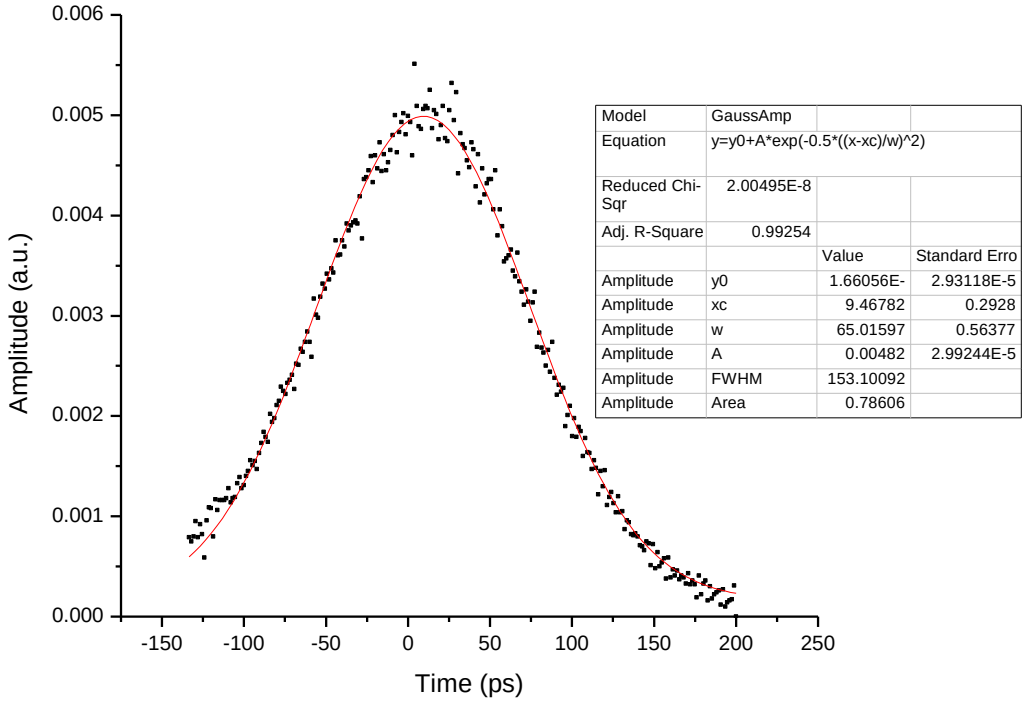

Figure 3.1.5 Autocorrelation of the pulse duration for the output of passively mode-locked Nd:YLF oscillator.

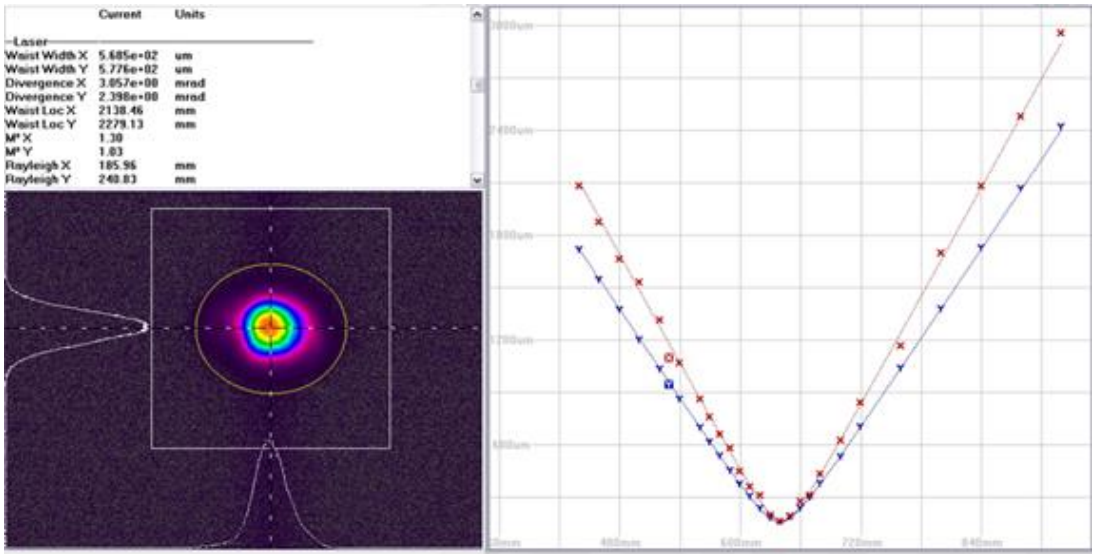

Figure 3.1.6 Beam profile and M^2 measurement for the output of passively mode-locked Nd:YLF oscillator.

The output beam of the passively mode-locked Nd:YLF oscillator was calibrated by a M^2 measurement meter (Ophir-Spiricon, LLC, USA). The results are shown in Figure 3.1.6 with the beam profile and the parabolic fit of beam diameter at different position from the output coupler of the cavity. The beam was a symmetric, round TEM_{00} mode with beam waist of 568.5 μm in *x* direction and 577.6 μm in *y* direction (Figure 3.1.6). From the parabolic fitting, the M^2 in the *x* direction was 1.30 and in the *y* direction was 1.03. This beam then served as the seed for a regenerative amplifier which will be discussed in the next session.

3.1.2 Nd:YLF Regenerative Amplifier

Regenerative amplifiers produce energetic picosecond pulses at repetition rate up to several kHz from a train of low-energy pulses [9] and thus were used to amplify the pulses generated by the passively mode-locked Nd:YLF oscillator in the PIRL system. The pulse energy can be amplified by as much as 10^6~10^7 times by picking individual pulse from the oscillator's pulse train and allowing it pass through the gain medium of the amplifier many times. The design of regenerative amplifiers is distinct from other amplifier by their use of Pockels Cell. The layout of regenerative amplifier used in the PIRL system is shown in Figure 3.1.7.

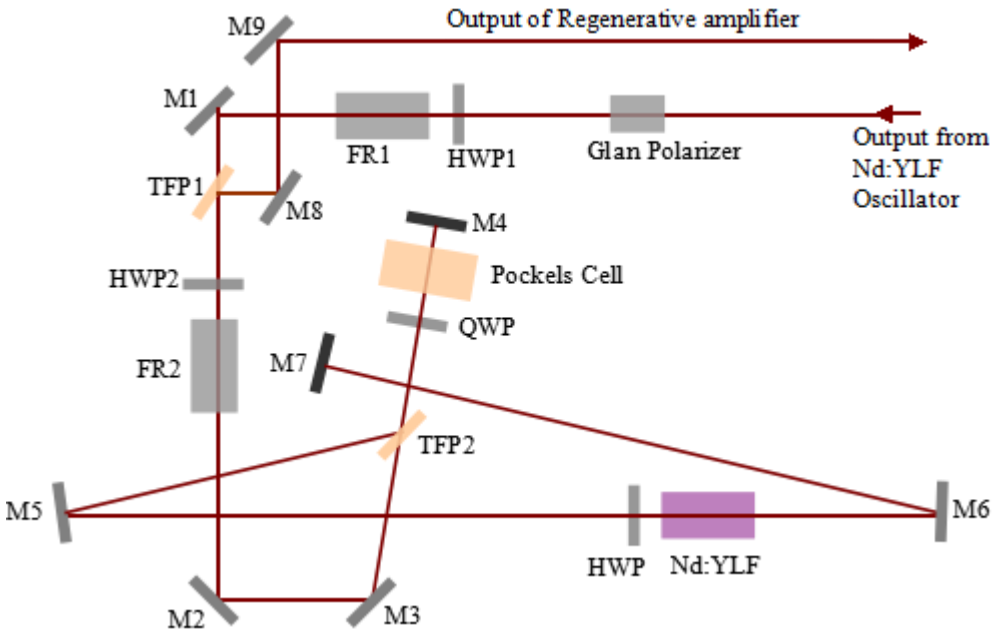

Figure 3.1.7 Layout of regenerative amplifier. M1~M9, flat mirror with high reflective coating at 1.053 μm; HWP, half-wave plate; FR, Faraday Rotator; TFP, thin film polarizer; QWP, quarter-wave plate.

In Figure 3.1.7, all the mirrors labeled with M1~M9 were flat mirrors with high reflective coating at $\lambda = 1.053\ \mu m$. The horizontally polarized output pulses from the Nd:YLF oscillator were rotated to vertically polarized pulses by a combination of a half-wave plate and a Faraday Rotator (not shown in the layout) and were directed into the Glan Polarizer for further purifying the polarization state. The pulses were then turned into horizontally polarized light by another combination of a half-wave plate (HWP1) and Faraday Rotator (FR1) and thus can pass through the thin film polarizer (TFP1) following mirror M1. These pulses then experienced a 135^0 degrees of rotation in polarization by the second half wave plate (HWP2) and an additional 45^0 degrees of rotation by Faraday rotator (FR2), resulting in no net change in the polarization. These horizontally polarized pulses were then injected into the resonator by M2 and M3 through the second thin film polarizer (TFP2). The power supply of the Pockels Cell was synchronized with the output of the Nd:YLF oscillator. When the high voltage of Pockels Cell was off, individual pulse from the horizontally polarized pulse train passed through the quarter-wave plate (QWP) twice via the rear cavity mirror M4, experiencing a 90^0 rotation to vertical polarization and thus can be reflected by TFP2 into the gain medium (Northrop Grumman, USA) via mirror M5. Once the beam left the Pockels Cell travelling towards M5, the high voltage of the Pockels cell was turned on. The voltage rise time is typically a few nanoseconds from zero to the level required for a $\lambda/4$ retardation. There are two reasons to switch on the voltage at this point: First, in order to make sure that the required $\lambda/4$ voltage was already achieved in the Pockels Cell when the pulse inside the cavity passes back to the TFP2 from the gain medium. This insured the pulse would not experience a polarization change by passing through the QWP and Pockel's cell twice via M4 and thus would stay inside the cavity for amplification; Second, since pulses experienced no polarization change with the high voltage applied on the Pockels Cell, pulses that came after the trapped pulse from the output of Nd:YLF oscillater (pulse-to-pulse interval 12.54 ns) would directly leak out from TFP2 without any amplification. The trapped pulse underwent a few round-trip inside the cavity until its pulse energy was saturated, which can be directly monitored on an oscilloscope indicated by the pulse train displaying a Q-switched envelope (Figure 3.1.8). Once the pulse energy was saturated, the high-voltage of the Pockels Cell was switched off to let the amplified pulse output from the cavity via the TFP2 by experiencing 90^0 degrees of rotation from the quarter-wave plate (QWP) and was then horizontally polarized. This pulse experienced a -45^0 rotation from FR2 and another 135^0 rotation from HWP2, 90^0 degrees of rotation in total, and became vertically polarized. It was

reflected by TFP1 to M8 and M9 to the output. The half-wave plate (HWP) in front of the gain medium was used to suppress the YLF stronger emission at 1.047 μm but with a polarization perpendicular to the 1.053 μm emission. The geometry parameters of the cavity were as follows: distance between M4 to TFP2 was 270 mm, from TFP2 to M5 was 250 mm, from M5 to HWP was 410 mm, from HWP to M6 was 260 mm, from M6 to M7 was 480 mm, resulting in a total cavity length of 1650 mm.

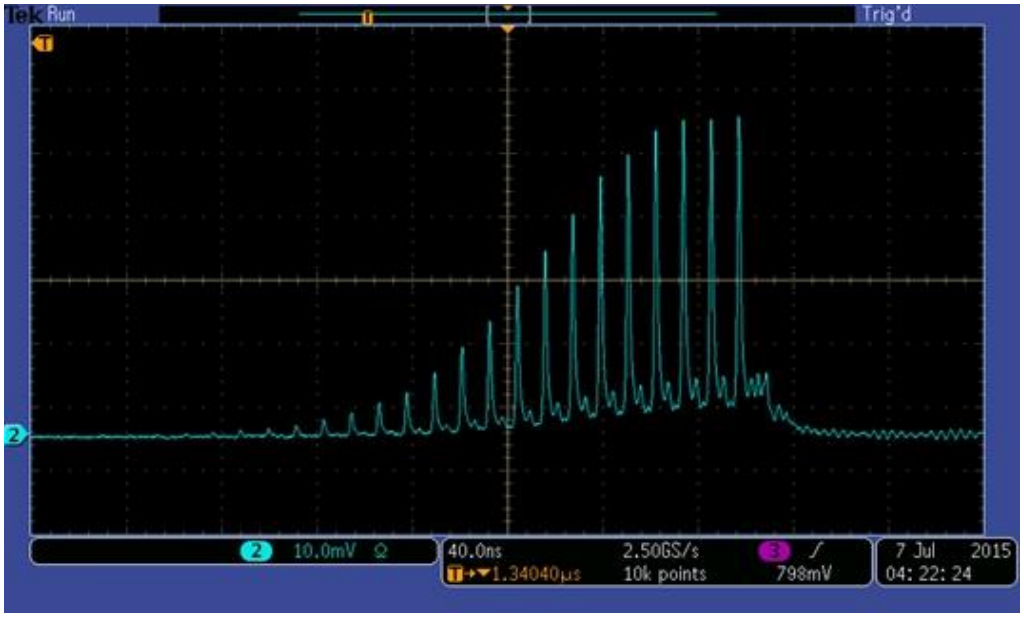

Figure 3.1.8 Pulse train of the amplified trapped pulse of Nd:YLF regenerative amplifier.

Figure 3.1.8 shows the pulse trains of the trapped pulse by detecting the leakage from one of the cavity mirrors, e.g M5 in our case. The pulse train indicates that the trapped pulse experienced 24 round-trips inside the cavity for the saturated amplification. The output pulse energy was 1.90 mJ with a repetition rate of 100 Hz, indicating an amplification factor of 1.98×10^6. The stability of the output of the amplified pulse was also monitored via the amplitude of the pulse from the oscilloscope with LabView program. The results are shown in Figure 3.1.9, and demonstrate a fluctuation of 1.57% during a monitoring time of 50 minutes. The beam quality of the output pulse was characterized by the M^2 meter (Ophir-Spiricon, LLC, USA) with the result shown in Figure 3.1.10. The beam profile shows the output of the regenerative amplifier was a symmetric round TEM_{00} mode from the cavity, with the waist width of 1518 μm in *x* direction and 1756 μm in *y* direction and the beam quality factor M^2 of 1.11 in *x* direction and 1.29 in *y* direction

respectively. This beam was then directed toward the Optical Parametric Amplifier to serve as the pump for the high energy mid-IR pulse generation.

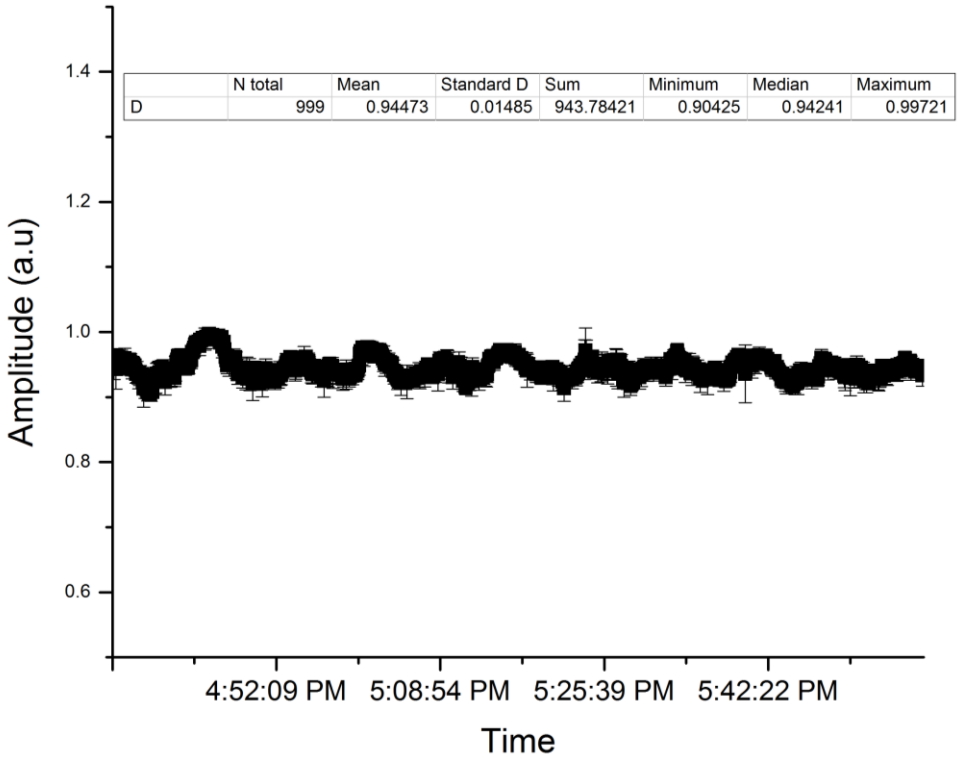

Figure 3.1.9 Stability of output pulse energy of Nd:YLF regenerative amplifier.

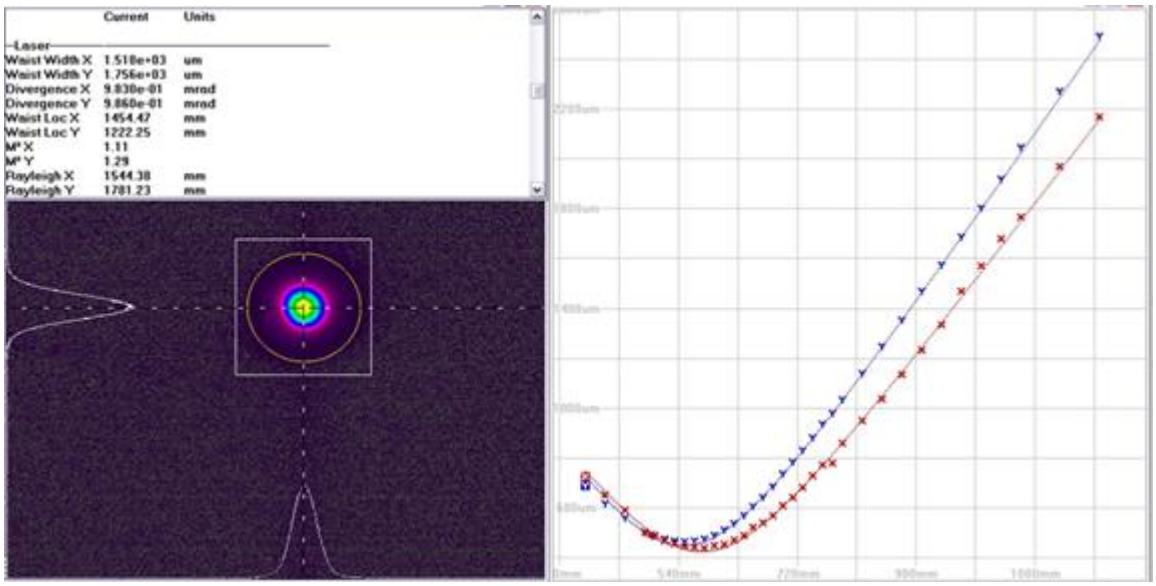

Figure 3.1.10 Beam profile and M^2 measurement for the output of regenerative amplifier.

3.1.3 Optical Parametric Amplifier (OPA)

An Optical Parametric Amplifier is a nonlinear device based on a three-wave mixing process, in which a pump beam, a signal beam and an idler beam at frequencies ω_p, ω_s and ω_i respectively, with $\omega_p = \omega_s + \omega_i$, propagate and interact in a nonlinear medium [16]. In principle, if the pump pulses are intense enough, no signal beam is required and the amplified pulse can be generated though optical parametric generation (OPG) where the signal and the idler beams are generated from quantum fluctuations [17]. However, in practice, the initial presence of a narrowband signal beam will significantly reduce the threshold of generating idler photons and improve beam quality [18] as well as aid in the OPA alignment. Using the output of the Nd:YLF regenerative amplifier as the pump beam ($\lambda = 1.053\ \mu m$), and the required idler generation and amplification near $\lambda = 2.94\ \mu m$ for ablation under DIVE condition, the signal wavelength must be in the 1.60 ~ 1.66 μm range. In this spectral region, distributed feedback (DFB) laser diodes developed for telecom applications are available. With their narrow bandwidth, high stability, single mode operation, and long lifetime, they are a perfect choice for this configuration.

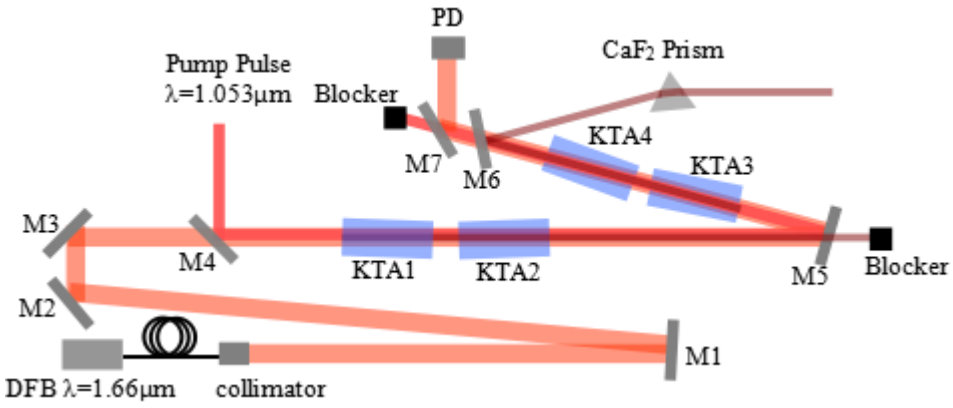

Figure 3.1.11 Scheme of Optical Parametric Amplifier (OPA). DFB, distribute feedback diode laser; M1~M3, Gold coated mirror; M4, anti-reflective coated at λ=1660nm but high reflective coated at $\lambda=1.053\ \mu m$; M5, anti-reflective coated at $\lambda = 2.88\ \mu m$ but high reflective coated at $\lambda = 1.66\ \mu m$ and $\lambda=1.053\ \mu m$; M6, anti-reflective coated at $\lambda = 1.66\ \mu m$ and $\lambda = 1.053\ \mu m$ but high reflective coated at $\lambda=2.88\ \mu m$; M7, anti-reflective coated at $\lambda = 1.053\ \mu m$ but high reflective coated at $\lambda = 1.66\ \mu m$; PD, photodiode detection the amplified signal pulse; CaF_2 prism, apex angle 60°.

The scheme of the OPA is shown in Figure 3.1.11. The output of the Nd:YLF regenerative amplifier was collimated to a diameter of 1.00 mm at the crystals' position via a telescope before the OPA serving as the pump beam (red in Figure 3.1.11). A CW single mode DFB laser diode at 1.66 μm (NTT Electronics Corp) was used as the signal seed, resulting in the generated idler

wavelength $\lambda = 2.88\ \mu m$ for optimum efficiency of the DIVE ablation process. The diode's optical output was coupled into a polarization preserving fiber and was collimated to a beam of diameter 1.50 mm via a collimator (orange in Figure 3.1.11). The signal beam size was slightly larger than the pump beam for maximum energy conversion. Approximately 3 mW of power from the DFB was incident at the OPA due to losses. The pump and the signal beam were combined and overlapped via a dielectric mirror M4 which was high reflection coated for the pump but anti-reflection coated for the seed.

The OPA consisted of four KTA crystals cut at ($\theta = 63.9^o$, $\varphi = 0.0^o$) for type II collinear phase matching. Two of these crystals, 12 mm lengths, were used as a pre-amplifier and arranged in a walk-off compensating geometry. The generation of the idler beam (dark red in Figure 3.1.11) started from the first crystal (KTA1). However, the temporal mismatch between the pump pulse, the signal pulse and the generated idler pulse due to the group velocity dispersion of air will result in destructive interference of the idler generated in the pre-amplifier and the main amplifier (KTA3 and KTA4) and thus reduce the conversion efficiency. To avoid this effect, the idler beam generated in the pre-amplifier was filtered out by a dielectric mirror (M5) while only the pump and the amplified signal beams were reflected into the main amplifier. The idler output of the main amplifier was reflected by a dielectric mirror M6 with a high reflection coating at the idler's wavelength $\lambda = 2.88\ \mu m$ but anti-reflected coated at the pump and signal wavelength. The idler spectrum was further purified by the dispersion from a CaF2 prism (apex angle 60^o). The filtered signal beam was reflected by a dielectric mirror M7 with high reflective coating at $\lambda = 1.66\ \mu m$ and was detected by a photodiode (Thorlabs DET410) to monitor the behavior of the OPA.

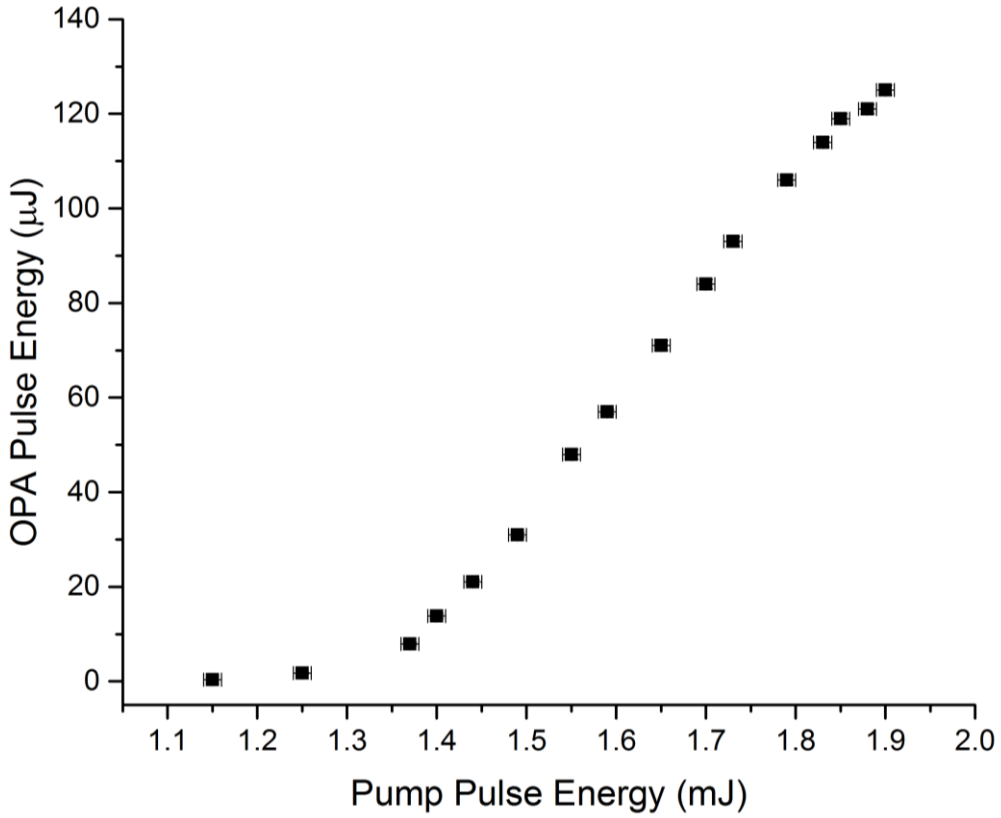

Figure 3.1.12 Output pulse energy vs pump pulse energy of OPA.

The generated idler output of this OPA had a pulse energy of 120 μJ at $\lambda = 2.88\ \mu m$. The basic amplifier performance was characterized by the idler's output power as a function of input peak pump power. The results are shown in Figure 3.1.12 where the OPA started to saturate at input pump power of 195 mW, corresponding to pulse energy of 1.95 mJ/pulse. The stability of the OPA under saturation condition was also monitored by the photodiode over a period of 50 minutes with the results illustrated in Figure 3.1.13., which show a fluctuation of 1.9% in the output pulse energy.

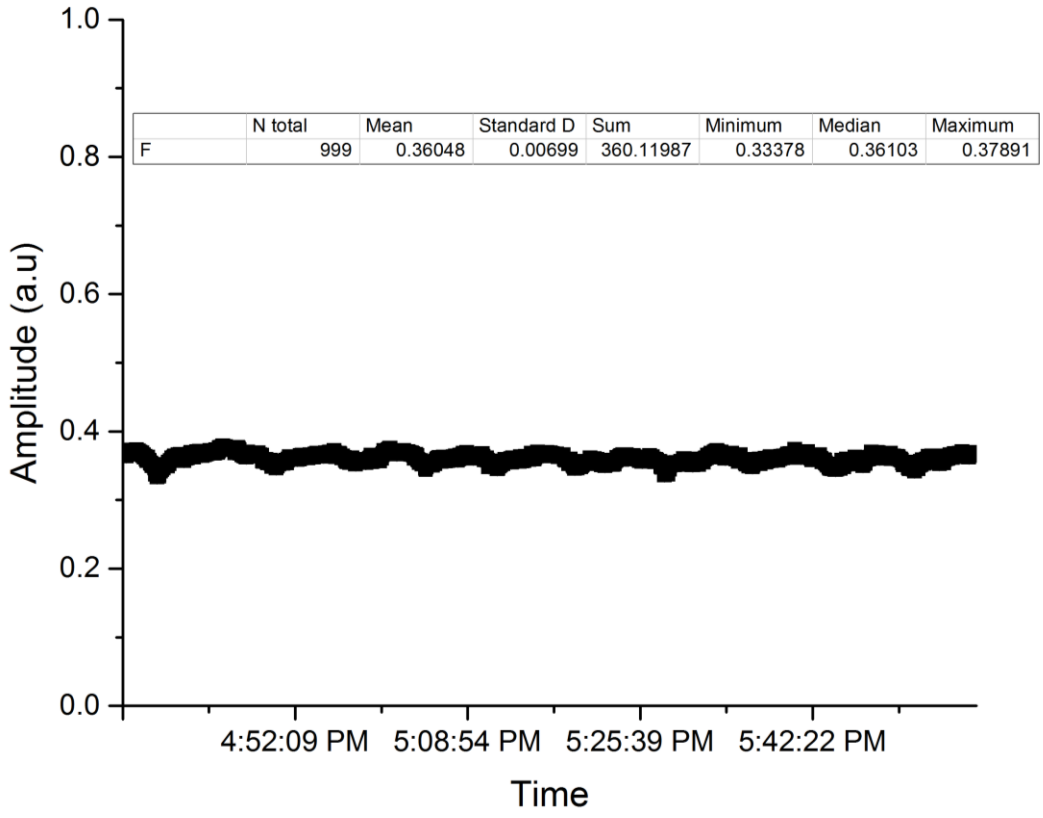

Figure 3.1.13 Stability of OPA output pulse energy.

The fluence of the incident laser beam is a critical parameter in ablation which defines the ablation threshold etc. If there is hot spot in the beam, though the average fluence is low, the local fluence can be very high which will lead to an observed ablation threshold value that is lower than what is needed for uniform ablation. The beam profile of the output of OPA was measured with a 200 μm pinhole scanned across the beam with a step size of 50 μm at the position where the beam was expanded to diameter of 4 ~ 5 mm. The results are shown in Figure 3.1.14, with Figure 3.1.14A showing the 3D peak plot of the power distribution and Figure 3.1.14B showing the corresponding counter plot in grey scale. The purple and blue lines in Figure 3.1.14B indicate the position where the data was extracted for Gaussian fitting along the *x* and *y* axis respectively. The extracted data together with the fitting is shown in Figure 3.1.14C for the *x* axis and Figure 3.1.14D for the *y* axis. The power distribution for the OPA output was Gaussian along both directions, though the beam was slightly elliptical. There were no hot spots in the beam.

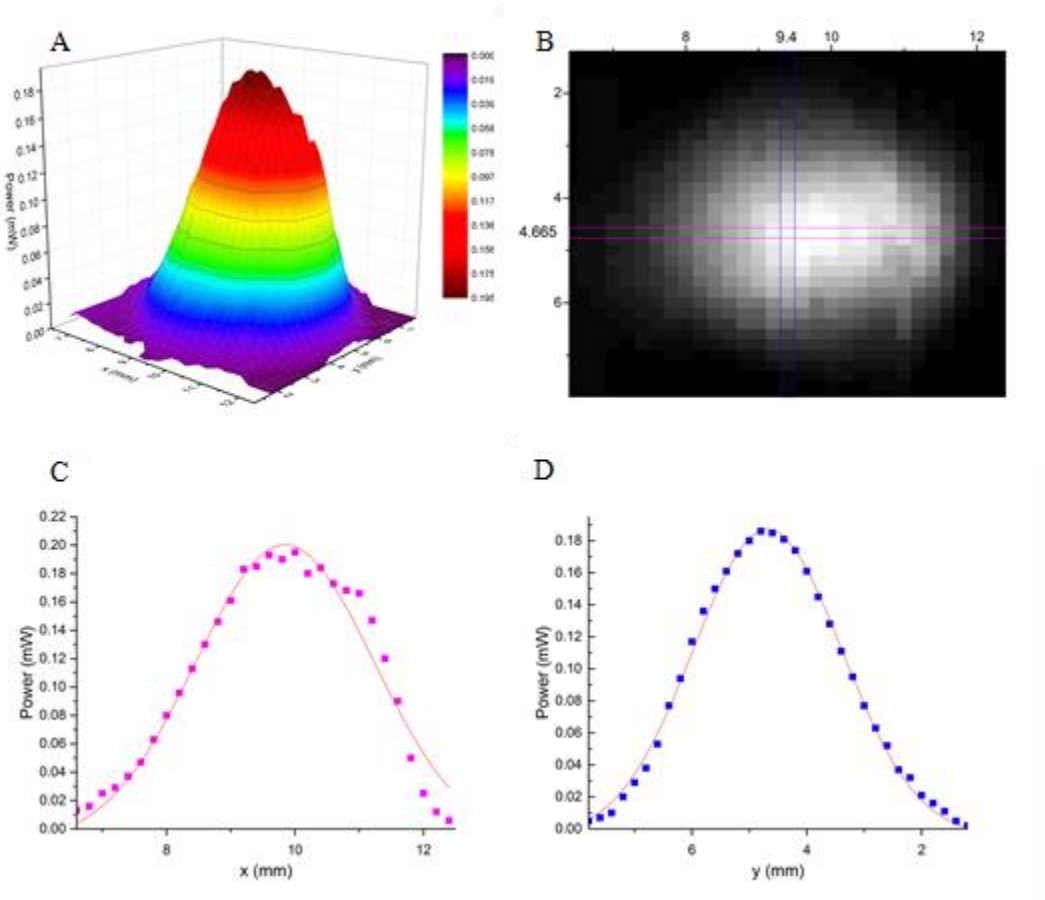

Figure 3.1.14 Beam profile of OPA output beam ($\lambda = 2.88\ \mu m$). A, 3D power distribution of the OPA output; B, 2D grey scale counterplot of power distribution; C, Gaussian fit of power distribution in the x direction (purple line in panel B); D, Gaussian fit of power distribution in the y direction (blue line in panel B).

3.1.4 Electronics in PIRL system

The application of PIRL system in imaging mass spectrometer requires the output pulses to be controllable to optimize the quality of the molecular map. A homemade Labview program was developed to control the pulsed ablation of the sample with both successive and burst mode options. If in burst mode, the number of pulses per burst, the delay between bursts as well as the repetition rate of the pulses within the burst could be controlled via the program. The layout of physical connection of electronics, a screen shot of the program, and the sequence of signals are shown in Figure 3.1.15, Figure 3.1.16 and Figure 3.1.17 respectively.

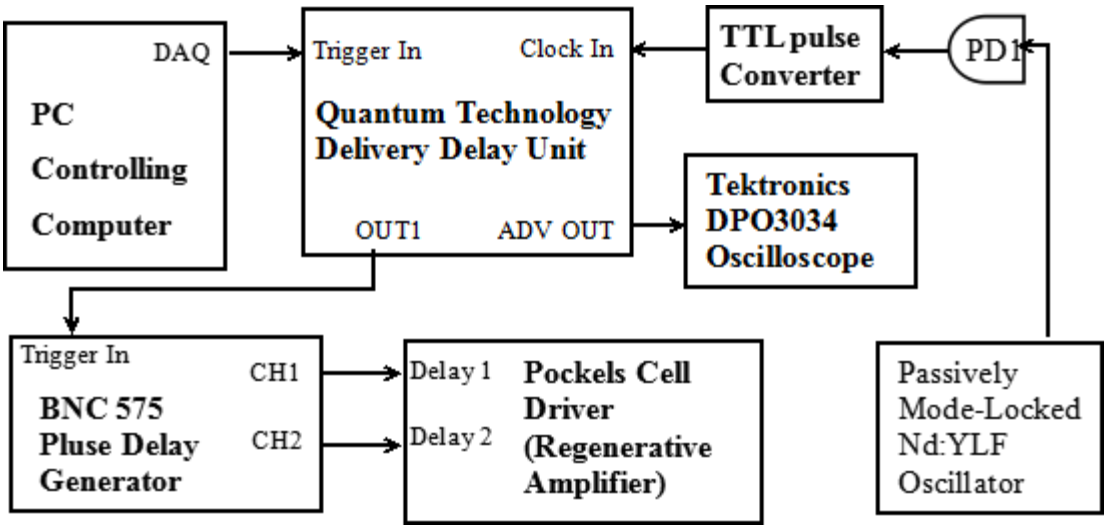

Figure 3.1.15 Layout of physical connections of electronics contolling PIRL system.

In Figure 3.1.15, the data card (DAQ, PCI-6601, National Instruments) was used to send out TTL pulse sequence as predefined by the Labview program shown in Figure 3.1.16. For example, as in Figure 3.1.16, 1 pulse was sent out within one burst at a repetition rate *Fr = 200 Hz*, and the dead time or delay time $T_D = 0$ *s* between bursts with 3 bursts being sent out in total. The TTL pulse sequence is shown in the bottom panel in Figure 3.1.17 while the second top panel shows two adjacent TTL pulses within one burst separated by a time that is the inverse of the repetition frequency $T_t = 1/F_r$. This pulse sequence triggered the Quantum Technology Delivery Delay Unit (QTDDU) which was clocked by pulses from the passively mode-locked Nd:YLF oscillator via a photodiode (PD, Thorlabs DET410) detecting photons leaked out of the cavity folding mirror in the oscillator (M1 in Figure 3.1.2), as shown in the top panel of Figure 3.1.17. The advanced output (ADV OUT) of QTDDU was sent to trigger the oscilloscope (Tektronics DPO3034) to monitor the Nd:YLF regenerative amplifier and OPA's performance during experiments. OUT1 of QTDDU thus sent TTL pulses synchronized with the Nd:YLF oscillator to trigger another pulse delay generator (Berkeley Nucleonics Cooperation Model 575). The delayed outputs of the BNC575 (*ΔT1* for CH1 & *ΔT2* for CH2) controlled the delay time of the Pockels Cell driver for maximum output pulse energy of the regenerative amplifier, top third panel in Figure 3.1.17. Once the Pockels Cell driver received a TTL pulse from CH1 of BNC575, it would apply high voltage on the Pockels Cell within a few ns. Since the seed of the regenerative amplifier was the output of the Nd:YLF oscillator, the same pulse train as shown in the top panel of Figure 3.1.17, the very first pulse from this train after the Pockel's Cell high

voltage applied was picked and trapped in the regenerative amplifier's cavity for amplification. In the case shown in the top sixth panel of Figure 3.1.17, the trapped pulse experienced 11 roundtrips inside the cavity to reach its saturation. The delay of CH2 (*ΔT2*, top four panel in Figure 3.1.17) was set to switch off the high voltage of the Pockels cell after the 10th roundtrip so that the trapped pulse can be released out of the amplifier's cavity after its 11th roundtrip for maximum output pulse energy, top five and six panel of Figure 3.1.17. In this way, the output of the amplifier and the output of OPA were synchronized with the trigger of BNC575, and was fully controlled by the Labview program. In the case shown in Figure 3.1.17, the PIRL system sent out 5 pulses at repetition rate F_r = *100 Hz*, and another 5 pulses after a 3 s dead time, and the last 5 pulses 3 s later.

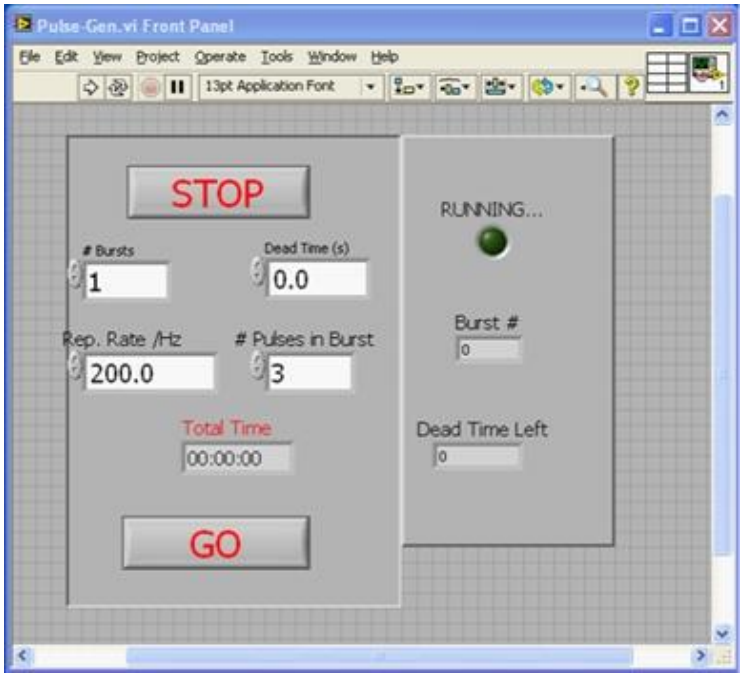

Figure 3.1.16 Screenshot of the Labview PIRL control program.

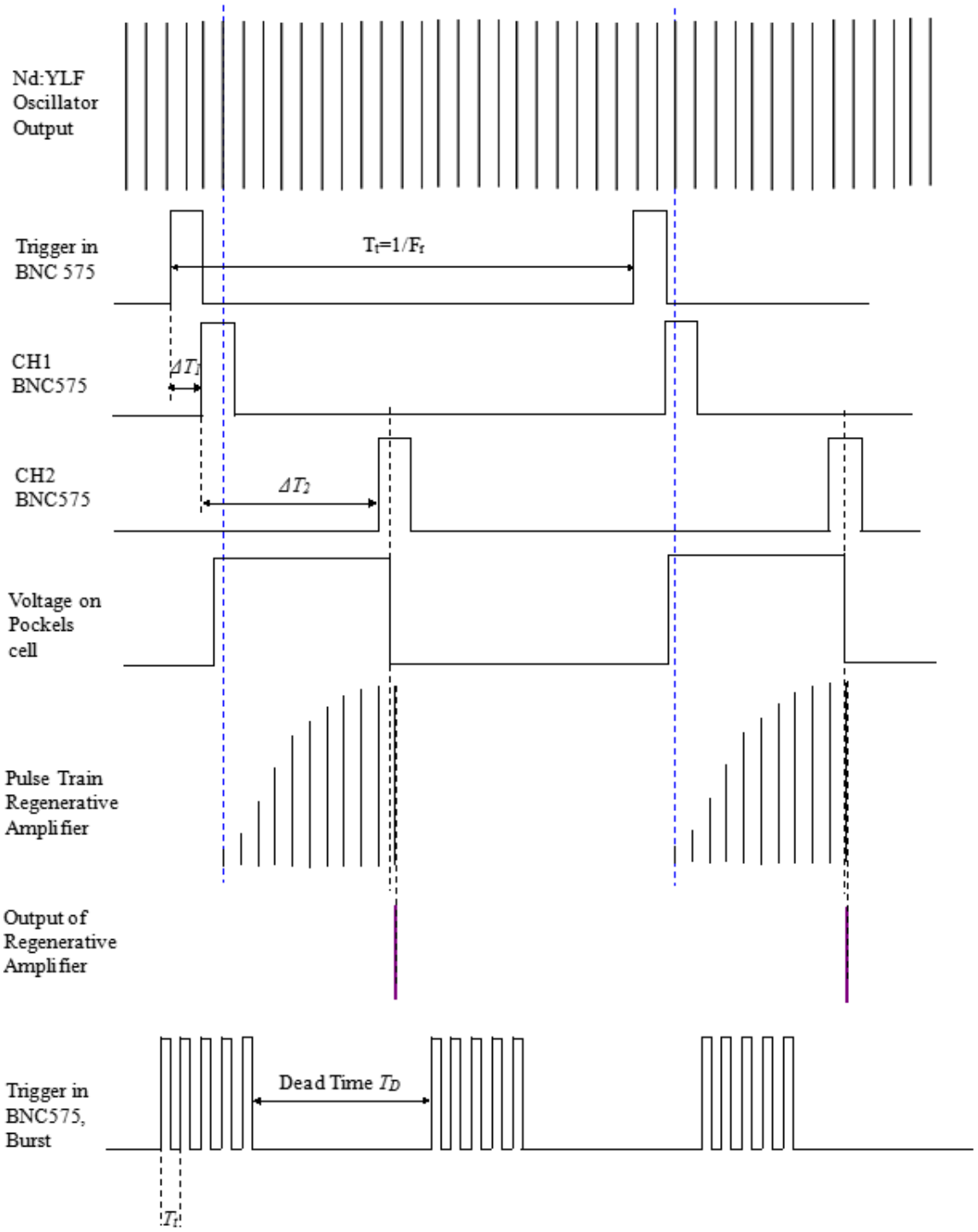

Figure 3.1.17 Sequence of outputs of electronics controlling PIRL system.

3.2 Picosecond Infrared Laser Ablation Electrospray Ionization (PIR-LAESI) Interface for Imaging Mass Spectrometry

A homemade mass spectrometer interface was designed for the tissue molecular mapping experiment. It was similar to the nanosecond version developed by the Vertes group at George Washington University [19] [20]. In addition to being able to perform tissue scanning, the interface was also flexible for switching between the PIR-LAESI experiment and the nanosecond LAESI experiment used for a direct comparison of PIRL and nanosecond infrared laser ablation.

3.2.1 Mass Spectrometer, Electrospray and the Geometry of PIR-LAESI Interface

Mass Spectrometer (MS)

The mass spectrometer (MS) used in the experiment was a quadrupole based orthogonal acceleration Time of Flight (TOF). It contained an ion source, three quadrupoles (Q0~Q2) and the TOF chamber that was orthogonal with the quadrupoles, as shown in Figure 3.2.1. The ion source was replaced by a home build electrospray interface for PIR-LAESI as discussed later. The first quadrupole Q0 focused and transferred ions from the ion source into the stubbies and the high vacuum region of Q1 which was the mass filter. In MS mode, both Q0 and Q1 were in RF only mode to transmit ions over a wide mass range with the voltage of Q0 a fraction of the RF voltage of Q1. In MS/MS mode, a DC voltage was added on the RF voltage in Q1 to only transmit a very narrow mass range (~ 1 Da) centered at the selected precursor ion. The third quadrupole Q2 was housed inside the collision cell where the precursor ions were fragmented into product ions via collision with N_2 gas in the cell. Q2 operated in an RF mode to transmit a wide range of *m/z* values.

Ions entered the time of flight chamber (TOF) from Q2 and were pushed down the TOF tube on an orthogonal trajectory relative to their initial path. Because ions with greater masses took longer to traverse the flight tube, the TOF section was used to measure the mass of each ion by recording the time reaching the detector located at end of the flight tube path. Once inside the TOF section, the ions followed a path based on the following sequence:

1. The ion beam entered the TOF pulsing region through a slotted ion aperture.

2. The applications computer sent a signal to activate the ion accelerator and began timing the ion flight. The ion accelerator pulsed, launching a 'slice' of ions from the ion stream down the flight tube (perpendicular to the ion stream) at a velocity which varied inversely with the square root of the mass (*m/z* ratio) of the ions [$v \propto (m/z)^{-1/2}$].

3. Midway through the ion flight, the ion mirror reversed the direction of the ions, correcting for small energy differences in the process.

4. As each ion in the "slice" reached the multichannel plate (MCP) connected with multimode detector, it sent an electrical signal to the time to digital converter (TDC) which recorded the time of detection.

5. According to a specified interval (pulser frequency is selected between 9 ~ 11 KHz so the 'slices' did not overlap), the applications computer sent another signal to the ion accelerator and started the sequence over again at step 2.

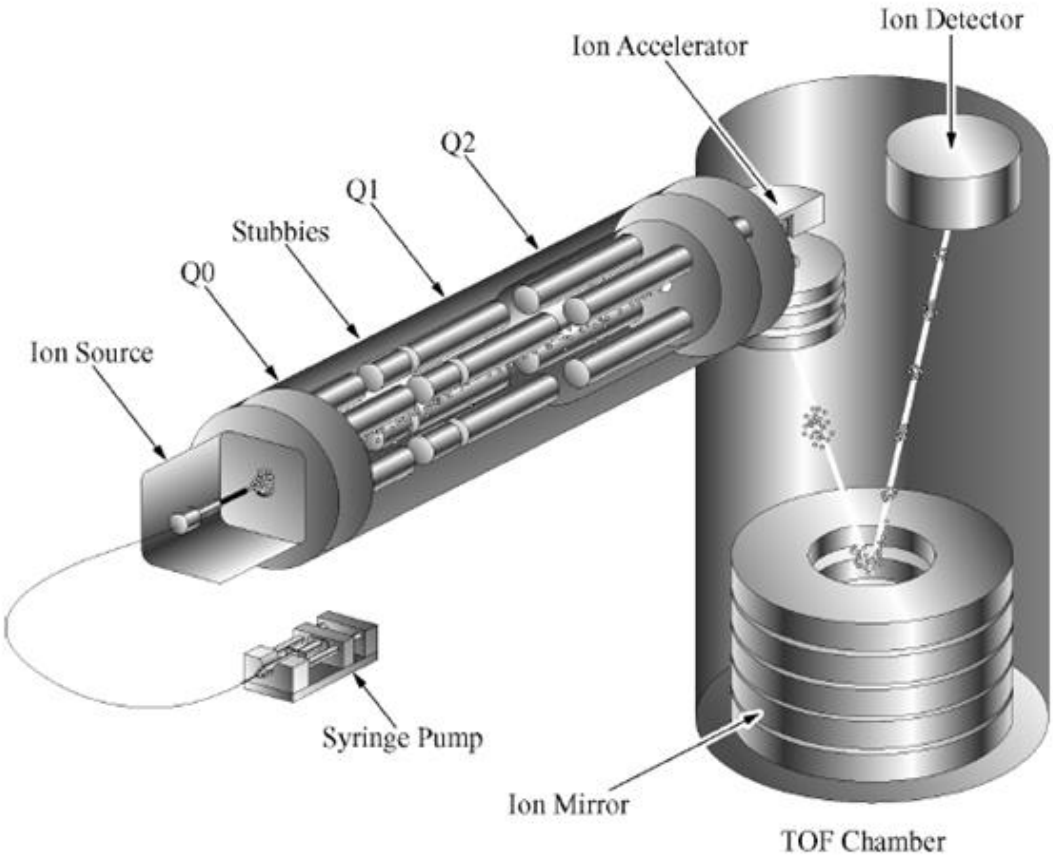

Figure 3.2.1 Ion path chamber in QSTAR Elite system.

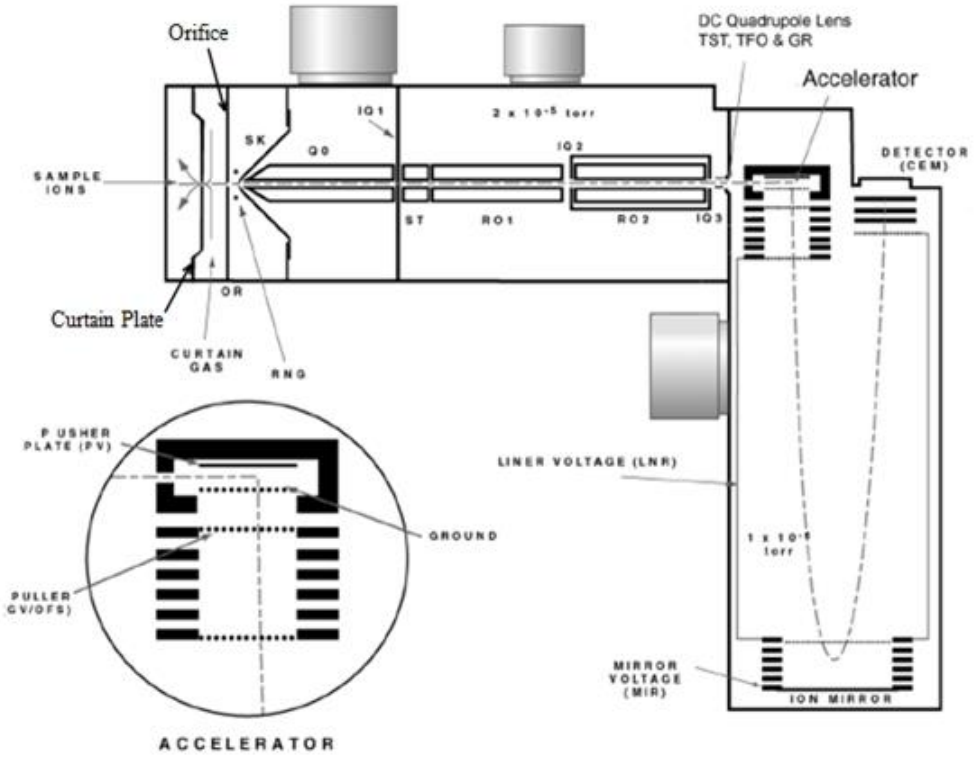

Figure 3.2.2 Ion optics to guide ions through ion path chambers in QSTAR Elite system.

Table 3.1 Ion Path Chamber Optics Components

Component	Description
Curtain Plate	Help maintain the vacuum interface
Orifice plate (OR)	Help maintain the vacuum interface and decluster the ions
Focusing ring (RNG)	Focus ions into the skimmer
Stubbies (ST)	Help transfer ions into the Q1 section
Interquad lenses (IQ1, IQ2, IQ3)	Help transmit ions into Q1, Q2, and the TOF sections respectively
DC Quadrupole lens (GR, TFO, TST)	Focus and steer ions into the TOF section

Electrospray (ESI)

The geometry of the ESI emitter is shown in Figure 3.2.3. The emitter was made of stainless steel blunt tube with *I.D = 125 μm* and *O.D = 2.0 mm*. One end of the tube was tapered down to a cone-shape with the *O.D = 150 ~ 200 μm* at the tip. The emitter was maintained at high voltage to charge the liquid solvent that was flowing through the tube with the flow rate maintained by

an electric controlled syringe pump. At the tip of the emitter, charged liquid was dispersed into a fine aerosol of multiply charged small droplets due to Coulomb repulsion. The charged aerosol droplets went through several cycles of solvent evaporation and Coulomb explosions leading eventually to isolated charged analyte molecules (single charged or multiple charged) that were introduced into the mass spectrometer for detection, as shown in Figure 3.2.4.

Figure 3.2.3 Geometry of ESI emitter.

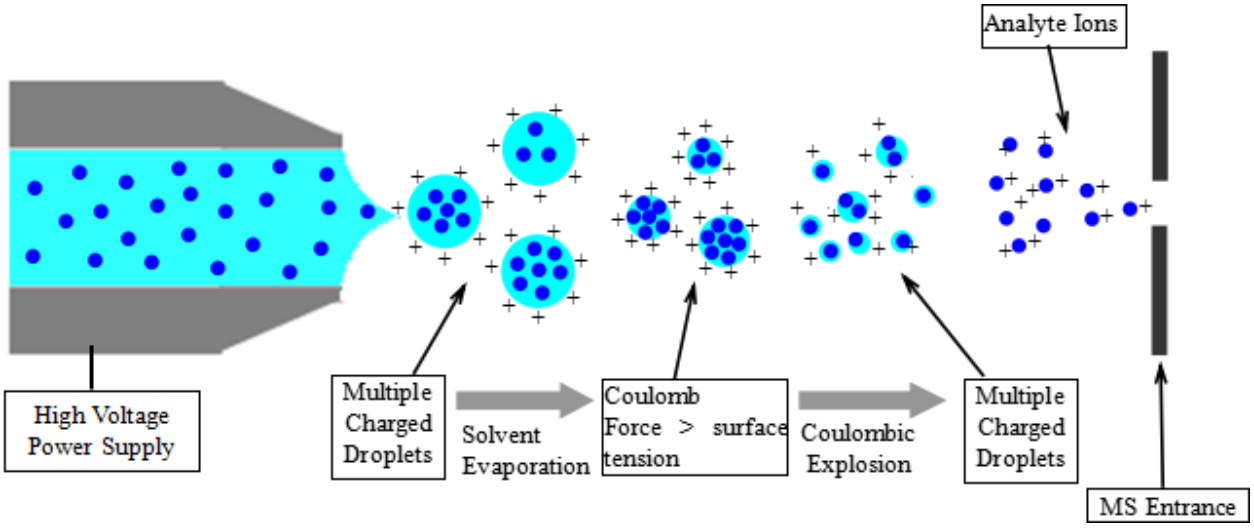

Figure 3.2.4 Ionization mechanism in traditional ESI process.

In PIR-LAESI, the ionization process is slightly different from the traditional ESI process. In traditional ESI, analyte molecules are in the solvent flow whereas in PIR-LAESI, analyte molecules are derived from ablation plume which intercepted the stream of the multiple charge solvent droplets. The solvent droplets dissolve the analyte and continues the solvent evaporation and columbic explosion process as in traditional ESI. The schematic of PIR-LAESI is shown in Figure 3.2.5. In this case the ions from the solvent serves as background ions and could be treated as an indicator of the stability of the spray. For tissue imaging experiments with the PIR-LAESI interface, a stable spray is necessary during the scan of the sample. Thus before any tissue imaging experiment, high voltage and flow rate were adjusted in order to stabilize the

steady spray mode with a Taylor cone appearing at the tip, as shown in Figure 3.2.6. The voltages used in our experiment were 3.0 ~ 4.0 kV with a flow rate of 1.5 ~ 2.0 μL/min.

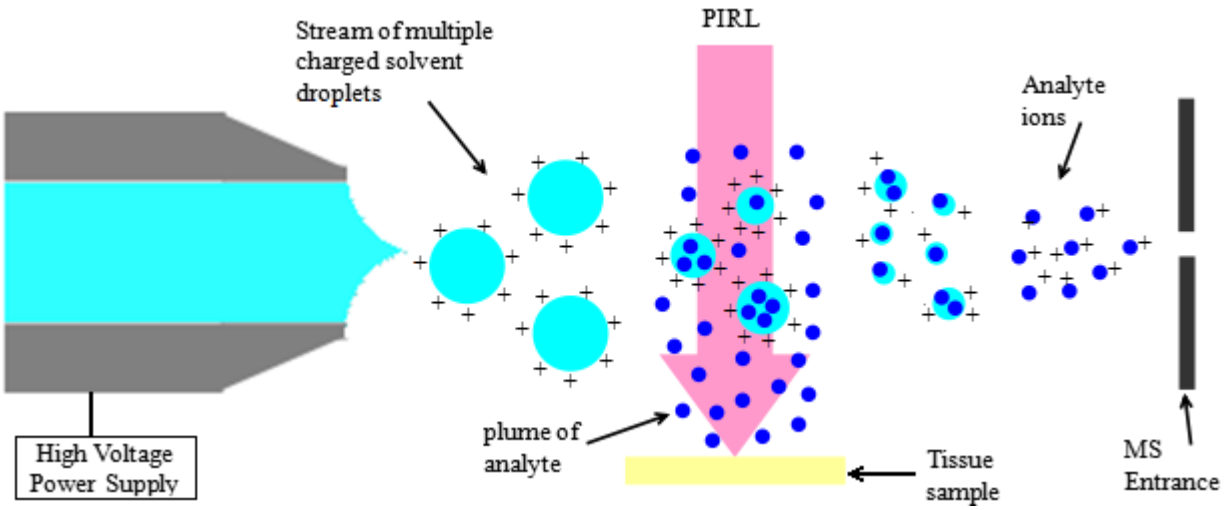

Figure 3.2.5 Schematic of PIR-LAESI ionization process.

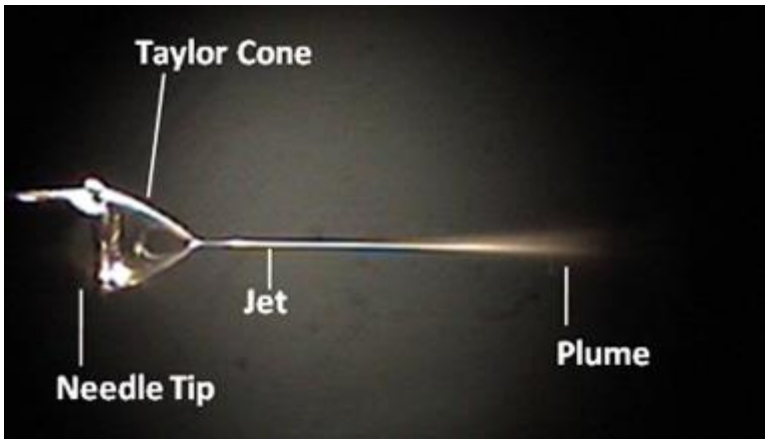

Figure 3.2.6 Steady electrospray with Taylor cone.

Geometry of the PIR-LAESI Interface

Figure 3.2.7 shows the scheme of the PIR-LAESI interface. A curtain gas (N_2) was applied during the experiment to prevent the contamination of the MS. The mid-IR beam was focused by $f = 100\ mm$ CaF_2 lens to a beam diameter of 100 μm at focus in front of the MS on a sample plate. The distance between the laser focus and the entrance of the MS were $x_{s\text{-}ms} = 5 \sim 8\ mm$ horizontally and $d_{s\text{-}ms} = 4\ mm$ vertically. The emitter of the ESI was mounted on the axis of the MS with its tip $x_{esi\text{-}ms} = 10 \sim 13\ mm$ away from the entrance of the MS. The solvent flowed through the emitter at a flow rate of $F_{esi} = 90\ \mu L/h$. A high voltage of about 3.0 kV was applied

to the emitter to maintain a steady Taylor cone shaped spray. A stainless steel sample plate was mounted on a 2D translational stage with a voltage of 400 V applied to enhance the ions collected by the mass spectrometer. The 2D translational stage was composed of two 1-D computer controlled stages from Physikinstrumente. They were mounted ~ 15 mm below and ~ 100 mm away from the MS entrance. An adaptor for the sample plate was attached on the 2D translational stages to satisfy the geometry shown in Figure 3.2.7. The sample plate was temperature controlled by a eltier element (TEC) to prevent the dehydration of sample during experiment.

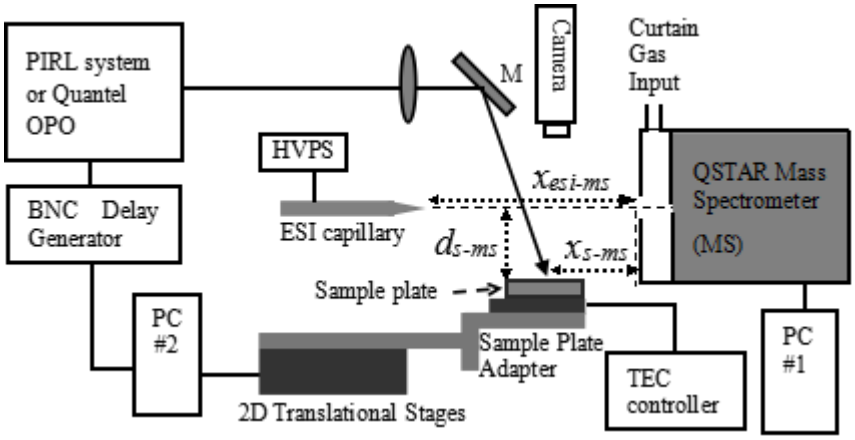

Figure 3.2.7 Setup for PIR-LAESI tissue imaging. OPA: optical parametric amplifier; L: CaF2 lens, f = 100 mm; M:Flat mirror, silver coated; HVPS: high voltage power supply for electrospray (ESI); xesi-ms: distance between the tip of ESI capillary and the entrance of MS along its axis; xs-ms: distance between ablation spot and the entrance of MS along its axis; ds-ms: vertical distance between the sample plate and the entrance of mass spectrometer;PC#1: computer controlling the MS and data acquisition; PC#2: computer synchronizing IR laser and 2D translational stages.

3.2.2 Sychronization of the 2D Translational Stages with the PIRL System

In order to perform the molecular tissue imaging experiment, the motion of the 2D translational stage has to be synchronized with the PIRL laser system. A homemade tissue imaging program (XYTissue_NIv2.vi, Labview 8.0) was developed for this purpose which integrated the PIRL control program discussed in Section 3.1.4. A screen shot of the program's control interface is shown in Figure 3.2.8. Before acquisition, the scan range on the sample was determined by monitoring the camera (Figure 3.2.7), $(x, y) = (x_{start}, y_{start}) \sim (x_{stop}, y_{stop})$ as shown in Figure 3.2.8 with a step size x_{step}, y_{step} in each direction respectively. The PIRL control program is shown under the "Laser Firing" panel. The '# pulses in Burst' defined the total number of pulses at each

spot or pixel with a certain repetition rate. “Delay/ms” was the dwell time of the 2D stages at each spot after the laser firing was complete. Controls were further incorporated for the selection of PIR-LAESI (‘Pico-only’) from the ‘Laser Selector’ in the left bottom panel and ‘Nano-only’ for nanosecond IR OPO for ns-LAESI experiments. Once these pre-defined parameters were selected and the ESI operating in Taylor cone mode, the 2D acquisition was ready to start.

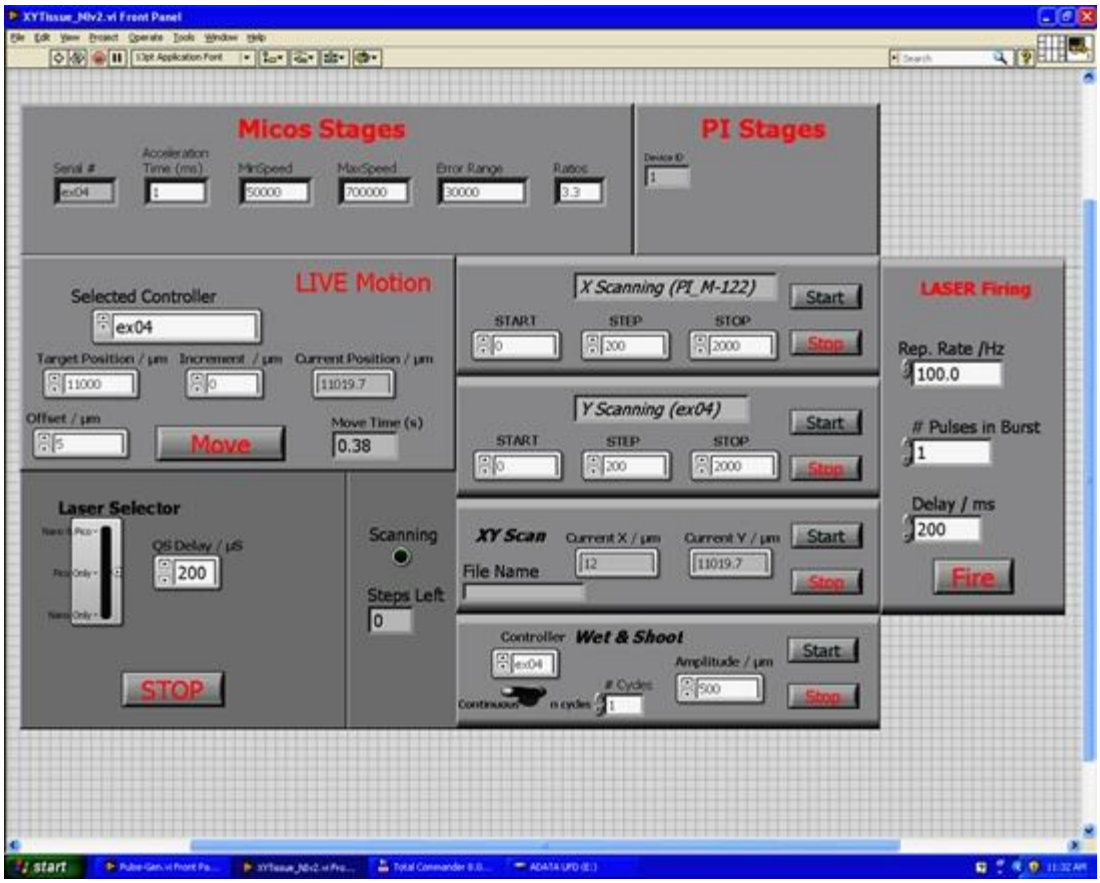

Figure 3.2.8 Labview interface of control PIRL laser and 2D translational stages.

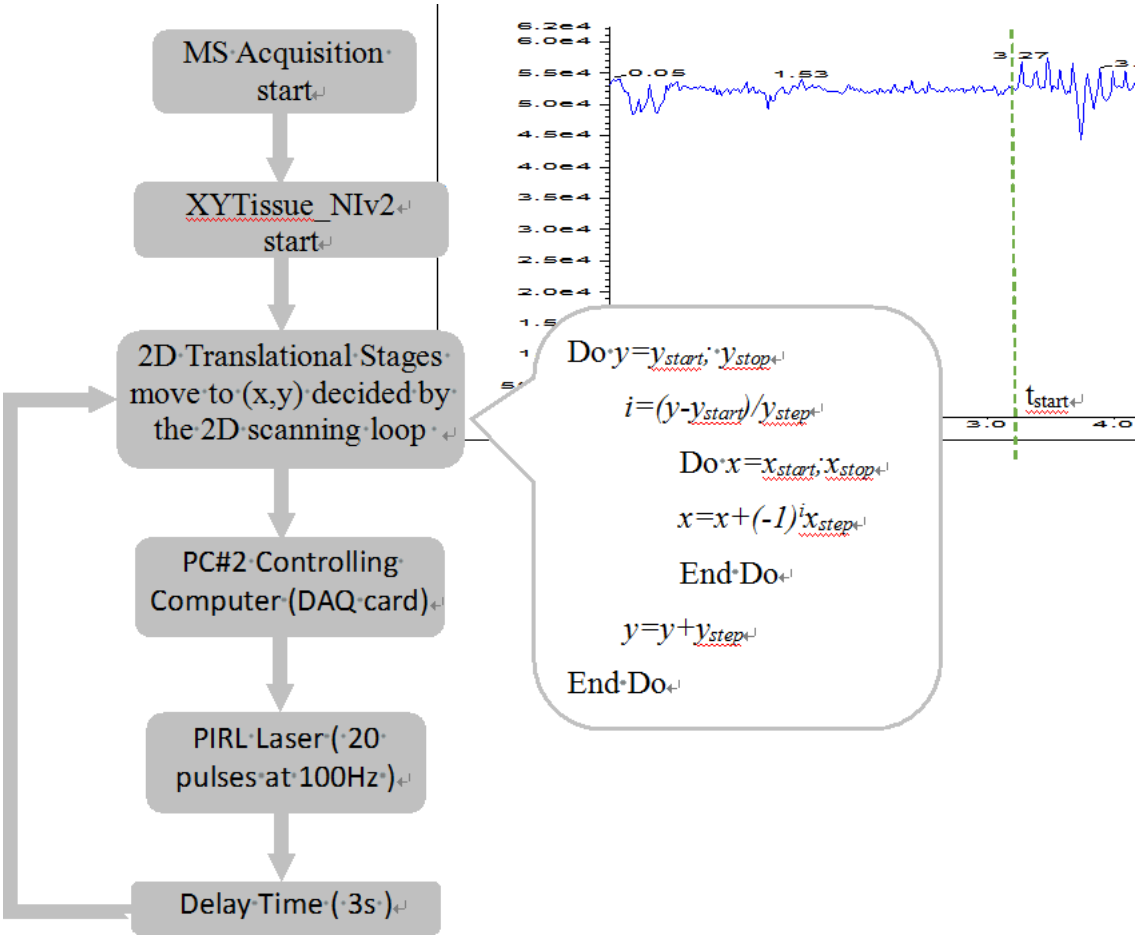

Figure 3.2.9 Sequence of Event of PIR-LAESI imaging MS experiment.

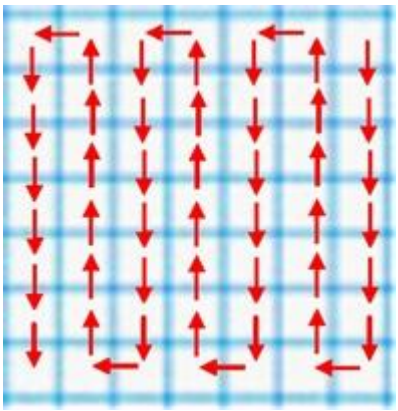

Figure 3.2.10 Route of PIRL shooting on samples during imaging MS experiment.

Figure 3.2.9 shows the layout of the sequence of events. Once the XYTissue_NIv2.vi program and the acquisition software of MS were set for acquisition, the MS acquisition program was started and the electrospray monitored for a few minutes to insure it was stable. The 'Start'

button on the “XY Scan” panel in the XYTissue_NIv2.vi program was then pressed to start a 2D scan while the time on the MS acquisition software was recorded for reconstruction of the molecular map by pressing “Start” t_{start} (Figure 3.2.9 insert). The 2D translational stages moved to the first pixel (x_{start}, y_{start}) following “Start”. The DAQ card (PCI-6601, National Instruments) in PC#2 sent a burst of TTL pulses predefined by the parameters set in the “Laser Firing” panel to trigger the PIRL. Once the PIRL pulses finished firing, the stages waited for the defined time (“Delay/ms”) for the ESI to washout/ionize the ablated plume from the current pixel. Once the dwelling time was completed, the stages moved to the next pixel, e.g. (x_{start}+ x_{step}, y_{start}). The scanning was realized by a scanning loop with the stages moving along *x* axis first and then a *y* axis shift after finishing each row on *x* axis, as shown in Figure 3.2.10. The purpose of the delay time was to eliminate the overlapping of signals from the previous spot, so that when PIRL shot a new spot there was no remaining plume from the previous ablation spot. The delay time was minimized to retain a reasonable total scan time. In the presented experiment, the delay time was usually set to be 3 s and 20 pulses per spot at 100 Hz, resulting in a total dwelling time at each spot of 3.2 s. For a scan area of 5 mm × 5 mm with step size 200 μm, there were 676 spots (pixels) in total corresponding to a total scan time of 36.05 minutes.

References of Chapter 3

[1] K. Franjic, “Studies of Laser Ablation of Liquid Water under Conditions of Impulsive Heat Deposition through Vibrational Excitations (IHDVE),” Ph.D thesis, 2010.

[2] J.Cummings, and J. Walsh, “Erbium laser ablation: The effect of dynamics optical properties,” Appl. Phys. Lett., vol. 62, no. 16, pp. 1988–1990, Apr. 1993.

[3] M. Skorczakowski, J. Swiderski, W. Pichola, P. Nyga, A. Zajac, M. Maciejewska, L. Galecki, J. Kasprzak, S. Gross, A. Heinrich, and T. Bragagna, “Mid-infrared Q-switched Er:YAG laser for medical applications,” Laser Phys. Lett., vol. 7, no. 7, pp. 498–504, Jun. 2010.

[4] M. Skórczakowski, W. Pichola, J. Świderski, P. Nyga, L. Galecki, M. Maciejewska, A. Zając, S. Gross, A. Heinrich, T. Bragagna, and J. Kasprzak, “30 mJ, TEM00, high repetition rate, mechanically Q-switched Er:YAG laser operating at 2940 nm,” Opto-Electron. Rev., vol. 19, no. 2, Jan. 2011.

[5] M. N. Satyanarayan, A. Deepthy, and H. L. Bhat, “Potassium Titanyl Phosphate and Its Isomorphs: Growth, Properties, and Applications,” Crit. Rev. Solid State Mater. Sci., vol. 24, no. 2, pp. 103–191, Jun. 1999.

[6] C. Nelson and J. Crist, “Predicting laser beam characteristics: mode quality (M2) measurement improves laser performance,” Laser Tech. J., vol. 9, no. 1, pp. 36–39, Jan. 2012.

[7] G. Anstett, A. Borsutzky, and R. Wallenstein, “Investigation of the spatial beam quality of pulsed ns-OPOs,” Appl. Phys. B-Lasers Opt., vol. 76, no. 5, pp. 541–545, May 2003.

[8] R. Urschel, A. Borsutzky, and R. Wallenstein, “Numerical analysis of the spatial behaviour of nanosecond optical parametric oscillators of beta-barium borate,” Appl. Phys. B-Lasers Opt., vol. 70, no. 2, pp. 203–210, Feb. 2000.

[9] W. Koechner, Solide-State Laser Engineering, Fifth Edition. Springer Science + Business Media, LLC, 2005.

[10] H. Haus, “Parameter ranges for CW passive mode locking,” IEEE J. Quantum Electron., vol. 12, no. 3, pp. 169–176, Mar. 1976.

[11] C. Hönninger, R. Paschotta, F. Morier-Genoud, M. Moser, and U. Keller, “Q-switching stability limits of continuous-wave passive mode locking,” J. Opt. Soc. Am. B, vol. 16, no. 1, p. 46, Jan. 1999.

[12] U. Keller, K. J. Weingarten, F. X. Kartner, D. Kopf, B. Braun, I. D. Jung, R. Fluck, C. Honninger, N. Matuschek, and J. Aus der Au, “Semiconductor saturable absorber mirrors (SESAM’s) for femtosecond to nanosecond pulse generation in solid-state lasers,” IEEE J. Sel. Top. Quantum Electron, vol. 2, no. 3, pp. 435–453, Sep. 1996.

[13] T. R. Schibli, E. R. Thoen, F. X. Kärtner, and E. P. Ippen, “Suppression of Q-switched mode locking and break-up into multiple pulses by inverse saturable absorption,” Appl. Phys. B, vol. 70, no. S1, pp. S41–S49, Jun. 2000.

[14] P. Černý, G. Valentine, D. Burns, and K. McEwan, "Passive stabilization of a passively mode-locked laser by nonlinear absorption in indium phosphide," Opt. Lett., vol. 29, no. 12, p. 1387, 2004.

[15] R. Paschotta, Field Guide to Laser Pulse Generation. SPIE Press, 2008.

[16] J.-Y. Zhang, J. Y. Huang, and Y. R. Shen, Optical Parametric Generation and Amplification. CRC Press, 1995.

[17] K. Vodopyanov, "Pulsed Mid-IR Optical Parametric Oscillators," in Solid-State Mid-Infrared Laser Sources, vol. 89, I. T. Sorokina and K. L. Vodopyanov, Eds. Berlin, Heidelberg: Springer Berlin Heidelberg, 2003, pp. 144–183.

[18] J. E. Bjorkholm and H. G. Danielmeyer, "Frequency control of a pulsed optical parametric oscillator by radiation injection," Appl. Phys. Lett., vol. 15, no. 6, pp. 171–173, Sep. 1969.

[19] P. Nemes, A. A. Barton, Y. Li, and A. Vertes, "Ambient Molecular Imaging and Depth Profiling of Live Tissue by Infrared Laser Ablation Electrospray Ionization Mass Spectrometry," Anal. Chem., vol. 80, no. 12, pp. 4575–4582, Jun. 2008.

[20] A. Vertes, P. Nemes, B. Shrestha, A. A. Barton, Z. Chen, and Y. Li, "Molecular imaging by Mid-IR laser ablation mass spectrometry," Appl. Phys. A, vol. 93, no. 4, pp. 885–891, Jul. 2008.

Chapter 4
Characterization of the Picosecond Infrared Laser Ablation Electrospray Ionization (PIR-LAESI) Imaging Mass Spectrometer

4.1 DIVE Ablation Dynamics on Biological Samples

Following the invention of a new type of pulsed laser, researchers are eager to investigate its application to medicine. This is primarily due to lasers' potential to manipulate and destroy biological tissue precisely and selectively [1] [2]. Laser destruction that includes the removal or incision of biological tissue is known as ablation. Lasers that can drive an ablation process have been widely used in laser surgeries and biological analysis, among which the mid-IR laser is common as water is the main photon absorber. Understanding the ablation mechanism is critical for proper design of medical instruments based on the laser technology. However, to date only IR lasers with long pulse duration pulses (> 1ns) have been well studied. Vogel.et al. has studied the ablation dynamics of Er.YAG lasers ($\lambda = 2.94\ \mu m$) on different biological tissues with pulse durations of 200 μs [3] and 70 ns [4]. These studies show that laser characters such as pulse duration and fluence as well as the physical properties of the biological tissues (mechanical, thermal and optical etc.) influence the ablation mechanism and plume propagation. The DIVE ablation process driven by the PIRL system has only been studied numerically and experimentally for liquid water [5]. The ablation dynamics driven by the PIRL system on biological tissue with different physical properties has not been investigated to our knowledge. Here, the experimental study of the ablation dynamics is presented by taking high speed snapshots of the ablation plume at time intervals after the irradiation of a PIRL pulse on different tissue samples, such as liquid water, ice, Agarose gel, pig skin and tendon.

4.1.1 Experimental Setup

In order to gain insight to the dynamics of the ablation plume driven by the PIRL pulse, time resolved dark field imaging microscopy (DFIM) techniques were used to produce images with high contrast and high spatial resolution without sacrificing the required sensitivity. The method allows the detection of small differences in the refractive index of the expanding water vapor and air shock waves over small interaction lengths between the illumination light and the ablation

plume [6]. The principle of DFIM has been well described by Vogel et al. [7]. In DFIM, non-scattered light from the illumination source is blocked and only the light scattered by the plume is collected. The generated image thus has a black background with the scattering plume shown as bright, opposite to an image generated by a bright field imaging microscope. The scheme of the setup was similar to the one used in the study of the ablation dynamics of liquid water [5] and is shown in Figure 4.1.1.

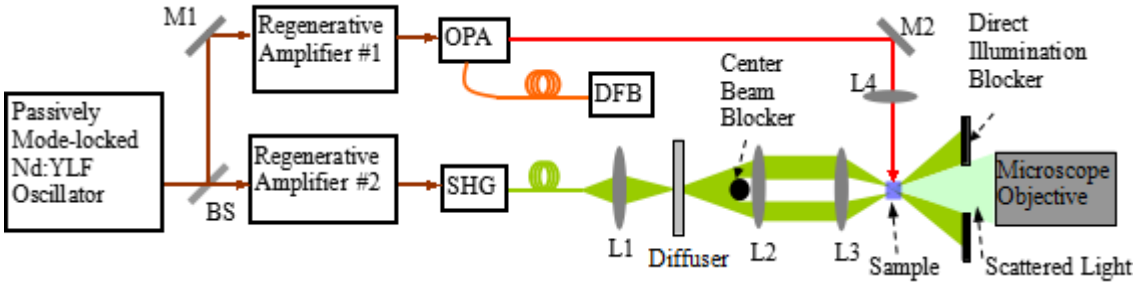

Figure 4.1.1 Setup of Dark Field Imaging Microscope for ablation plume dynamics study. BS, 50:50 beam splitter for 1.053 μm; M1, flat mirror high reflective coated at $\lambda = 1.053\ \mu m$; M2, flat mirror high reflective coated at $\lambda = 2.94\ \mu m$; L1~L3 BK7 lens $f = 40\ mm$; L4, CaF_2 lens $f = 100\ mm$; OPA, optical parametric amplifier; SHG, second harmonic generation; DFB, distributed feedback diode laser.

In Figure 4.1.1, the output of the passively mode-locked Nd:YLF oscillator described in Section 3.1.1 was split by a 50:50 beam splitter to seed both regenerative amplifiers. The mid-IR beam generated from the PIRL system described in Section 3.1 was focused onto the sample by a CaF_2 lens of $f = 100\ mm$. The incidence angle of the beam on the sample was approximately 45^0 degrees, resulting in an elliptical focus spot with 100 μm and 141 μm diameters ($1/e^2$ level) of the short and long axis. Given the PIRL system output pulse energy of 120 μJ, the fluence that stimulated the ablation process was 1.083 J/cm^2. The illumination source was generated by the second Nd:YLF regenerative amplifier with an output pulse energy of 1.5 mJ, which was then converted to its second harmonic (SHG) $\lambda = 526\ nm$ by a 10 mm long LBO crystal. The green beam was coupled into a 1.5 m long multimode fiber to reduce both spatial and temporal coherence to eliminate speckles from a coherent illumination source which may blur the generated image. The output of the fiber was focused onto a diffuser (Thorlabs, DG10-1500) by a BK7 lens $f = 40\ mm$ (L1) for further reduction of spatial coherence. The focal spot at the diffuser acted as the microscope light source. A metal rod with diameter 3 mm was placed in front of a lens group composed by two BK7 lenses (L2, L3, both $f = 40\ mm$) to block the center part of the illumination. In this way, only the green shaded part in Figure 4.1.1 from the

illumination source was focused on the sample and scattered by the plume. The non-scattered part of the illumination (green shade, Figure 4.1.1) was blocked by an opaque plastic mask whereas only the light scattered by the plume (light green shade, Figure 4.1.1) was collected by a long distance microscope with 22X nominal magnification and 5 cm effective working distance (Infinity Photo-Optical Company, model K2 with CF-4 objective). The fine position adjustment of the metal rod and the opaque plastic mask was made by trails and errors to get the optimal image. The image was recorded by a digital camera (Nikon D3200) with camera settings optimized for image quality. The time delay between the imaging event and the ablation event was controlled by computer with a four channel delay generator (Berkeley Nucleonics Cooperation Model 575, BNC575). Each image was taken for a single shot ablation event.

4.1.2 Materials Preparation

Ablation plume dynamics was studied with the dark field imaging setup on samples with different physical properties. The samples included liquid water, ice, 1% Agarose gel, and pig skin as well as pig tendon.

Ice, as the solid version of water, is mechanically stronger than liquid. The energy needed to ablate the same volume of ice as liquid water is larger since extra energy is needed to melt the ice and break its structure. The IR absorption of ice and liquid water are also different with the liquid water absorption maximum at $\lambda = 2.94\ \mu m$ and ice at $\lambda = 3.049\ \mu m$ [8]. Based on this less recoil-induced ejection of droplets was predicted in the ablation of ice compared with liquid water. The water sample was kept in an overfilled 4 mm wide metal channel; so a well-defined meniscus was formed with the infrared spot focused at the top of the meniscus. For ice, the water sample was prepared as liquid and then put into the freezer at a temperature of -20^0C for half an hour. During the experiment, the metal channel was fixed on a metal blocks which was located in a bath of dry ice to prevent the melting of the ice sample at room temperature.

As a mimic of soft biological materials, agarose gel was prepared with a water mass concentration of 99%. Agarose powder (Sigma Aldrich, Oakville, ON, Canada) was mixed with liquid water and heated on a heat disk to boil. The boiling lasted for 20 minutes to allow the agarose powder to fully melt and mix with the water. 5 mL of the mixed liquid was poured into a 4-inch petri dish and left to uniformly spread to form gel layer of about 400 μm thickness. A small slice of 3 mm × 10 mm was cut and removed for the experiment.

Tendon and skin have inherently different mechanical properties due to their difference in water and collagen content. Figure 4.1.2 shows the stress-strain curves characterizing their mechanical properties under uniaxial tension [9]. Tendon is a tissue that possesses high collagen content and thus is very strong and stiff, with an ultimate tensile strength (UTS) > 100 MPa and a fracture extensibility of 10%. Skin, with less collagen content and more water content, is relatively softer and more extensible with a UTS of about 10 MPa and a fracture extensibility of 45%. Samples of pig tendon and pig skin were cut from a pig foot bought from local grocery store. The pig foot was stored in a freezer at -20^{0}C until the experiment took place.

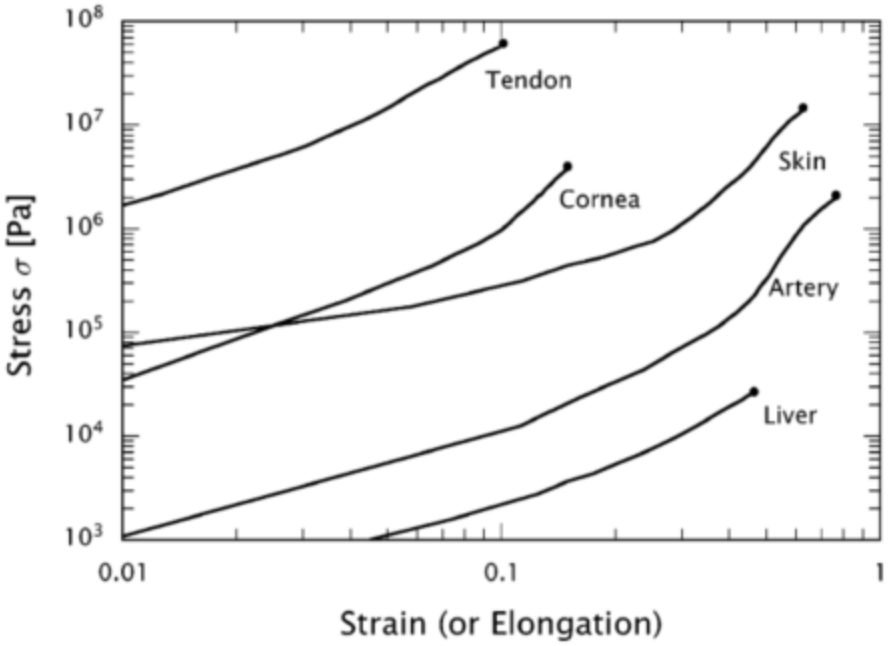

Figure 4.1.2 Stress-strain curves characterizing the mechanical properties of various biological tissues under uniaxial tension. The ● symbols represent the mechanical state at which tissue fracture occurs. Reprinted with permission from ref. [9]. Copyright © 2003 American Chemical Society.

4.1.3 Results and Discussion

Figure 4.1.3 and Figure 4.1.4 show representative dark field images of the plume expansion after PIRL ablation of liquid water and ice respectively with a 108 ps pulse duration and the incident fluence of 1.08 J/cm^2. The brighter background in Figure 4.1.4 comes from the stronger scattering of the ice surface due to the meniscus deformation induced in the freezing process. For both liquid water and ice, the ablation started with a vapor explosion caused by the fast energy deposition into the sample. Since the energy was deposited on a time scale shorter than the pressure dissipation time scale in the media, all the energy absorbed from the pulse was localized

within a confined volume defined by the incident area and the penetration depth of the pulse in the sample, resulting in a very intense volumetric energy density. When the energy density is higher than the vaporization enthalpy of water (or the sum of fusion and vaporization enthalpy in the case of ice), the water within the confined volume will be explosively vaporized. The transparent upper portion of the plume indicates the complete vaporization of water. The plume from ice ablation had a larger portion of gas-phase molecules since almost the entire plume is transparent in the image of 100 ns delay. Due to the fast propagation speed of the plume, the gas-phase molecules in the front part of the plume collided with air molecules and formed a shockwave with a typical mushroom shape. The bright spot on the apex of the shockwave shown in the image of 100 ns delay indicates much stronger longitudinal momentum than transverse momentum which was not observed in the ablation with longer pulse duration (70 ns) [4][5].

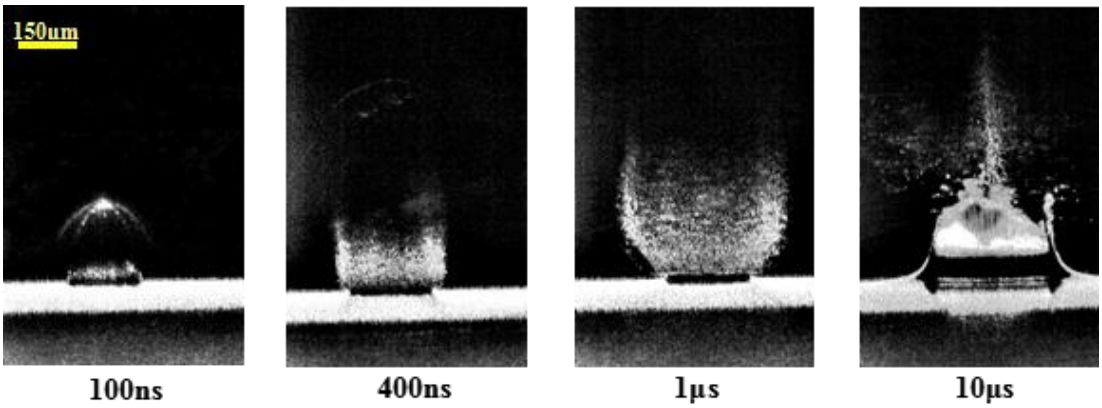

Figure 4.1.3 Dark field images of ablation plume dynamics of liquid water excited by PIRL pulse.

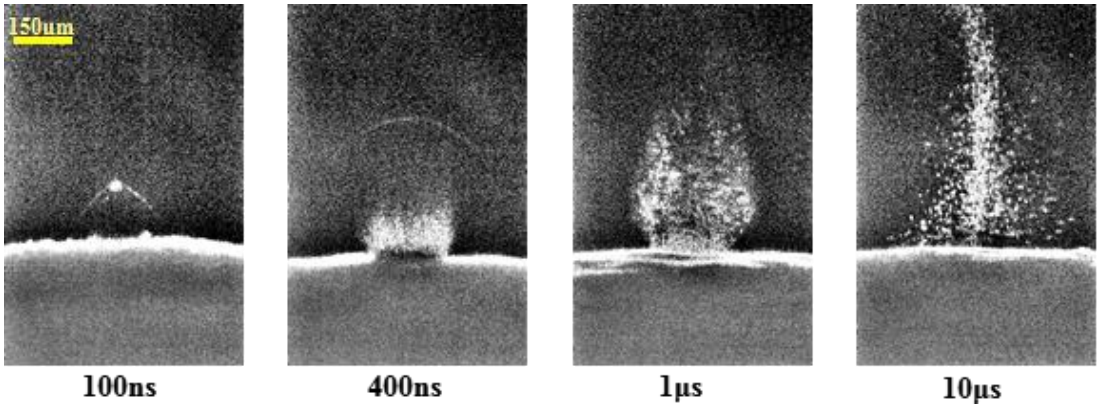

Figure 4.1.4 Dark field images of ablation plume dynamics of ice excited by PIRL pulse.

As the plume propagated further, the speed of the gas-phase molecules decreased via collision with air molecules thus the shockwave became less visible at longer time delays (400 ns) and

disappeared 1 μs after laser irridation The energy deposited into the confined volume was dissipated into the surrounding media so that the energy density in the confined volume was reduced to less than the required for vaporization, resulting in the ejection of small droplets as shown in the images collected at 400 ns and 1 μs delay in both liquid water and ice.

The deposited energy also induces acoustic wave propagation inwards in the case of liquid water which leads to the ejection of large droplets and turbulence on liquid surface, thus the process called recoil can be seen in the image collected at 10 μs delay in Figure 4.1.3. In the case of ice, the pressure required to disrupt its structure is much higher so only small droplets were ejected even at 10 μs delay (Figure 4.1.4) without recoil as predicted. The distribution of small droplets at 10 μs delay for ice showed a similar property as the upper portion of the image in the liquid case at the same time delay. The density of the small droplets in the center was much higher than the two sides and different from the images at earlier time delays. This is because the energy distribution in the incident pulse was Gaussian at the earlier stages of ablation and the central portion of the confined-volume still retained enough energy for vaporization whereas the edges only had energy sufficient for droplets ejection. This is illustrated by the middle portion of images having a downwards curvature of the bright/black part, especially in the case of liquid water (400 ns and 1 μs delay). As energy dissipation proceeded, the center of the confined-volume did not contain enough energy for vaporization either so only droplets were ejected whereas the energy in the edges was not sufficient enough for efficient droplets ejection. We did not observe any “inner shock waves” as reported by Apitz and Vogel in case of water ablation with 70 ns pulses [4].

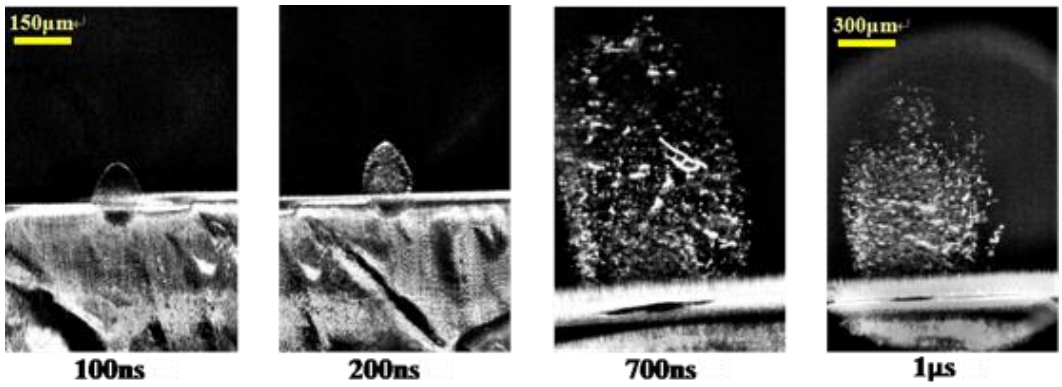

Figure 4.1.5 Dark field images of ablation plume dynamics of 1% agarose gel excited by PIRL pulse.

The dark field image of the PIRL driven ablation process on Agarose gel with an agarose mass concentration of 1% is shown in Figure 4.1.5, with the image collected at a time delay of 1 μs and taken with half of the magnification as compared to images of earlier time delays. Similar as the case of liquid water and ice, the transparency in the upper portion of the plume at a delay time of 100 ns indicates the complete vaporization of water inside the gel. However, no bright spot was observed in the image, indicating the gas-phase molecules gained less longitudinal momentum from the pulse than in the case of liquid water and ice. At a time-delay of 200 ns, the entire plume was filled with small droplets, indicating the reduction of the volumetric energy density. As the deposited energy further dissipated into the surrounding media, fragments of agarose gel with a size larger than 10 μm were ejected, as shown in Figure 4.1.5 at a time delay of 700 ns and 1 μs. The ejection of fragments in earlier time delays reflects that the agarose gel is more easily disrupted as compared to the solid ice substrate.

Dark field images following ablation of pig skin and pig tendon are shown in Figure 4.1.6 and Figure 4.1.7. The early delay time (100 ns) showed that only fragments of skin and tendon were ejected under the present irradiation conditions. In the previous study of ablation with a pulse duration of 70 ns [4], the authors showed that the plume initially consisted of only gas phase molecules in the case of pig skin (cut from pig ear) ablated with the irradiation fluence 5 times higher than used in the present experiment. The study did not investigate the ablation of the skin sample under similar fluence as described here. However, they did irradiate pig liver which is softer than skin with a fluence both similar to and 5 times higher than the fluence used in the present study. Their results showed the plume only consisted of small liver fragments for the lower fluence ablation and the presence of gas phase molecules for higher fluence irradiation. Those results implied the fluence is very important to the plume composition in the ablation process. We believe with higher fluence, it is also possible to generate a plume with gas-phase molecules. In the images with longer time delays, small fragments continued to propagate and larger particulates (>10 μm) were ejected in the case of pig skin starting from 1 μs after the incidence of PIRL pulse. In the case of pig tendon, the main composition of the tissue was bundles of collagen fibers which are very strong and mechanically stiff. The ejection in the later time delay mostly contained pieces of these collagen fibers which can already be seen in the images at a 400 ns time delay.

The presence of gas-phase molecules in the ablation plume give insight for the design of new ion sources for Mass Spectrometer with the capability of quantitative analysis. The bottleneck to achieve quantitative analysis is ion suppression due to chemical ionization in the ion source such as ESI, MALDI, APCI, etc. To eliminate ion suppression process, ion sources based on physical ionization are needed which require the analytes being in the gas-phase intact if the analytes are already charged in the original sample or intact and neutral if post-ionization is needed. The ablation dynamics presented here imply the possibility for the development of such an ion source. Large droplets from recoil-induce ejection must be eliminated to produce a clean environment for ions from post-ionization to survive. For samples such as biological fluids (blood, urine etc.), frozen samples are a better choice relative to the liquid phase due to less recoil and the larger portion of gas-phase molecules in the plume. Reduction of the sample volume to the size of the energy confined volume will also eliminate the ejection of small droplets and large droplets from recoil. Picoliter nanowell chips have been designed for this purpose and ion sources based on the chips are now under development [10]. For samples of biological tissues, in the application of off-line surgery biological diagnosis, the samples can be sliced into sub-10 μm thick slices by cryotome and the PIRL fluence is adjusted to be large enough to bring the tissue into gas phase for ionization. For in vivo diagnosis of biological tissues during clinical operations, the effects of high fluence ablation must be considered, such as two photon photo-chemical reactions and plasma formation which can produce toxic chemicals [9].

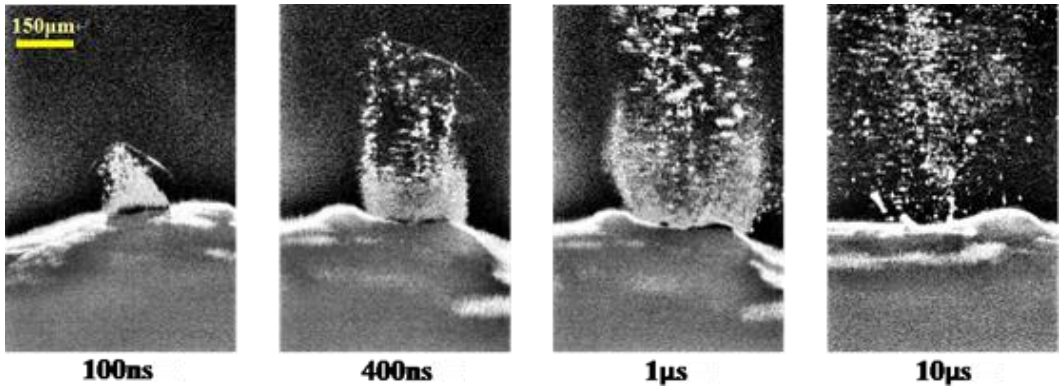

Figure 4.1.6 Dark field images of ablation plume dynamics of pig skin excited by PIRL pulse.

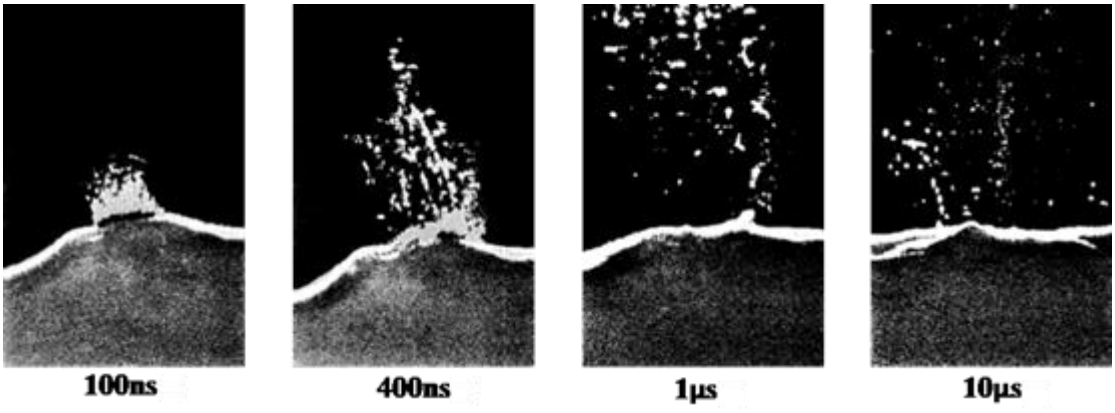

Figure 4.1.7 Dark field images of ablation plume dynamics of pig tendon excited by PIRL pulse.

In the present study, we limited the application of PIRL pulses to develop an ion sources for Imaging Mass Spectrometry, Laser Ablation Electrospray Ionization (LAESI). The system was compared directly to nanosecond ablation pulses of the same wavelength for which an interface has been built. The purpose of the study is to investigate the use of PIRL ablation for biological diagnosis given the tremendous advantages the technique has demonstrated for laser surgery. Previous studies have shown the collateral damage from PIRL surgery in various samples is confined to the first cell boundary, the minimal damage zone possible [11] [12] [13] [14].

4.2 PIR-LAESI on Aqueous Solution -- Limit of Detection of PIR-LAESI as an Ion Source

In order to characterize the sensitivity of PIR-LAESI as an ion source, experiments were conducted on aqueous solutions of Rerserpine (*m = 608.68 Da*) at different concentration and the limit of detection of the PIR-LAESI demonstrated. Conventional LAESI has been reported with the lowest detectable concentration of 750 nM [15] with the improvement down to 1 nM by utilizing plume collimator and laser beam coupled into etched fibers [16]. Here we performed a limit of detection experiment with a setup similar to the conventional LAESI but without plume collimation and fiber coupling of the beam. Experiments on other molecules such as Cytochrome C and lipids were also performed to demonstrate the ionization ability of PIR-LAESI and the results will be presented in the discussion section.

4.2.1 Experimental Setup

The geometry and principle of operation of PIR-LAESI has been discussed in Chapter 3 for solid samples such as tissue. For liquid samples, minor modification was made to ensure stable and reproducible results. The setup for liquid samples is shown in Figure 4.2.1. The liquid sample was delivered to the MS via a small cylindrical stainless steel sample holder connected to a large liquid reservoir (volume ~ 10 mL) constructed from Teflon. The cross section of the liquid reservoir was constructed to be oval in shape in order to ensure smooth flow without bubbles in the flow line. The height of the liquid level in the reservoir was adjustable via the attached vertical translational stage. Once smooth flow achieved, the position and shape of the meniscus of the liquid in the small sample holder was maintained by the flow during experiments with the continuous consumption of sample. In this case, the PIRL beam always hit the top of the meniscus with the same fluence from pulse to pulse to provide reproducible results. The geometry parameters were as follows: the vertical distance from the top of the meniscus to the MS entrance was $d_{s\text{-}ms} = 7\ mm$; the horizontal distance from the top of the meniscus to the MS entrance was $x_{s\text{-}ms} = 8\ mm$; the emitter of electrospray was aligned on the axis of the MS with its tip $x_{esi\text{-}ms} = 14\ mm$ away from the MS entrance. The voltage on the electrospray was 4.0 kV with a flow rate 90 μL/hour to maintain a stable spray. Voltages of 1.3 kV was applied on the stainless steel sample holder to help ions collected by the MS. The position of the meniscus was monitored by another camera from the side during experiments. Mixtures of deionized water (18 MΩ) and Methanol (MeOH, Sigma Aldrich, Oakville, ON, Canada) 1:1 were used as the solvent in the electrospray for all the experiments.

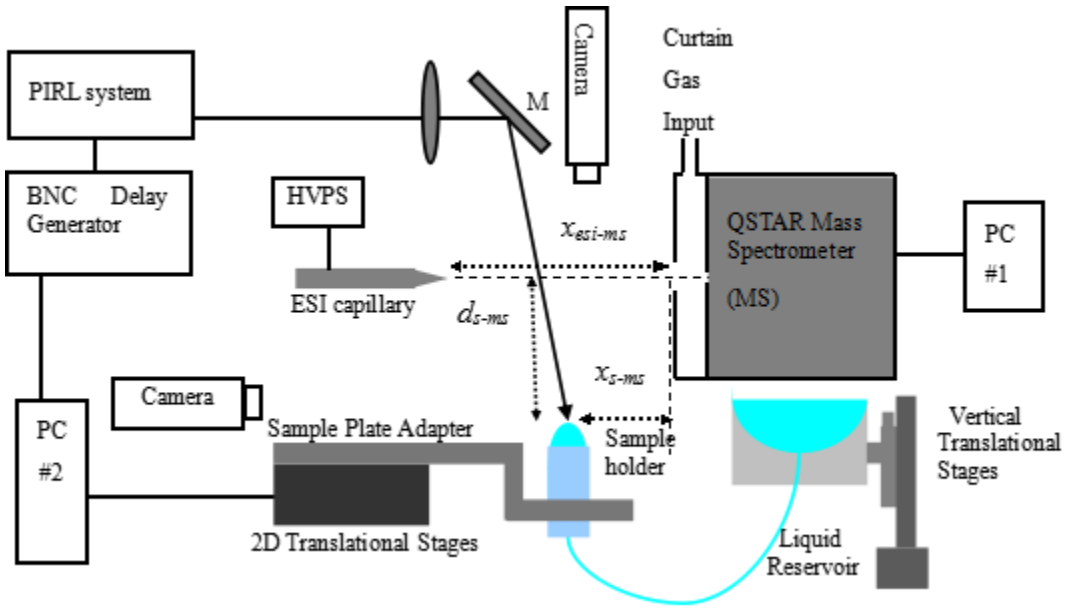

Figure 4.2.1 PIR-LAESI interface for limit of detection experiment.

4.2.2 Results and Discussion

PIR-LAESI was applied to water solutions of Reserpine, Cytochrome C and lipids (L-α-phosphatidylcholines (PC)) respectively. Reserpine and Cytochrome C were purchased from Sigma Aldrich (Oakville, ON, Canada) and L-α-phosphatidylcholines (PC) from Chicken eggs (average molecular weight ~ 770 Da) were purchased from Avanti Polar Lipids (Alabaster, AL, USA). Deionized water (18 MΩ), HPLC-MS grade, was used to make the aqueous solution. An amount of 10 µg of PC was diluted in chloroform and 100 µL of the resulting mixture was then dissolved in 900 µL (1:1) MeOH:H_2O solution with an approximate final concentration of 10 µM. The aqueous solution was loaded into the liquid reservoir with smooth flow to form a meniscus in the position shown in Figure 4.2.1. 1000 pulses of PIRL laser were sent at a repetition rate of 100 Hz. Some of the results shown here are presented in Ref. [17] which has been submitted to Analytical Chemistry and is now under processing.

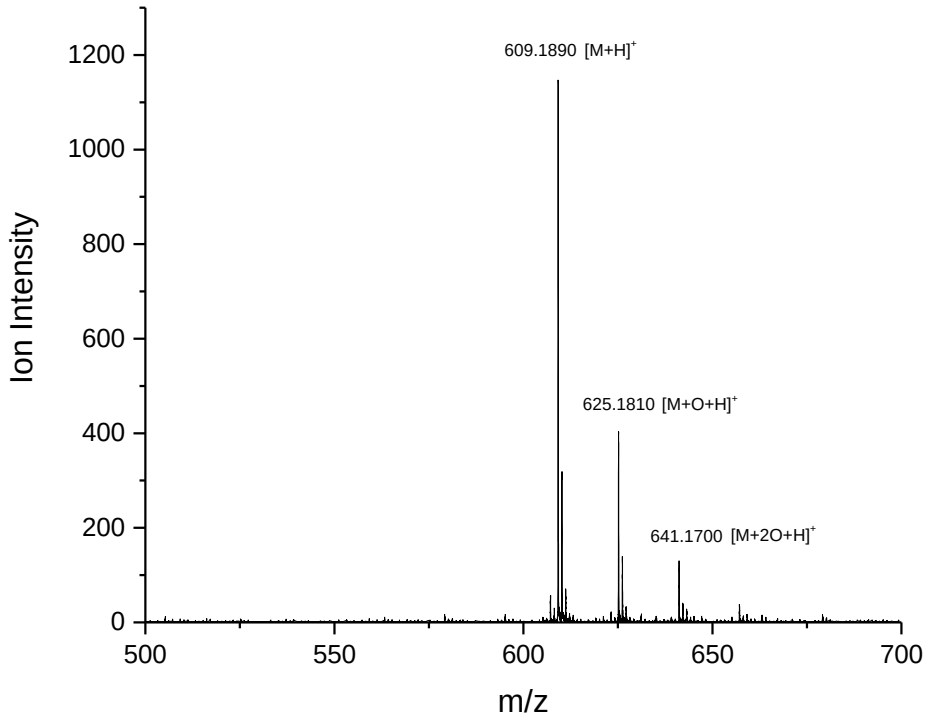

Figure 4.2.2 Spectrum of 1 μM Reserpine aqueous solution from PIR-LAESI ion source.

The spectrum of 1 μM reserpine aqueous solution is shown in Figure 4.2.2 with the protonated reserpine ion $[M+H]^+$ of mass to charge *m/z = 609.1890*, and other two peaks of *m/z = 625.1810* and *m/z = 641.1700* corresponding to single oxygen atom $[M+O+H]^+$ and double oxygen atoms $[M+2O+H]^+$ attached on the molecules. The theoretical *m/z* of protonated reserpine is 609.2807 Da, illustrating the results shown in Figure 4.2.2 has a mass deviation of 0.0917 Da.

The PIR-LAESI spectrum of 10 μM Cytochrome C water solution is shown in Figure 4.2.3. A typical ESI mass spectrum comprising of multiply charged ions $[M+nH]^{n+}$ is apparent. Compared to the spectrum from similar experiment done on the same protein using 100 ns long pulses at λ = 2940 nm [18] where two charge state distributions were observed, the spectrum in Figure 4.2.3 shows only one charge state distribution centered at $[M+14H]^{14+}$ and $[M+15H]^{15+}$ indicating only one conformation state of the protein was presented in the ablation process. No fragmentation was observed from the spectrum implying the proteins are kept intact during the ablation process.

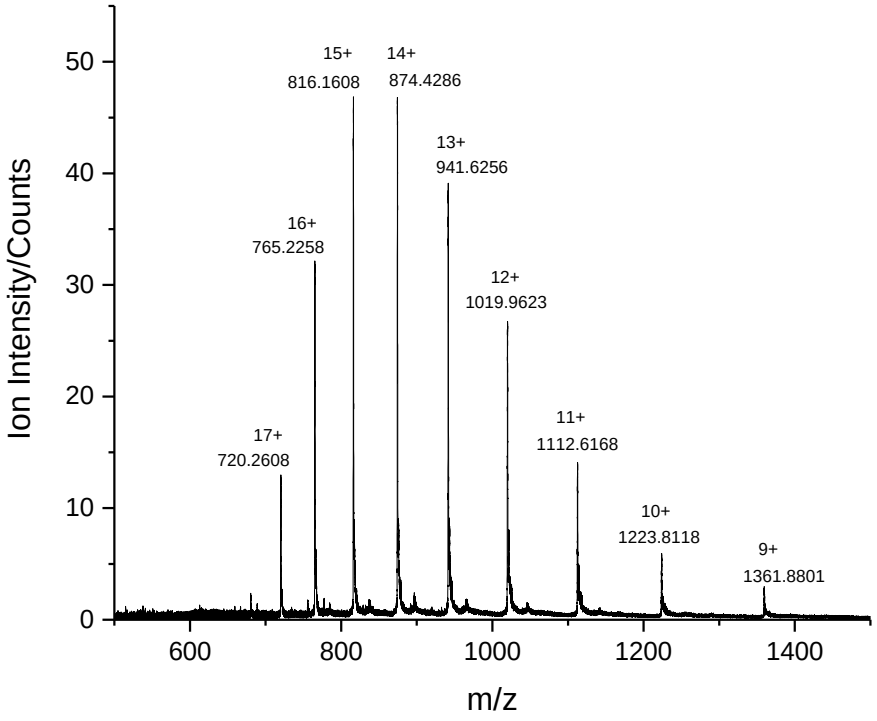

Figure 4.2.3 Spectrum of 10 μM Cytochrome C aqueous solution from PIR-LAESI ion source [17].

The spectrum of 10 μM of phospholipids extracted from chicken egg from PIR-LAESI is shown in Figure 4.2.4. The spectrum presents the dominant phospholipids of the egg yolk, sodiated, potassiated and protonated adducts of PC (34:2) and PC (34:1) as well as protonated PC (38:5) and PC (38:4) and sodiated PC (36:1). These phospholipids are in agreement with matrix assisted laser desorption ionization mass spectrometry (MALDI-MS) results of the phospholipids that constitute egg yolk [19].

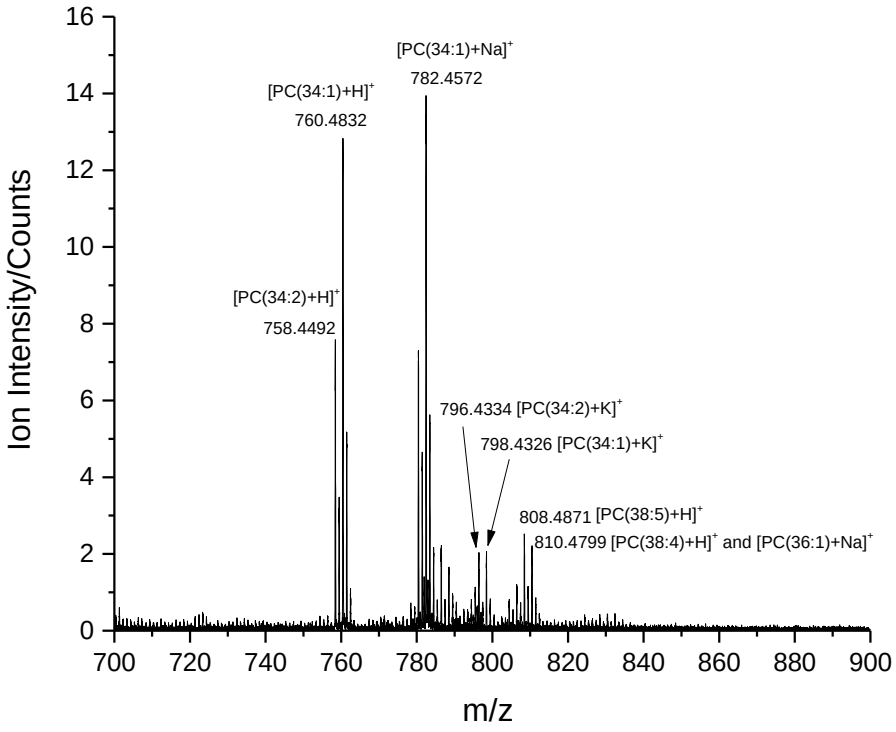

Figure 4.2.4 Spectrum of 10 μM phospholipids solution from PIR-LAESI ion source [17].

In order to obtain a figure of merit of the PIR-LAESI ion source, a series of aqueous solution of reserpine were prepared ranging from 10 pM to 50 μM, where 50 μM is the saturation concentration of reserpine at room temperature. The ion source was kept under identical condition for experiments from the lowest to highest concentrations. The spectrum was averaged over 1 s acquisition time for each solution corresponding to 100 PIRL pulses at a repetition rate of 100 Hz. The total ion counts of all *m/z* peaks were summed for data analysis, i.e. *m/z = 609*, *625* and *641*. The measured ion abundance *vs* analyte concentration curve was plotted on a log-log scale and is shown in Figure 4.2.5. The linear correlation with correlation coefficient of 0.9907 indicates the stable and reproducible performance of the ion source with the lowest detectable concentration of reserpine of 100 nM with the current MS system. This value is significantly lower than that obtained in similar experiments performed by Vertes. et al using a 7 ns pulse at $\lambda = 2.94\ \mu m$ which resulted in a limit of detection of 750 nM [15]. The spectrum from 100 nM solution is inserted into Figure 4.2.5, which demonstrates a signal to noise ratio S/N > 4.

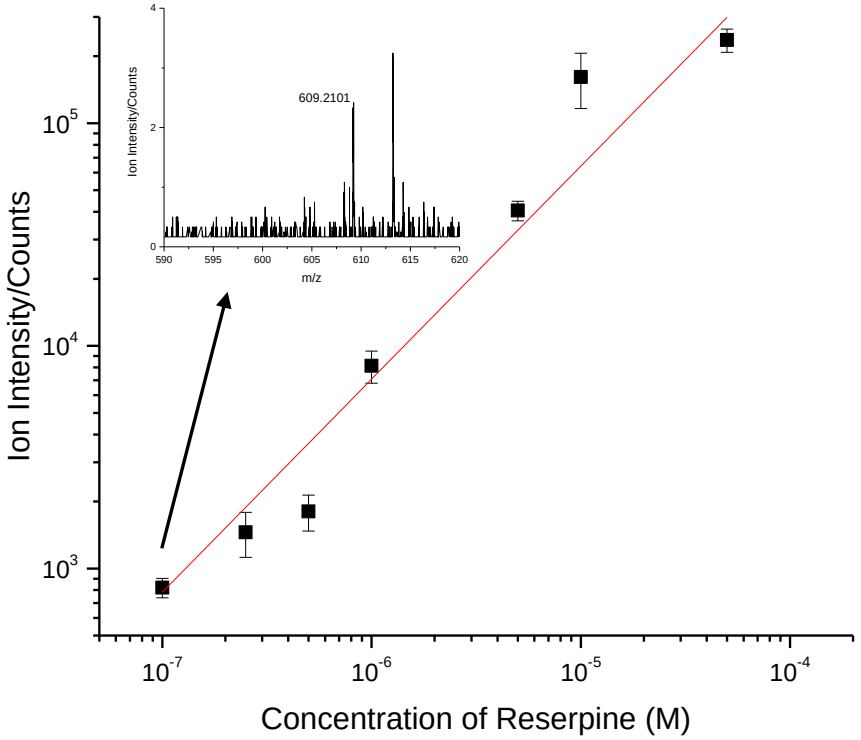

Figure 4.2.5 Limit of detection of PIR-LAESI using aqueous solution of Reserpine [17].

4.3 Characterization of PIR-LAESI as Imaging Mass Spectrometer Ion Source

Mass spectrometers have been used to map the molecular distribution in biological tissues over last decades. High spatial resolution has been reported for vacuum ion sources, such as secondary ion mass spectrometer (SIMS) with a spatial resolution < 1 μm [20] and MALDI < 5 μm [21]. As discussed in Chapter 2, the requirement of vacuum (SIMS) or complicated sample preparation process (MALDI) for these ion sources excludes them from their application as a surgical guidance instrument. Among ambient ion sources, LAESI and Desorption Electrospray Ionization (DESI) are the most widely studied. These techniques have been reported to possess a spatial resolution of 100 ~ 300 μm [22] [23], with DESI on ink printed paper and LAESI on a leaf sample. Recent studies also reported a spatial resolution of ~ 20 μm with DESI using nano-spray [24] and ~ 3 μm with LAESI by coupling the laser into a fiber of which one end was etched down to a few microns [25]. Given the influence of the physical properties of tissue on the laser-tissue interaction, the same technology may result in variations in spatial resolution for

different tissue types. In principle, the spatial resolution should be calibrated using standard calibration substrates. Unfortunately, to our knowledge, no such standard substrate exists for ambient soft ionization sources. Here we present the characterization of both the lateral and vertical spatial resolution of PIR-LAESI on a standard sample made from agarose gel with Rhodamine640 in the gel and the results are presented in Ref. [17].

4.3.1 Materials and Sample Preparation

The experiment was performed on the PIR-LAESI interface described in Chapter 3. Sucrose (*m = 342.30 Da*, Sigma Aldrich, Oakville, ON, Canada) and Rhodamine640 (Exciton, Rhodamine640 Percholrate, *m = 591.05 Da*) were chosen to be the indicator molecules due to their solubility in water and good thermal stability. 2% agarose gel containing the indicator molecules was used for characterization of the PIR-LAESI system. Agar powder (0.2 g) was mixed with 10 mL pure water (18 MΩ) and heated on a hot plate for 30 min for complete melting of agar powder to form a 2% agar water solution. Then 500 μL of 10 mM sucrose water solution (or 500 μL of 1 mM Rhodamine640 water solution) was mixed with the 4.5 mL of 2% agar solution within 3 minutes after being removed from the hot plate. The mixed solution was spread in petri dish at room temperature and stood for 30 minutes to form a 2% Agar gel with 1 mM of sucrose (100 μM of Rhodamine640) with a thickness of 400 μm. Optical image of the samples were taken by Nikon D3400 digital camera which was connected to the eyepiece of a microscope (Nikon SMZ-10) for comparison with the molecular map.

4.3.2 Lateral Resolution

The 1 mM sucrose 2% agarose gel and 100 μM Rhodamine640 2% agarose gel were cut into right triangles immediately after gel formation and placed onto a stainless steel sample plate with their hypotenuse parallel to each other and spaced by ~ 200 μm to minimize the diffusion of sucrose/Rhodamine640. The sample plate was cooled to 0^0 C to prevent the drying of the Agar gels during the experiment due to the high temperature and dry N_2 gas flow from the mass spectrometer. To avoid overlap of laser shots between pixels, the step size of the 2D translational stages was set to 200 μm. At each pixel, 100 PIRL laser pulses were sent to ablate the agarose gel at repetition rate of 100 Hz. The sucrose/Rhodamine640 in the ablated particulates were dissolved and ionized by the electrospray and then collected by the mass spectrometer. The time, t_{start}, on the acquisition software of the mass spectrometer was recorded. The (x,y) position

information as well as the timing of each pixel was recorded by the Labview program XYTissue_NIv2.vi discussed in Chapter 3. The ion peak of sucrose *m/z=365.1531* ($[M+Na]^+$) and Rhodamine640 *m/z=491.2933* $[M\text{-}ClO4]^+$ were observed as the dominant peaks for the respective samples. Figure 4.3.1 shows the two spectra respectively. The sucrose ion observed was formed via sodium ion attachment onto the sucrose molecule as is present in solution. The Rhodamine640 itself is a single charged ion in solution with the ClO_4^- counter ion detaching from the molecule. The optical image of the agarose gel following ablation and the molecular distribution of sucrose and Rhodamine640 are shown in Figure 4.3.2.

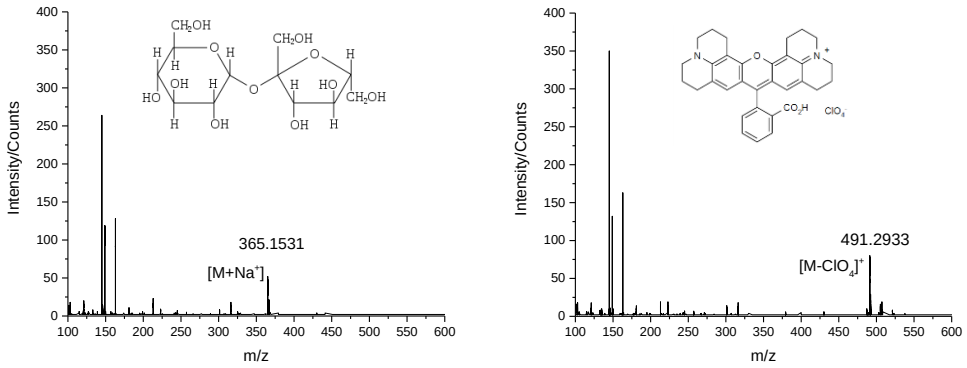

Figure 4.3.1 Mass Spectrum of Sucrose and Rhodamine640.

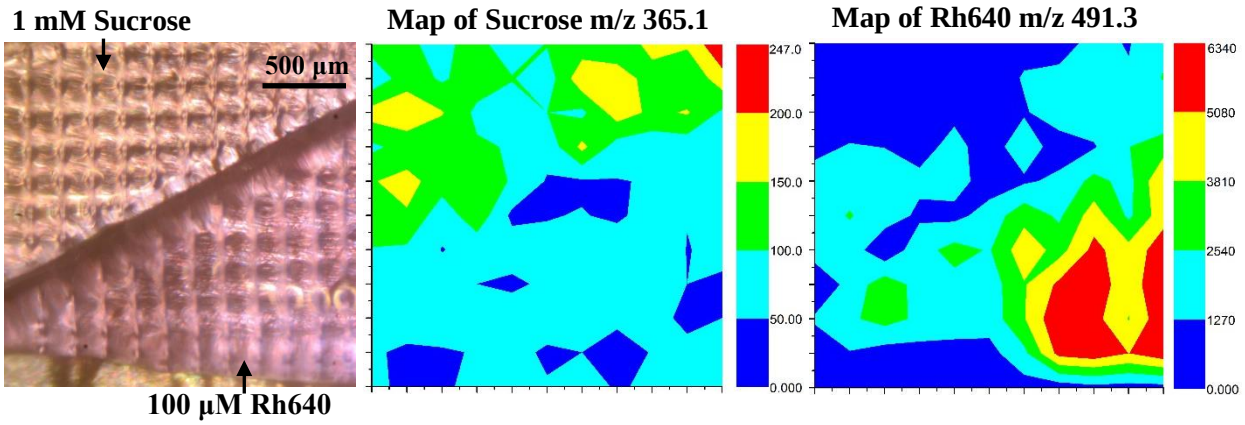

Figure 4.3.2 molecular map of 1 mM sucrose 2% agarose gel and 100 µM Rhodamine640 2% agarose gel.

In Figure 4.3.2, the left panel is the optical image of the agarose gel after ablation. The lateral resolution is limited by the spot size of the laser beam focused on the gel. With a focus diameter of 100 µm, the size of the well drilled by the laser was approximately 100 µm, therefore the lateral resolution for the ablation of agarose gel is approximately 100 µm.

The middle panel and the right panel in Figure 4.3.2 show the molecular map of sucrose (*m/z=365.1531*) and Rhodamine640 (*m/z=491.2933*) respectively. It can be clearly seen that the sucrose mostly distributed on the upper triangle area and the Rhodamine640 mostly distributed on the bottom triangle area. Both maps indicate a good match with the optical image. The red dashed lines confirm that the boundary of the sucrose/Rhodamine640 gel in the molecular map was approximately in the same position as the boundary in the optical image.

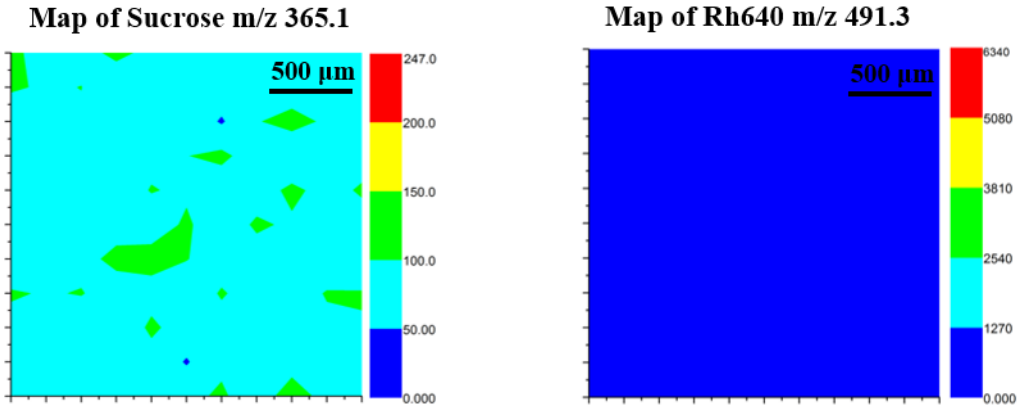

Figure 4.3.3 Examination of DESI contribution to the molecular map from PIR-LAESI.

Since the surface of agarose gel was only 4 mm below the emitter of electrospray, there was a chance that the signal could be produced via a DESI process. To test the contribution of DESI, another scan of the same sample under exactly the same experimental condition with the PIRL pulses blocked was performed. The molecular maps of sucrose and Rhodamine640 were constructed in exactly the same way as the case of PIR-LAESI with the same color scale for each molecule. The maps of sucrose and Rhodamine640 without PIRL pulse irradiation are shown in Figure 4.3.3. The uniform distribution of both maps confirms that the molecular maps shown in Figure 4.3.2 were purely from the PIR-LAESI process. No significant contribution from a DESI process was shown in the experiments.

4.3.3 Vertical Resolution

In order to characterize the vertical resolution of PIR-LAESI system, both mass spectrometers and bright field imaging experiment were performed. For the mass spectrometer experiments, double-sided tape was attached onto the sample plate and the mass spectrum of the polymer on the tape was recorded by PIR-LAESI, shown in Figure 4.3.4. A peak of *m/z=393.2548* was picked up as a reporter molecule of the double-sided tape. A thin layer of aluminum foil (<10 µm

thick) was firmly attached on top of the double-sided tape. PIRL laser pulses were sent to drill a hole through the aluminum foil until the *m/z = 393.2548* peak was observed in the mass spectrum. A 400 μm thick 2% agarose gel layer containing 100 μM Rhodamine640 was placed on top of aluminum foil. Diffusion of the polymer on the double-sided tape to the agarose gel was eliminated by the aluminum foil, but the hole still allowed the ablation plume from the double-sided tape to escape through to be ionized and collected by the ion source. Bursts of PIRL pulses were sent to the same *(x,y)* position as the hole on the aluminum foil until the signal from the double-sided tape appeared in the mass spectrum. Each bursts contained 10 pulses at repetition rate of 100 Hz with time intervals of 3 s between bursts. In this case the number of pulses needed to drill through the Agar layer can be obtained by monitoring the mass spectrum of the reporter molecule from the double-sided tape. The results are shown in Figure 4.3.5.

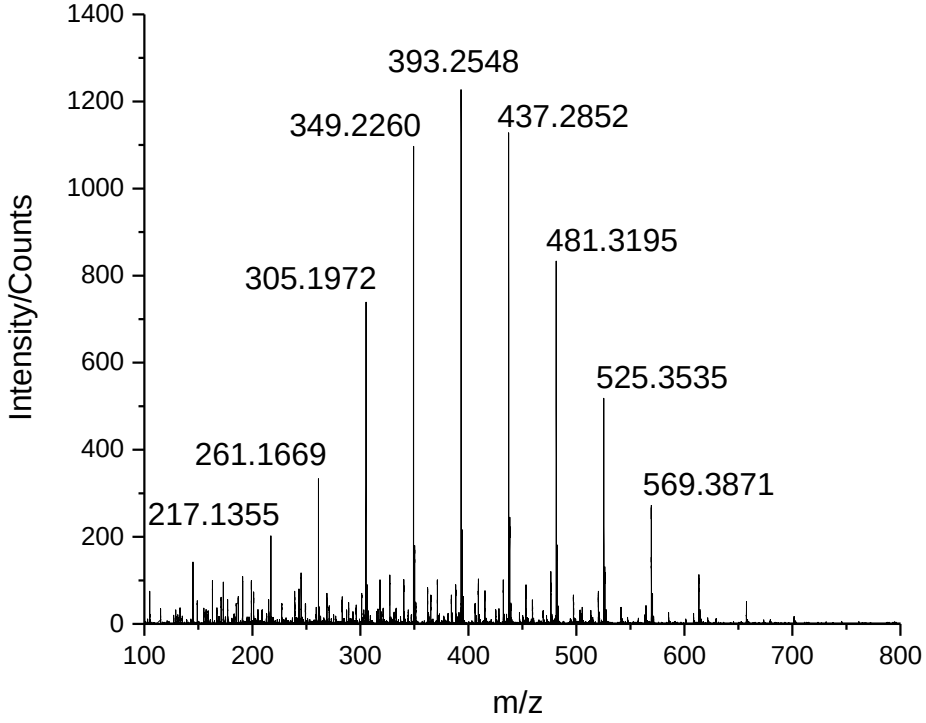

Figure 4.3.4 Spectrum of double-sided tape from PIR-LAESI.

In Figure 4.3.5, the peak from the Rhodamine640 ion (*m/z = 491.2933*) appeared immediately after the first burst was sent. The Rhodamine640 ions proceeded for the next two burst, but disappeared starting from the 4th burst. The signal from the double-sided tape (*m/z = 393.3*) appeared at the 10th burst, indicating that it took about 90 pulses to drill through the 400 μm layer of Agar. This indicates that each PIRL pulse removed ~ 4.5 μm of agarose gel.

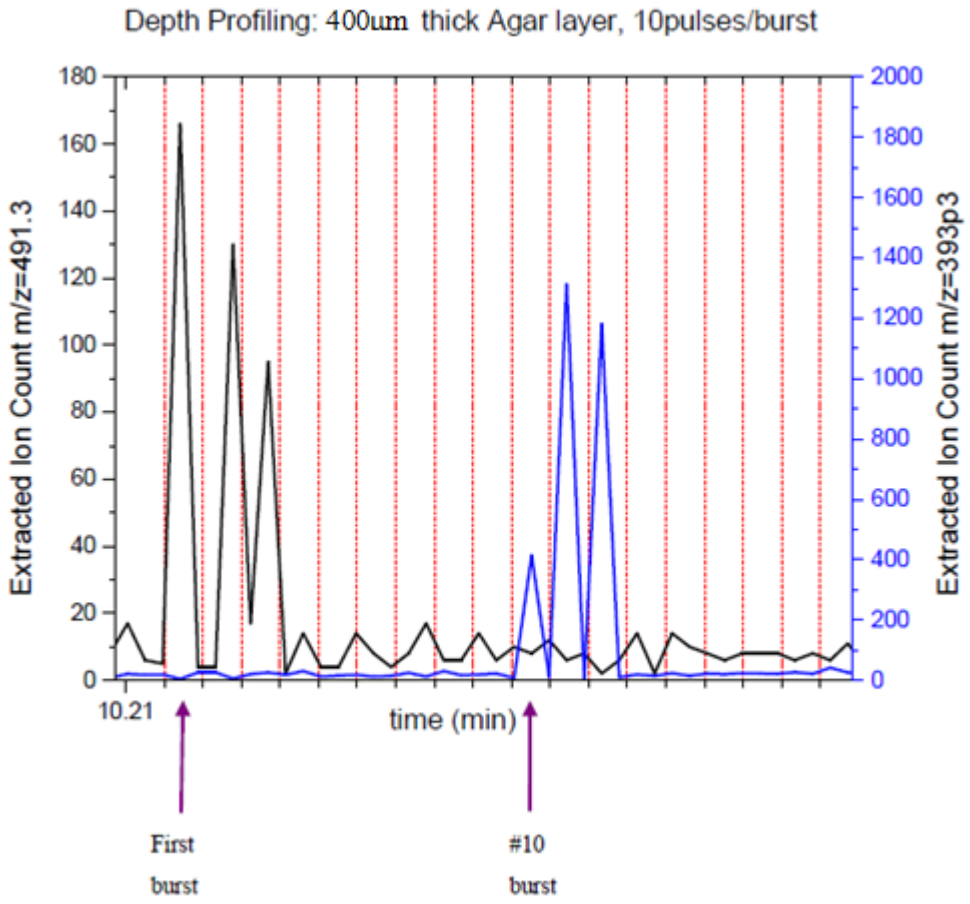

Figure 4.3.5 Vertical resolution of PIR-LAESI on 2% Agarose gel [17].

In order to further confirm the thickness of agarose layer removed by PIRL pulses, bright field images of the drilling through process was monitored on the same setup of dark field imaging microscope discussed in Section 4.1 by removing the central beam blocker and the direct illumination blocker in Figure 4.1.1. The illumination source was the same as used in dark field imaging since agarose gel is optical transparent medium for green beam. The agarose gel used in bright field image was exactly the same as used in mass spectrometer experiment. The PIRL laser also shoot exactly the same way as in mass spectrometer experiment, that is 10 pulses per burst at repetition rate of 100 Hz. Images of the agarose gel was taken after each burst, and the results are shown in Figure 4.3.6, with the center image of a 200 μm diameter pinhole taken under the same condition to show the dimension of the removal of agarose gel. The fluence irradiating on the agarose gel on the image set-up was approximately the same as in front of mass spectrometer. Figure 4.3.6 shows that it costs 90 pulses (9 bursts) to drill through a ~ 400

μm thick Agar layer, indicating each PIRL pulse can remove 4.5 μm agarose gel layer. The result is consistent with the mass spectrometer experiment results.

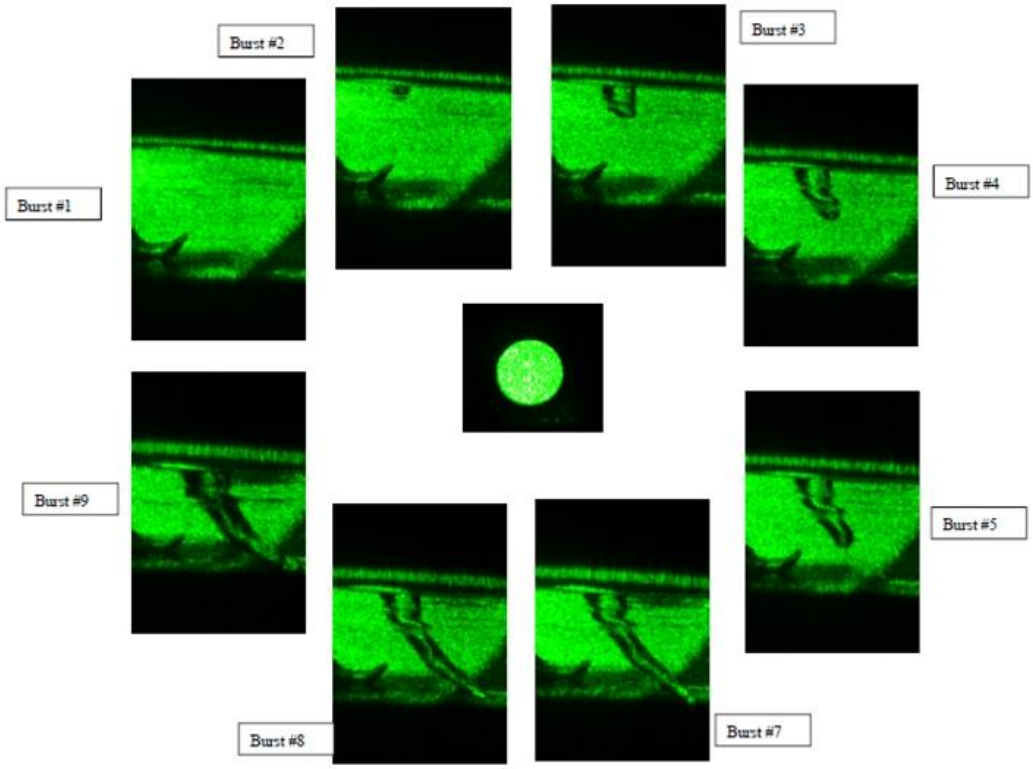

Figure 4.3.6 Dark Field Imaging of 2% agarose gel drilled through by burst of PIRL pulses. The middle picture is a 200 μm pinhole imaged under the same experimental condition [17].

The origin of the disappearance of the Rhodamine640 ion in later bursts in Figure 4.3.5 remains unclear. One possible reason could be that a channel was created inside the agarose gel as the PIRL pulse drilled deeper through. Compared to the first 3 bursts when the ablated plume was close to the surface and unrestricted, the plume from the later burst was required to escape the channel with a width of the laser spot size (< 200 μm) before it was captured by the electrospray. This explanation is not consistent with the detection of reporter molecule from the double-sided tape which was below the agarose gel with an aluminium foil spacer in between. It is possible that because the double-sided tape is a much stronger substrate for ablation and the quantity of the indicator molecule is very abundant that even a small portion of the plume escaped the narrow channel could be detected by the ion source. Further investigation is required to fully characterize the mechanism for plume production and propagation through a deep agar channel.

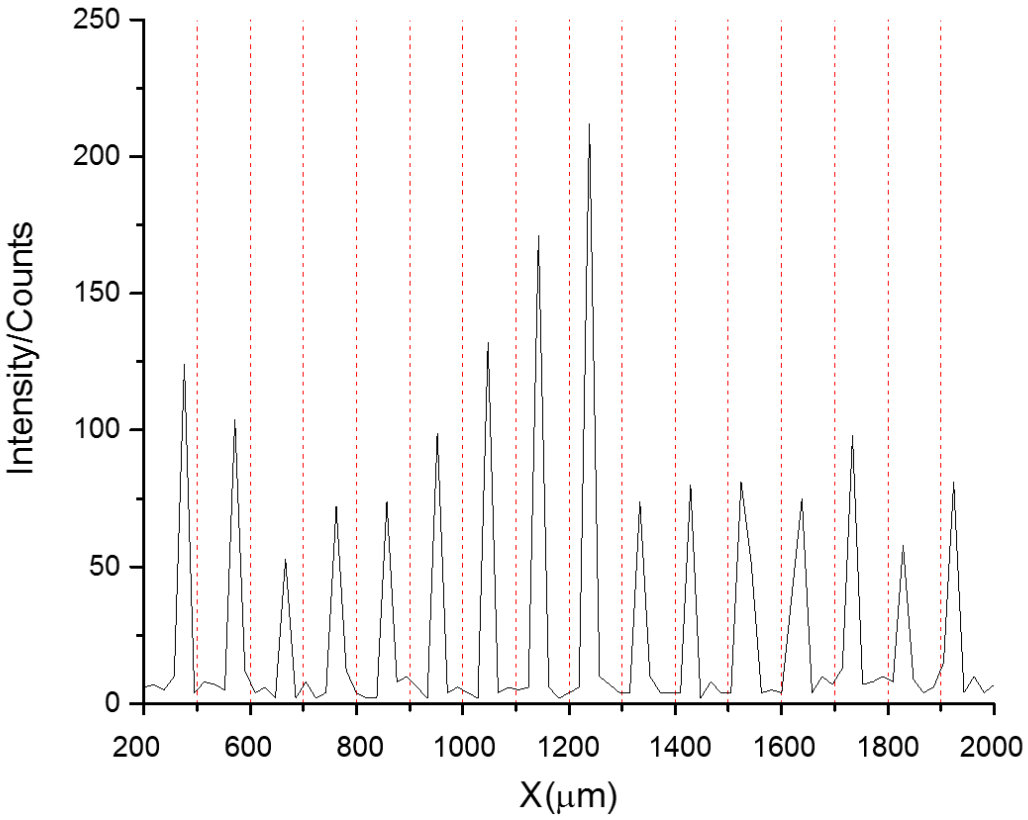

Figure 4.3.7 Ion counts of Rhodamine640 with 5 pulses per burst from PIR-LAESI.

The mechanism of the Rhodamine640 ion disappearance in later burst is unclear though it does not affect the application of the system to molecular tissue mapping. In order to construct a 3D molecular map of biological tissue, the scan will be performed layer by layer so series of 2D molecular map of each layer at different depth of the tissue are obtained. No channel will be created and the same experimental conditions are maintained at each layer. The vertical resolution of PIR-LAESI is defined by the thinnest agarose layer that PIRL pulses remove and can be reproducibly detected by the mass spectrometer interface. Since the thickness of the agarose layer removed by a single PIRL pulse was found to be 4.5 μm, in order to characterize the vertical resolution, we only need to know the minimum number of pulses that can provide a reproducible ion count at the mass spectrometer. The present design of the interface cannot reach stable single pulse detection. The number of pulses in each burst was increased and scans of the surface of the agarose gel was performed until the ion counts at different positions were reproducible. The ion counts of Rhodamine640 ions from PIRL burst containing 5 pulses from a 1D scan of the agarose gel surface is shown in Figure 4.3.7. The reproducibility is shown for Rhodamine640 ions in Figure 4.3.7 from burst to burst and spot to spot, indicating that with 5

pulses per burst, the ion source can detect abundant Rhodamine640 ions. The vertical resolution for the PIR-LAESI as an imaging mass spectrometer ion source is thus approximately 22.5 μm on 2% Agarose gel. The variation in the ion counts from burst to burst was due to the lack of synchronization between the burst and the acquisition in the MS. With a more efficient ion collection interface, it is very promising that the vertical resolution of PIR-LAESI can reach to 4 ~ 5 μm, the size of a single cell in biological tissue.

In conclusion, the PIR-LAESI experiments on 2% Agar gel reveals the ion source as a very promising tool to be applied to native biological soft tissues for molecular mapping. The present interface demonstrated a horizontal spatial resolution of ~ 100 μm and vertical resolution of ~ 20 μm on 2% agarose gel. With the concentration of Rhodamine640 of 100 μmole/L, this volume contains 15.7 fmol of Rhodamine640 molecules, proving the sensitivity of PIR-LAESI ion source is at least in femtomole range. These values may vary for different tissues given the tissue dependence of the interaction mechanism of PIRL pulses. With improvements to the design of the instrument and a tighter focused laser beam, it is quite possible to reach a horizontal spatial resolution of ~ 10 μm and vertical spatial resolution of ~ 4 μm which is on the order of the size of a single cell in biological system.

References of Chapter 4

[1] L. R. Solon, R. Aronson, and G. Gould, “Physiological implications of laser beams,” Science, vol. 134, no. 3489, pp. 1506–1508, Nov. 1961.

[2] M. M. Zaret, G. M. Breinin, H. Schmidt, H. Ripps, I. M. Siegel, and L. R. Solon, “Ocular lesions produced by an optical maser (laser),” Science, vol. 134, no. 3489, pp. 1525–1526, Nov. 1961.

[3] K. Nahen and A. Vogel, “Plume dynamics and shielding by the ablation plume during Er:YAG laser ablation,” J. Biomed. Opt., vol. 7, no. 2, pp. 165–178, Apr. 2002.

[4] I. Apitz and A. Vogel, “Material ejection in nanosecond Er:YAG laser ablation of water, liver, and skin,” Appl. Phys. A, vol. 81, no. 2, pp. 329–338, Mar. 2005.

[5] K. Franjic and R. J. D. Miller, “Vibrationally excited ultrafast thermodynamic phase transitions at the water/air interface,” Phys. Chem. Chem. Phys., vol. 12, no. 20, p. 5225, 2010.

[6] K. Franjic, “STUDIES OF LASER ABLATION OF LIQUID WATER UNDER CONDITIONS OF IMPULSIVE HEAT DEPOSITION THROUGH VIBRATIONAL EXCITATIONS (IHDVE),” 2010.

[7] A. Vogel, I. Apitz, S. Freidank, and R. Dijkink, “Sensitive high-resolution white-light Schlieren technique with a large dynamic range for the investigation of ablation dynamics,” Opt. Lett., vol. 31, no. 12, p. 1812, 2006.

[8] D. Eisenberg and W. Kauzmann, The Structure and Properties of Water. Oxford University Press, 2005.

[9] A. Vogel and V. Venugopalan, “Mechanisms of Pulsed Laser Ablation of Biological Tissues,” Chem. Rev., vol. 103, no. 2, pp. 577–644, Feb. 2003.

[10] A. Zarrine-Afsar, C. Mueller, F. O. Talbot, and R. J. D. Miller, “Self-Localizing Stabilized Mega-Pixel Picoliter Arrays with Size-Exclusion Sorting Capabilities,” Anal. Chem., vol. 83, no. 3, pp. 767–773, Feb. 2011.

[11] S. Amini-Nik, D. Kraemer, M. L. Cowan, K. Gunaratne, P. Nadesan, B. A. Alman, and R. J. D. Miller, “Ultrafast Mid-IR Laser Scalpel: Protein Signals of the Fundamental Limits to Minimally Invasive Surgery,” PLoS ONE, vol. 5, no. 9, p. e13053, Sep. 2010.

[12] M. Hess, M. D. Hildebrandt, F. Müller, S. Kruber, P. Kroetz, U. Schumacher, R. Reimer, M. Kammal, K. Püschel, W. Wöllmer, and D. Miller, “Picosecond infrared laser (PIRL): an ideal phonomicrosurgical laser?,” Eur. Arch. Otorhinolaryngol., vol. 270, no. 11, pp. 2927–2937, Nov. 2013.

[13] N. Jowett, W. Wöllmer, A. M. Mlynarek, P. Wiseman, B. Segal, K. Franjic, P. Krötz, A. Böttcher, R. Knecht, and R. J. D. Miller, “Heat Generation During Ablation of Porcine Skin With Erbium:YAG Laser vs a Novel Picosecond Infrared Laser,” JAMA Otolaryngol. Neck Surg., vol. 139, no. 8, p. 828, Aug. 2013.

[14] A. Böttcher, T. S. Clauditz, R. Knecht, S. Kucher, W. Wöllmer, W. Wilczak, P. Krötz, N. Jowett, C. V. Dalchow, A. Münscher, and R. J. D. Miller, “A novel tool in laryngeal

surgery: preliminary results of the picosecond infrared laser," The Laryngoscope, vol. 123, no. 11, pp. 2770–2775, Nov. 2013.

[15] P. Nemes and A. Vertes, "Laser Ablation Electrospray Ionization for Atmospheric Pressure, in Vivo, and Imaging Mass Spectrometry," Anal. Chem., vol. 79, no. 21, pp. 8098–8106, Nov. 2007.

[16] J. A. Stolee and A. Vertes, "Toward Single-Cell Analysis by Plume Collimation in Laser Ablation Electrospray Ionization Mass Spectrometry," Anal. Chem., vol. 85, no. 7, pp. 3592–3598, Apr. 2013.

[17] J. Zou, F. Talbot, A. Tata, L. Ermini, K. Franjic, M. Ventura, J. Zheng, H. Ginsberg, M. Post, D. R. Ifa, D. Jaffray, R. J. D. Miller and A. Zarrine-Afsar, "Ambient Mass Spectrometry Imaging with Picosecond InfraRed Laser Ablation ElectroSpray Ionization (PIR-LAESI)", Anal. Chem. , submitted July 2015, under processing.

[18] Y. H. Rezenom, J. Dong, and K. K. Murray, "Infrared laser-assisted desorption electrospray ionization mass spectrometry," The Analyst, vol. 133, no. 2, pp. 226–232, Feb. 2008.

[19] B. Fuchs, "A direct and simple method of coupling matrix-assisted laser desorption and ionization time-of-flight mass spectrometry (MALDI-TOF MS) to thin-layer chromatography (TLC) for the analysis of phospholipids from egg yolk," Anal. Bioanal. Chem., vol. 389, no. 3, pp. 827–834, Oct. 2007.

[20] P. J. Todd, T. G. Schaaff, P. Chaurand, and R. M. Caprioli, "Organic ion imaging of biological tissue with secondary ion mass spectrometry and matrix-assisted laser desorption/ionization," J. Mass Spectrom., vol. 36, no. 4, pp. 355–369, Apr. 2001.

[21] S. Guenther, A. Rompp, W. Kummer and B. Spengler, "AP-MALDI imaging of neuropeptides in mouse pituitary gland with 5 μm spatial resolution and high mass accuracy," Int. J. Mass Spectrom., vol. 305, no.2-3, pp. 228-237, Aug. 2011.

[22] D. Ifa, L. Gumaelius, L. Eberlin, N. Manicke, and R. Cooks, "Forensic analysis of inks by imaging desorption electrospray ionization (DESI) mass spectrometry," ANALYST, vol. 132, no. 5, pp. 461–467, 2007.

[23] P. Nemes, A. A. Barton, Y. Li, and A. Vertes, "Ambient Molecular Imaging and Depth Profiling of Live Tissue by Infrared Laser Ablation Electrospray Ionization Mass Spectrometry," Anal. Chem., vol. 80, no. 12, pp. 4575–4582, Jun. 2008.

[24] J. Laskin, B. S. Heath, P. J. Roach, L. Cazares, and O. J. Semmes, "Tissue Imaging Using Nanospray Desorption Electrospray Ionization Mass Spectrometry," Anal. Chem., vol. 84, no. 1, pp. 141–148, Jan. 2012.

[25] B. Shrestha, J. M. Patt, and A. Vertes, "In Situ Cell-by-Cell Imaging and Analysis of Small Cell Populations by Mass Spectrometry," Anal. Chem., vol. 83, no. 8, pp. 2947–2955, Apr. 2011.

Chapter 5
Application of PIR-LAESI for Molecular Mapping of Biological Tissue

The successful application of PIR-LAESI to 2% agarose gel motivates the development of this ion source for the molecular mapping of real biological system. In the development of the conventional LAESI-MS using nanosecond mid infrared pulses ($\lambda = 2.94\ \mu m$), the application was first extended to plant tissues [1][2][3][4][5][6] and then to animal tissues [7][8][9][10]. PIR-LAESI development has followed the same route as conventional LAESI-MS. In this Chapter, the molecular map of Zebra plant (Aphelandra squarrosa) from PIR-LAESI is first shown and a comparison of PIR-LAESI with conventional LAESI-MS on the same plant leaf will be discussed. The ability of PIR-LAESI to detect molecules directly from animal tissue is then shown on chicken kidney and salmon fish. Finally, PIR-LAESI images of mouse kidneys intravenously injected with Gadoteridol, an exogenous Magnetic Resonance Contrast agent, is presented. Parallel Mass Spectrometry Imaging (MSI) using Desorption ElectroSpray Ionization (DESI) and Matrix Assisted Laser Desorption/Ionization (MALDI) are also shown for direct comparison to PIR-LAESI images of the exogenous agent. Most of the results are presented in Ref. [11].

5.1 PIR-LAESI Images of the Molecular Distributions in Zebra Plant Leaf

Given that conventional LAESI-MS has shown success in molecular imaging of Zebra plant leaf, the ability of PIR-LAESI to image the molecular distribution on biological tissue was first proven on the same plant. Zebra plant was purchased from the local florist and stored in a shaded area in the lab. 200 mL of tap water was applied every day to keep it fresh. In order to compare with conventional LAESI-MS, the repetition rate of PIRL laser was set to 10 Hz, the same as the OPO used for the nanosecond IR pulses. Both the fluence from the PIRL beam and from the nanosecond OPO beam was set to approximately 1.5 J/cm^2 in front of the MS. At each pixel, 20 pulses were sent to ablate the tissue for MS analysis and a delay time of 4 s at each pixel was set after the pulses to reduce the carry-over effect from pixel to pixel. The total dwell time at each

pixel was set to 6 s. The geometry between the surface of the leaf, the emitter of the electrospray, the laser focus and the MS entrance was the same as in described in Chapter 3.

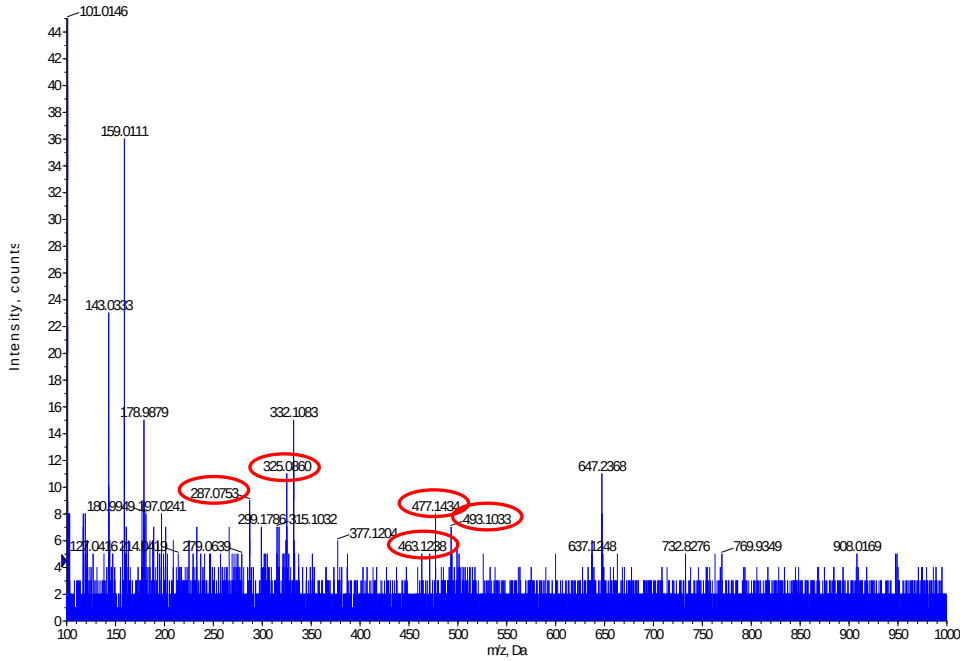

Figure 5.1.1 Mass spectrum of Zebra plant leaf from PIR-LAESI ion source.

The spectrum collected from the leaf using PIR-LAESI is shown in Figure 5.1.1. The peaks in the spectrum whose extracted ion chromatogram (XIC) showed a laser correlated pulsed pattern were produced with PIR-LAESI. The XIC of *m/z = 493.1033* is shown as Figure 5.1.2, presenting a pulsed pattern related to PIRL lasers. A few of these peaks are circled red in Figure 5.1.1. The XIC of these peaks were exported for the construction of the molecular map. Figure 5.1.3 shows a few of the molecules used for the map with the optical image of the leaf after the PIR-LAESI experiment [11]. As can be seen in Figure 5.1.3， molecules with a mass to charge ratio of *m/z = 463.1146* (kaempferol glucuronide), *m/z = 477.1477* (methoxykaempferol glucuronide), *m/z = 493.1033* (methoxyluteolin glucuronide) and *m/z = 639.0899* (kaempferol diglucoronide) were mostly concentrated in the yellow part of the leaf and matched the optical image very well. Sugar signal (glucose) was also seen but distributed evenly as shown in the bottom right panel in Figure 5.1.3. These molecules are also reported in conventional LAESI-MS experiments [5], listed in Table 5.1, whereas the highlighted molecules only locate in the yellow part of the leaf and the un-highlighted molecules distribute everywhere. The molecules in Table 1 were taken from reference [5] with copyright permission.

.

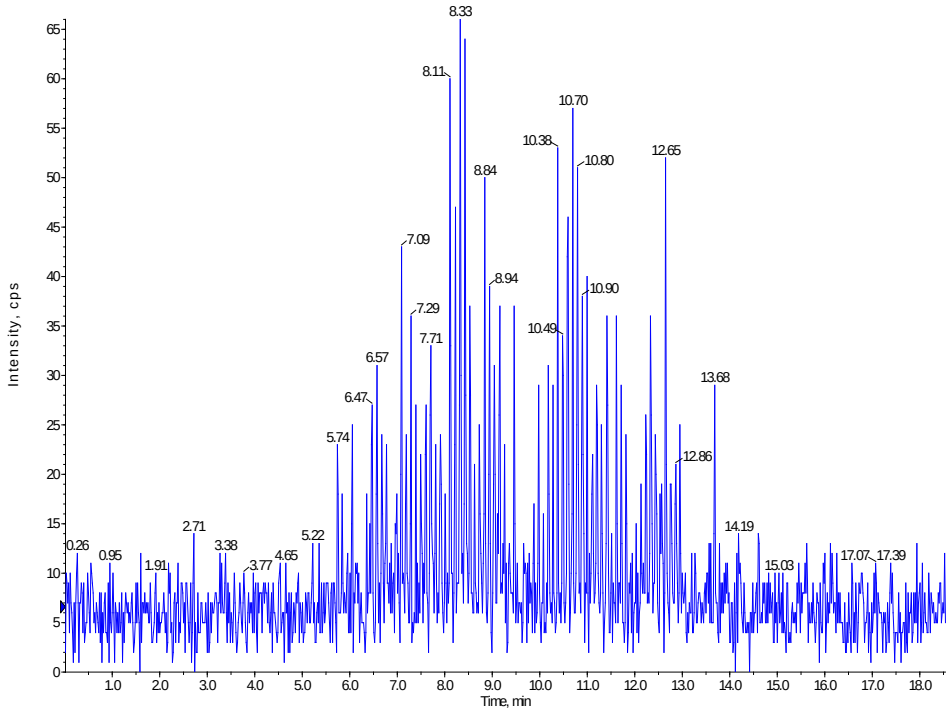

Figure 5.1.2 Extracted ion chromatogram of *m/z=493.1033*.

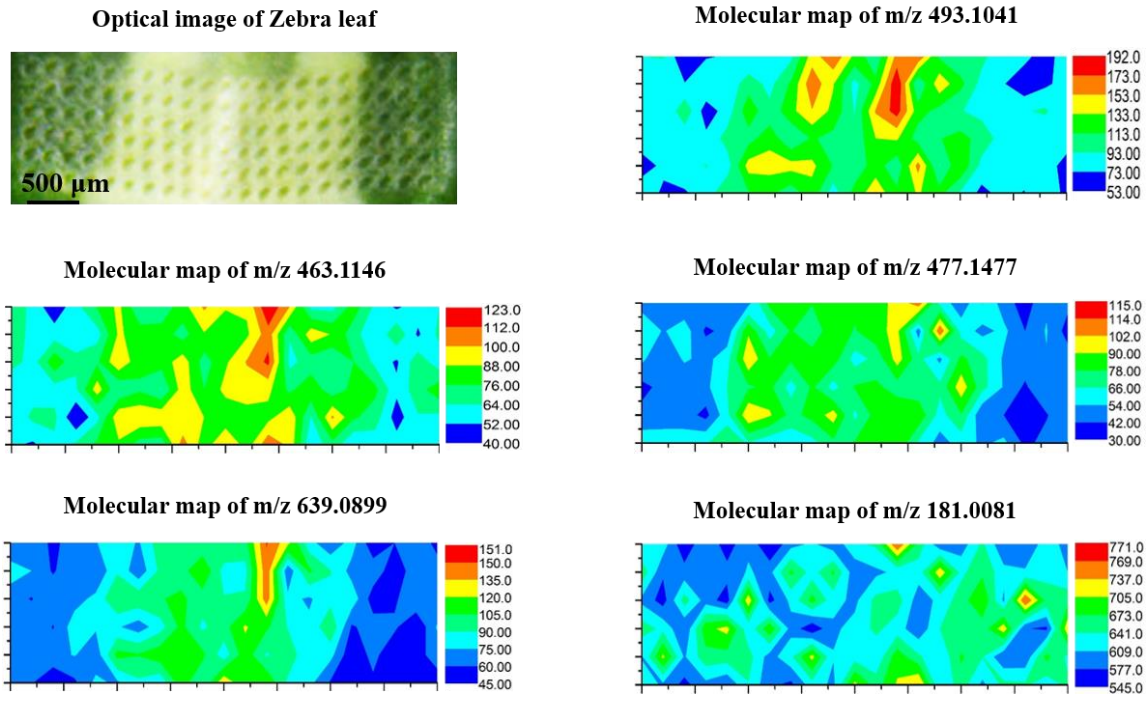

Figure.5.1.3 Molecular map of Zebra plant leaf from PIR-LAESI [11].

Table 5.1 Molecules in Zebra Plant leaf detected by both PIR-LAESI and nanosecond LAESI

Name	Formula	Monoisotopic *m/z*	Measured *m/z*	*Δm* (mDa)
succinate	C4H6O4	119.0339(H)	119.0216	-12.3
allantoin	C4H6N4O3	159.0513(H)	159.0077	-43.6
glucose	C6H12O6	181.0707(H) 203.0526(Na)	181.0707 203.0759	-62.6 23.3
kaempferol, luteolin	C15H10O6	287.0550(H)	287.0758	20.8
methoxykaempferol, methoxyluteolin, methylquercetin, petunidin	C16H12O7	317.0656(H) 317.0656(+)	317.1002	34.6
Methoxy-hydroxyphenyl glucoside	C13H18O8	325.0894(Na)	325.0880	-1.4
sucrose	C12H22O11	365.1054(Na)	365.1031	-2.3
kaempferol glucuronide, luteolin glucoronide	C21H18O12	463.0871(H)	463.1146	27.5
methylkaempferol glucoronide	C22H21O12	477.1028(+)	477.1477	44.9
acetylkaempferol glucoside, acetylluteolin glucoside	C23H22O12	491.1184(H)	491.1350	16.6
methoxykaempferol glucoronide	C22H20O13	493.0982(H)	493.1041	5.9
acacetin diglucoronide, kaempferol(acetyl-coumarylglucoside)	C32H28O14	637.1552(H)	637.1437	-11.5
kaempferol diglucoronide, luteolin diglucoronide	C27H26O18	639.1198(H)	639.0899	-29.9
luteolin methyl ether glucoronosyl glucoronide	C28H28O18	653.1348(H)	653.1505	15.7

*The mass accuracy, *Δm*, is the difference between the measured and calculated monoisotopic masses.

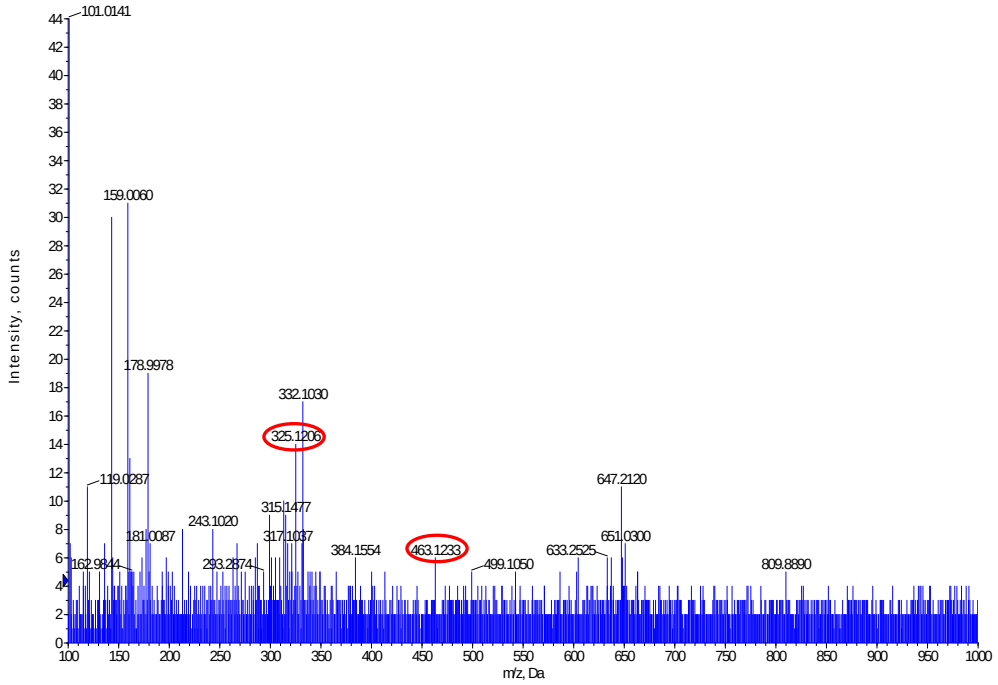

Figure 5.1.4 Mass spectrum of Zebra plant leaf from conventional LAESI ion source.

It is not accurate to compare PIR-LAESI with conventional LAESI by comparing the results presented here directly with the reported results in the literature [5] because the detection of the ions is not only dependent on the ion source but also on the mass spectrometer and its associated settings. A fairer comparison is to test the two ion sources on the same mass spectrometer and on the same sample. For this purpose, experiments on the same piece of leaf was performed using nanosecond IR pulses from the OPO under the optimized geometry for the laser pulses with the geometry parameter similar to PIR-LAESI interface. The spectrum of Zebra plant leaf from conventional LAESI-MS is shown in Figure 5.1.4 with some peaks from the leaf circled red. Compared with the spectrum from PIR-LAESI (Figure 5.1.1), there are less peaks visible in the conventional LAESI spectrum, especially in the higher mass range ($m/z > 400$). The XIC of $m/z = 493.1041$ is shown in Figure 5.1.5. Compared with the XIC of the same molecule but from PIR-LAESI in Figure 5.1.2, the ion intensity is on the same level, namely about 65 in PIR-LAESI and 70 in conventional LAESI.

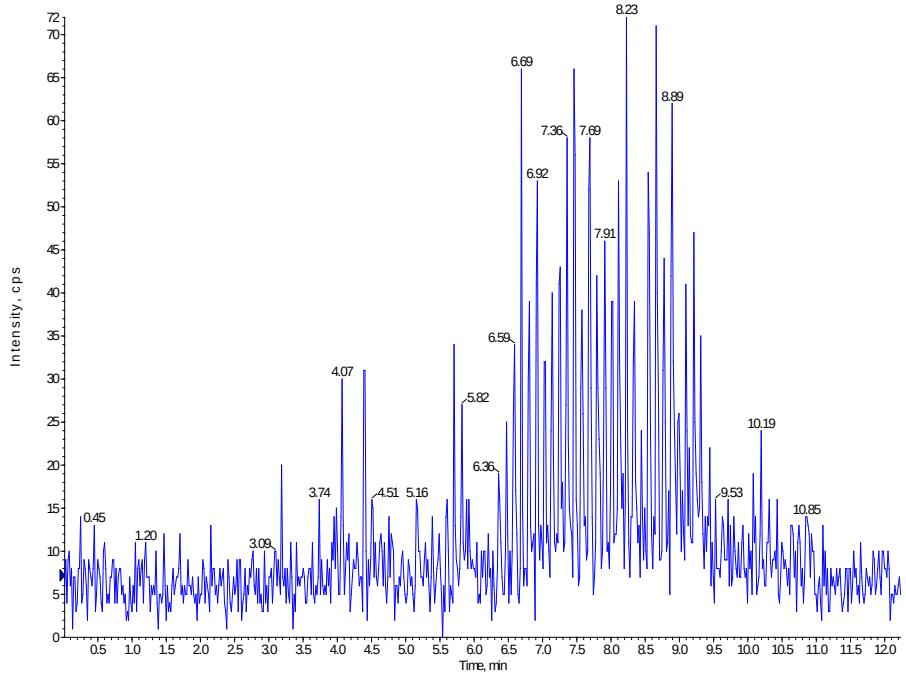

Figure 5.1.5 Extracted ion chromatogram of *m/z = 493.1041* from conventional LAESI ion source.

The molecular map of methoxykaempferol glucoronide (*m/z = 493.1041*) from both conventional LAESI as well as PIR-LAESI is shown in Figure 5.1.6 with the optical image of the leaf after the experiment [11]. Both maps match the optical image with the molecule only located in the yellow section of the leaf. There is no loss of image quality or accuracy in the map from PIR-LAESI as compared to the map from the conventional LAESI ion source.

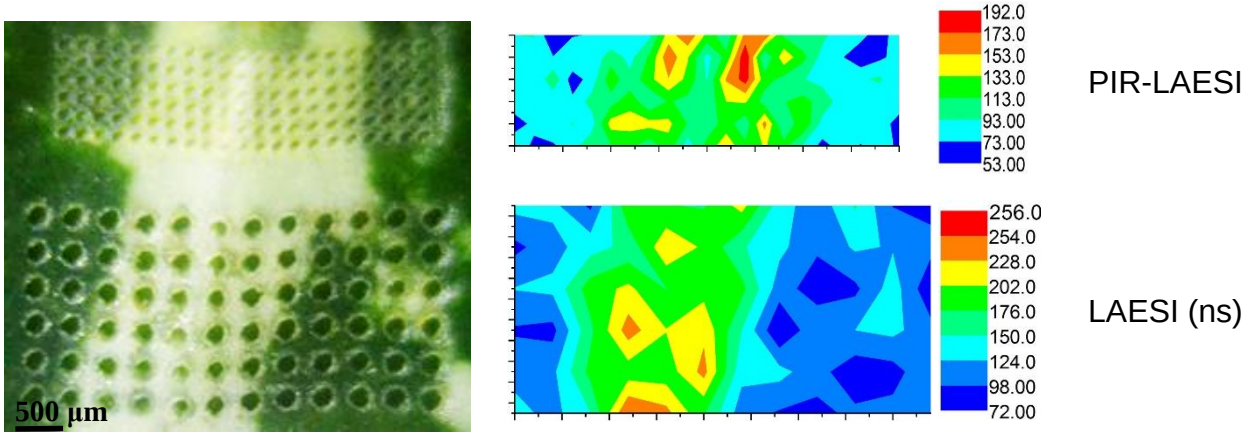

Figure 5.1.6 Molecular map of methoxykaempferol glucuronide (m/z = 493.1041) from Zebra plant leaf using both PIR-LAESI and conventional LAESI ion source. The picture in the right is the optical image of the leaf taken after the experiment [11].

Figure 5.1.6 clearly illustrates the improved spatial resolution in PIR-LAESI compared with conventional LAESI in the optical image. The laser focus in PIR-LAESI was 100 μm and the step size was 200 μm, whereas the spot size in conventional LAESI was 300 μm and the step size was 400 μm. Thus the spatial resolution of PIR-LAESI on Zebra plant leaf in the present design is 150 ~ 200 μm whereas in conventional LAESI it is 300 ~ 400 μm. The smaller spot size in PIR-LAESI led to a smaller ablated volume and thus less molecules originating from each pixel compared to conventional LAESI. However, the ion intensity from PIR-LAESI is on the same level as in conventional LAESI, Figure 5.1.2 and Figure 5.1.5, implying a more efficient desorption/ionization process in PIR-LAESI.

Due to the limited space in front of our mass spectrometer, we cannot focus the PIRL beam tighter by using a lens with a shorter focal length. However, with the beam quality of the PIRL beam M^2 ~ 1, it is possible to focus the beam down to 10 μm, the size of a single cell. The ion source is therefore very promising to be capable of creating a molecular map with a resolution comparable to a single cell. This feature is very important in surgeries using PIRL as a laser scalpel when combined with a mass spectrometer vivo to provide the molecular feedback to minimize damage to a patient's health tissue.

5.2 PIR-LAESI on Raw Animal Tissues: Chicken Kidney

The success of PIR-LAESI applied to Zebra leaf motivates us to make a further step to its application on animal tissues. Chicken kidney was first tested with the ion source due to availability. The sample was kept frozen at -20^o C until use. Slice of ~400 μm thick tissue was cut by a blade and placed on top of the stainless steel sample plate. The temperature of the sample plate was kept at -2^o C during the experiment to prevent drying of the samples. The geometry of the interface and the laser parameters were the same as described in Chapter 3. 100 PIRL pulses were sent at repetition rate of 100 Hz with a 5 s delay following the laser pulses at each spot.

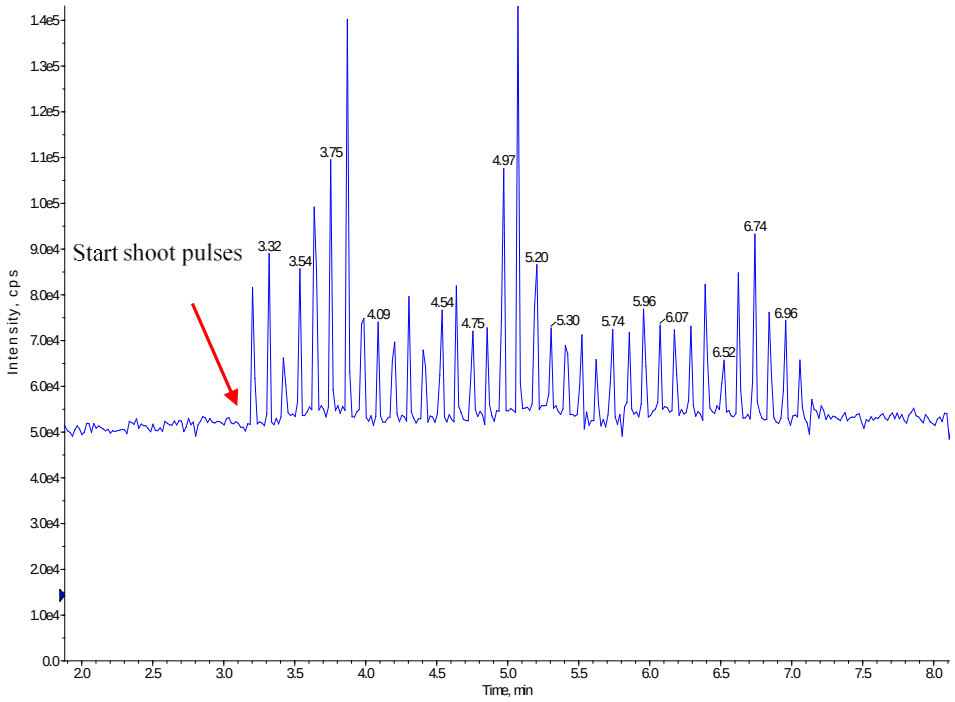

Figure 5.2.1 Total ion chromatogram of chicken kidney from PIR-LAESI ion source.

The total ion chromatogram (TIC) of chicken kidney is shown in Figure 5.2.1. The pulsed pattern of TIC indicates ions from the chicken kidney detected by the PIR-LAESI ion source. The mass spectra within the pulsed pattern range in Figure 5.2.1 was extracted and background spectrum was subtracted. The result is shown in Figure 5.2.2 with ions of proteins found in chicken kidney present. The proteins were multiply charged and centered at charge state of 18+ (m/z 961.7304) and 19+ (m/z 911.1670). From the charge distribution, the calculated molar mass of this protein is 17293 Da which is myoglobin, the main pigment protein in animal meat [12][13][14]. Further confirmation was done by a database search using “chicken myoglobin” as key words in SwissProt protein database (www.uniprot.org/uniprot/) yielded the unique entry P02197. Calculation of the average molecular weight of the coding protein sequence [2-154] using a web available tool (web.expasy.org/compute_pi/) yielded a mass of 17291 Da, which is within 2 Da of the experimental mass.

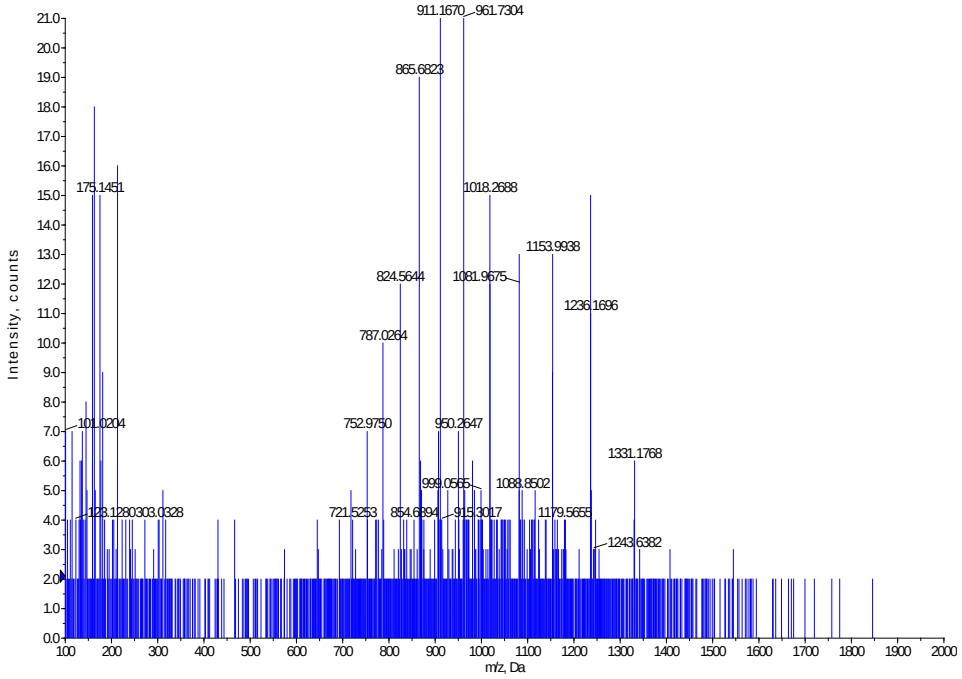

Figure 5.2.2 Mass spectrum of chicken kidney from PIR-LAESI ion source.

5.3 PIR-LAESI Images of a Magnetic Resonance Contrast Agent in Mice Kidney

The success in detecting proteins directly from chicken kidney encouraged further extension of PIR-LAESI for molecular mapping of animal tissues. For this purpose, PIR-LAESI was used to image the distribution of Gadoteridol (monoisotpic mass 559.13Da), an exogenous Magnetic Resonance Contrast agent, intravenously injected inside mouse kidneys. The structure and the isotopic distribution of neutral Gadoteridol molecule is shown in Figure 5.3.1, indicating a wide isotopic distribution. Parallel Mass Spectrometry Imaging (MSI) using Desorption ElectroSpray Ionization (DESI) and Matrix Assisted Laser Desorption/Ionization (MALDI) were performed to corroborate PIR-LAESI images of the exogenous agent.

5.3.1 Motivation

The ability to verify the distribution of contrast agents within biological tissues is key to successful development of novel agents. Gadolinium-based contrast agents, routinely used in medical applications, have been subjected to Matrix Assisted Laser Desorption/Ionization Mass Spectrometry Imaging (MALDI-MSI) under vacuum [15] [16], highlighting the utility of

MALDI-MSI in the detection of MRI contrast agents within the tissue as a verification tool that complements in vivo MRI results. In the quest to facilitate the detection of contrast agents under ambient conditions while preserving the native molecular information such as metabolism, aggregation and binding etc., gentle laser-based mass spectrometry imaging technologies are particularly useful. In MALDI-MSI the analysis can be done under both vacuum and atmospheric pressure condition with the application of a matrix material that enhances the ionization. In addition to matrix deposition artifacts that could lead to false localization of tissue molecules [17], the complicated sample preparation process further limits in vivo applications of MALDI for surgical guidance. PIR-LAESI as a laser based ambient ion sources, on the other hand, does not require matrix compounds also alleviating the need for vacuum, which makes PIR-LAESI a very promising ion source to provide real-time molecular guidance during surgeries using PIRL as a scalpel with minimum thermal damage.

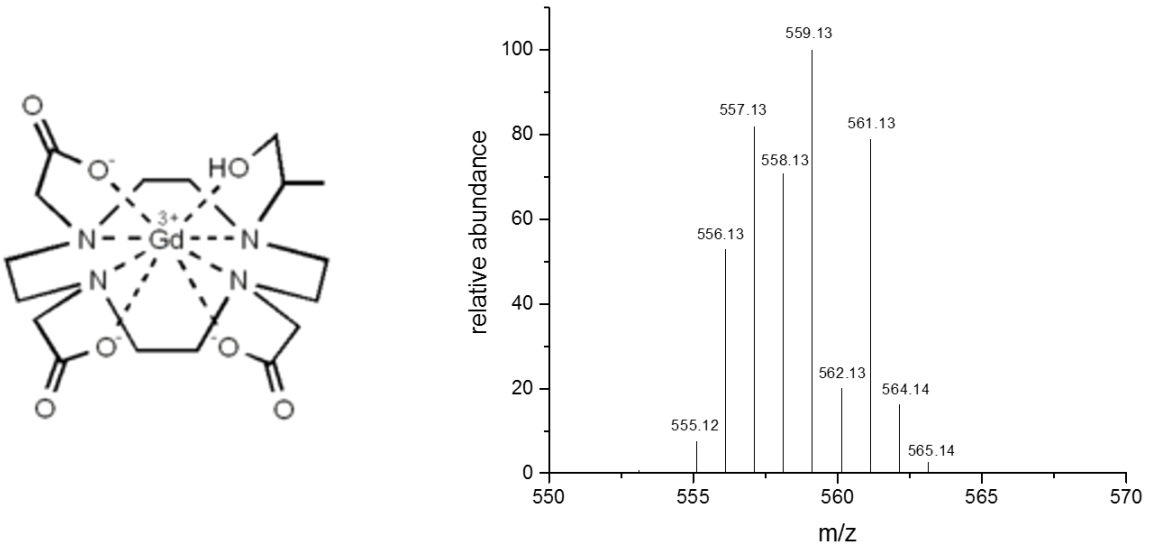

Figure 5.3.1 Structure and isotopic distribution of Gadoteridol.

5.3.2 Tissue Sample Preparation and Experimental Setup

Tissue Sample Preparation

All animal studies were conducted in accordance with institutional guidelines and approved by the Animal Use Committee. Severe Combined ImmunoDeficient (SCID) mice received i.v. injections of Gadoteridol (20 ~ 100 µL/25 g). At 5 minutes post injection, the mice were sacrificed with an overdose of isoflurane and subjected to surgical removal of the kidneys.

Excised tissues were frozen using liquid N_2 vapor and stored at -80°C prior to sectioning. Tissues were sectioned transversely using a cryotome (CM 1950, Leica) with a thickness of 20 μm. The tissue sections were mounted onto a homemade stainless steel sample plate that can be fixed onto the sample plate adaptor described in Figure 3.2.7 (Chapter 3). The mounted tissue sections were stored at -80°C and on the day of experiment were transported to the lab with a cooler filled with dry ice. They were kept in the cooler until experiment.

PIR-LAESI Experiment:

The PIR-LAESI experiment was performed on the setup described in Chapter 3 with the same geometry parameters illustrated in Figure 3.2.7. A mixture of MeOH:H_2O (1:1) with 1% acetic acid served as the solvent for ESI. The mounted tissue section (20 μm thick) was placed onto the sample plate adapter which was kept at a temperature of -2°C by the TEC cooler during the experiment. To further assist ion collection by the mass spectrometer, a potential of 400 V was applied to the sample plate. 20 pulses at a repetition rate of 100 Hz were sent for ablation, followed by 3 s dwell time per pixel for the ESI process of the plume to be completed, and for the ions to be collected by the MS. The total recording time per pixel was 3.2 s. With a scan range of 5 mm x 5 mm and a step size of 200 μm between pixels, the total pixel count of an image was 676 corresponding to a total scan time of ~ 36 minutes. Optical images of the section before and after the ablation were taken with a digital camera (Nikon D3200) mounted on a microscope (Nikon SMZ-10).

DESI-MSI Experiments

In DESI-MSI experiments, the tissue sections of 20 μm thick were mounted onto glass slides and placed on a laboratory-built prototype (described in reference [18]) using tape and analyzed afterwards. All MS experiments were performed using a Thermo Fisher Scientific LTQ mass spectrometer (San Jose, CA, USA) controlled by XCalibur 2.0 software (Thermo Fisher Scientific). The MS parameters and the DESI collection geometry were adjusted using the first slice and DESI-MS imaging was performed using the second tissue slice without altering the collection geometry and collection parameters. An MeOH:H_2O (1:1) solution was used as the spray solvent at a flow rate of 1.5 μL/min. This mixture of solvent provided the optimized signal for Gadetoridal. The tissues were scanned using a 2D moving stage with the spatial resolution of 150 μm (i.e. the step size between two consecutive DESI scan lines). The lines were scanned at a

constant velocity in the range of 248 to 414 µm/s and the scan time of the instrument was in the range of 0.43 to 0.56 s. Data were acquired in the positive ion mode over the mass range from *m/z* 500 to 900. MS spectra were processed using Qual Browser Xcalibur. ImageCreator version 3.0 was used to convert the Xcalibur 2.0 mass spectra files (raw) into a format compatible with BioMap (http://www.maldi-msi.org/). The latter was used to process the mass spectral data and to generate 2D molecular maps.

MALDI-MSI Experiments

The kidney tissue block was mounted transversely onto the specimen disc of a cryostat (Leica Microsystems) using a small amount of Optimal Cutting Temperature (OCT) compound (Sakura Finetek, Torrance, CA) on the distal side of the sample as a support. As such, the front side of the sample, exposing the area to be sectioned, was completely free of OCT. The tissue sections were prepared at a thickness of 12 µm at -15°C and mounted onto indium tin oxide (ITO)-coated glass slides. A thin matrix layer was applied to the tissue section using an automated MALDI plate matrix deposition system (TM-Sprayer™, Leap Tecnologies, Carboro, NC). A total of 5 mL of 9-Aminoacridine (9AA; 15 mg/mL in methanol) was sprayed per slide during 4 passes at 80 °C with a velocity of 400 mm/min and a line spacing of 3 mm. The matrix was already optimized for the signal of Gadetoridal.

A time-of-flight tandem mass spectrometer (AB SCIEX TOF/TOFTM 5800 System, AB SCIEX, Ontario, Canada) was used to acquire the images. MALDI mass spectra were obtained using the third harmonic of a Nd:YAG laser (355 nm) with 3 ns pulse duration and 400 Hz repetition rate. The data were acquired in the negative and positive-ion reflector modes using an external calibration method. The standard Gadoteridol (Prohance, Bracco Imaging) was deposited on the ITO-coated slides to recalibrate and minimize the mass shift. In the imaging experiment, a total of 200 laser shots per pixel were delivered (1 s/pixel) with the step size (i.e. the interval between the data points) of 75 µm. The mass data were processed using a specialized script of the Analyst software (AB SCIEX) at a mass resolution of 0.1 Da and the images were visualized using TissueView (AB SCIEX).

Histology Analysis

For each tissue slice subjected to mass spectrometry imaging, a consecutive 5 µm slice was taken for the Hematoxylin and Eosin (H&E) staining. After MALDI imaging, the matrix was removed with cold methanol and the tissue was fixed prior to standard H&E staining. Standard protocols were used for the staining.

5.3.3 Results and Discussion

Figure 5.3.2A shows the PIR-LAESI-MS spectrum of the medulla region of a kidney injected with Gadoteridol [11]. The ions of [Gadoteridol+H]+ of m/z 560.1, [2Gadoteridol+Na+H]2+ of m/z 571.1, [Gadoteridol+Na]+ of m/z 582.1, [2Gadoteridol+Na+K]2+ of m/z 590.1 and [Gadoteridol+K]+ of m/z 598.1 can be seen. In the mass spectrum of the cortex region (Figure 5.3.2B), a much lower ion count for [Gadoteridol+Na]+ of m/z 582.1 was observed (2.5 fold reduction in the ion count compared to medulla). PIR-LAESI images of [Gadoteridol+H]+of m/z 560.1 and [Gadoteridol+Na]+of m/z 582.1 are reported in Figure 5.3.2C. Both adducts, in addition to having the highest accumulation in the medulla, are distributed in the whole tissue, delineating the entire shape of the kidney. The H&E image of a consecutive slice between the tissue sections used for PIR-LAESI-MS and DESI-MS imaging is also given in Figure 5.3.2C. The entire shape of the molecular map of both ions and the H&E image are consistent with each other. To confirm the distribution of Gadoteridol in mice kidney, dynamic contrast-enhanced (DCE) – MR imaging of the renal uptake of Gadoteridol was taken. Figure 5.3.3 shows the representative 2D slices from T2w-DCE-MR imaging show the sequential renal uptake of intravenously injected Gadoteridol, over a 5 minutes time frame. 1 minute post-contrast injection, the contrast agent appears to be distributed throughout the entire kidney, with a preferential accumulation in the medulla (M), as shown by the positive contrast enhancement. Images at 2.5 and 5 minutes post-contrast injection show a gradual washout of the contrast agents, which accumulates in the renal pelvis (R) and ureter (U). The molecular images of Gadoteridol adduction ions thus consists with the MRI images.

Figure 5.3.4 shows the ion abundance of $[Gadoteridol+Na]^+$of *m/z = 582.1* during the entire course of the imaging experiment. The inset in this Figure shows the laser dependence of the $[Gadoteridol+Na]^+$ ion abundance. The ion intensity effectively diminishes in between laser pulses. This suggests that there is little to no carry-over of MS signal between PIRL pulses,

further indicating that in the absence of laser ablation the ESI solvent spray does not produce any parasitic ions from the ablation plume carry over.

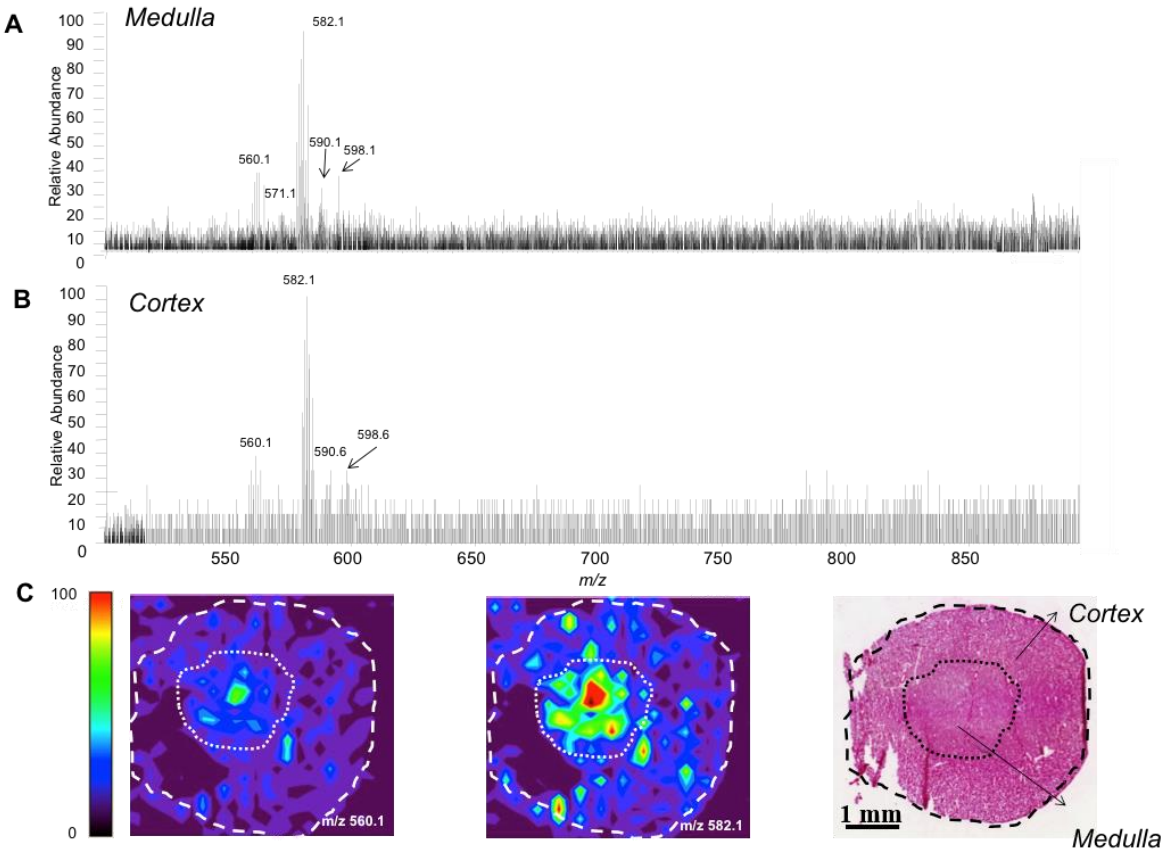

Figure 5.3.2 PIR-LAESI-MS imaging of Gadoteridol in mouse kidney in the positive ion mode. (A) PIR-LAESI-MS averaged spectrum of the medulla region; (B) PIR-LAESI averaged spectrum of the cortex region. In both spectra ion counts relative to [Gadoteridol+Na]+of m/z 582.1 are given. (C) PIR-LAESI-MS images of [Gadoteridol+H]+ of m/z 560.1 and [Gadoteridol+Na]+ of m/z 582.1. The dashed lines delineate the kidney and the medulla boundaries and are presented to guide the eye [11].

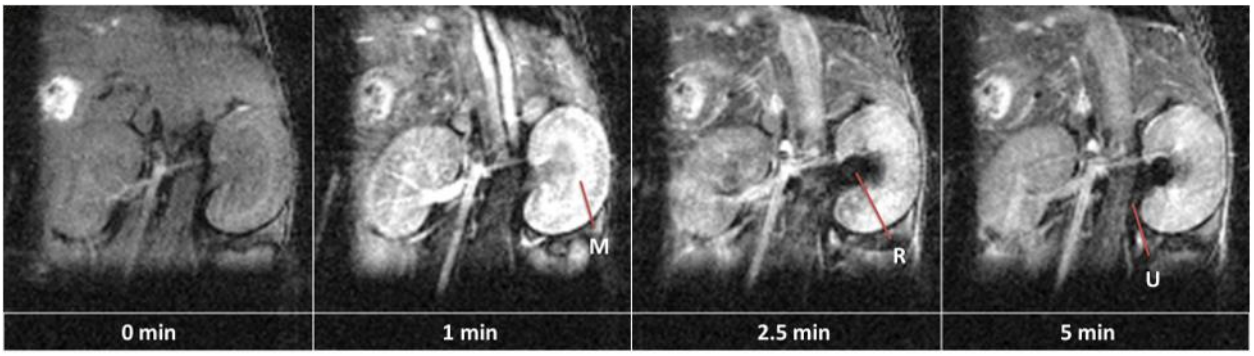

Figure 5.3.3 Dynamic contrast-enhanced (DCE) – MR imaging of mice kidney by renal uptake of Gadoteridol.

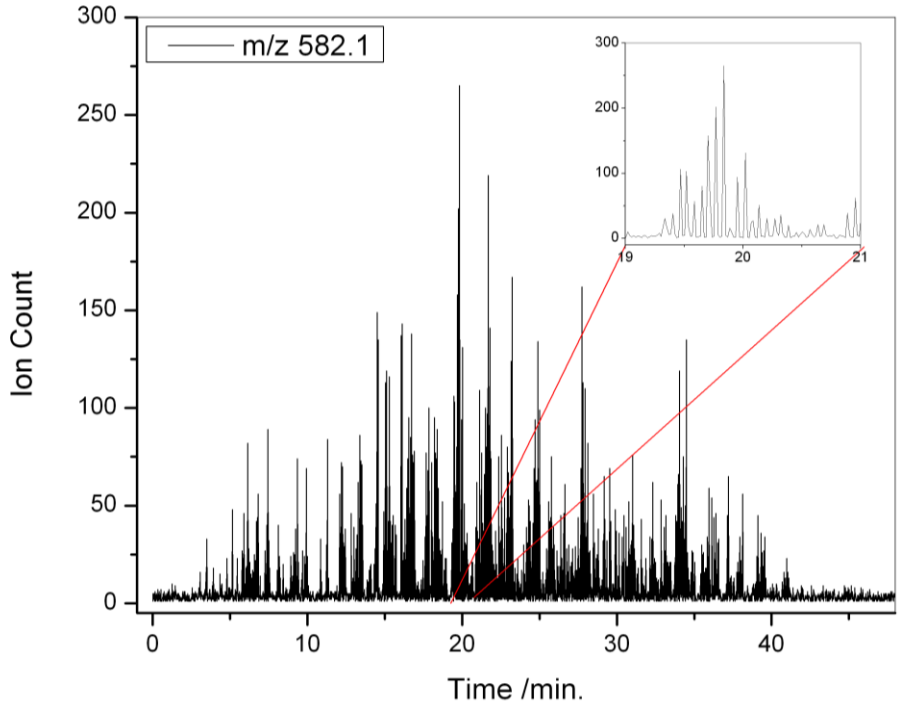

Figure 5.3.4 Extracted ion chromatogram for Gadoteridol adduct *m/z = 582.1*. Insert: zoomed in view of the ion abundance profile [11].

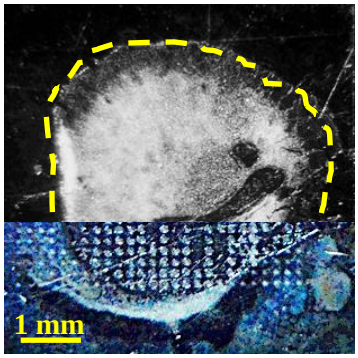

Figure 5.3.5 Optical image of the frozen mouse kidney subjected to PIR-LAESI. The yellow dashed lined delineates the tissue boundaries and is given to guide the eye [11].

Optical images before and after the ablation was shown in Figure 5.3.5 with the background grayscale the image prior PIR-LAESI overlaid with a partial image taken after the experiment (foreground, shaded in blue) illustrating the laser spots. Here, the laser spot size is 100 μm and the pixel step size (i.e. center-to-center distance between two adjacent laser spots) is 200 μm. Twenty pulses were sent to each pixel and the sample thickness was 20 μm. As illustrated in the Figure 5.3.5, the vertical resolution in this particular experiment was better than 20 μm as there is tissue material left at each pixel

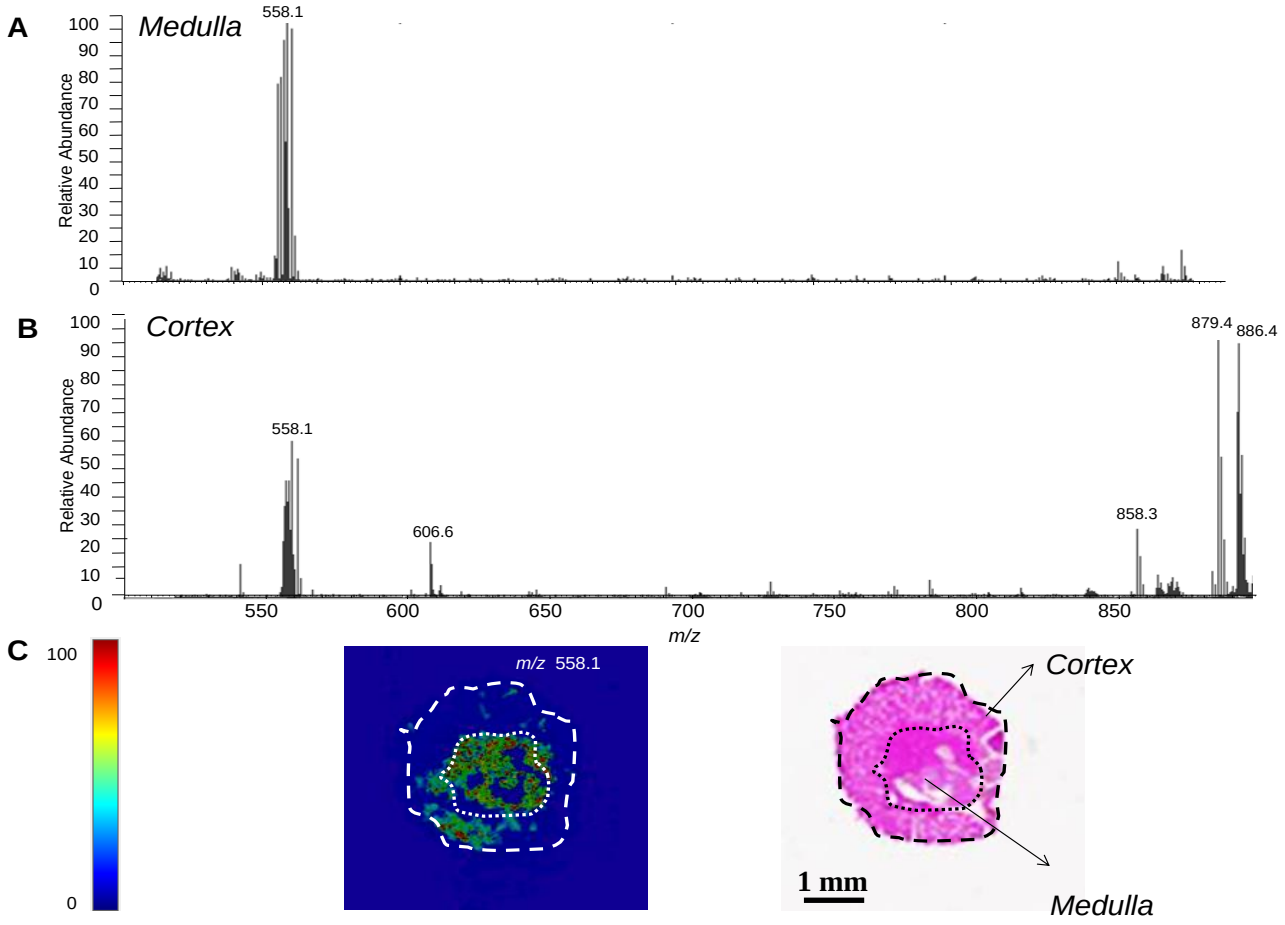

Figure 5.3.6 Contrast-agent MALDI-MS imaging of a mouse kidney injected with Gadoteridol in the negative ion mode. (A) MALDI-MS averaged spectrum of the medulla region; (B) MALDI-MS averaged spectrum of the cortex region. (C) MALDI-MS image of $[Gadoteridol\text{-}H]^-$ of *m/z 558.1* and the H&E image of the tissue slice after MALDI-MS imaging. The dashed lines delineate the kidney and the medulla boundaries and are presented to guide the eye [11].

For comparison, a slice of the same mouse kidney consecutive to the one analyzed by PIR-LAESI-MSI was subjected to MALDI-MSI, a well-established laser-based MS technique to corroborate PIR-LAESI images. MALDI-MSI experiments were run both in the positive and in the negative ion modes. Unfortunately, in the positive ion mode Gadoteridol was not efficiently ionized. As such, we used the negative ion mode results for our comparative molecular imaging. The results are shown in Figure 5.3.6 [11]. The MALDI-MS spectrum of Gadoteridol obtained directly from the kidney shows the prominent ionic species $[Gadoteridol\text{-}H]^-$ with the characteristic Gadolinium isotopic pattern and the monoisotopic peak of *m/z = 558.1*. Figure 5.3.6A and Figure 5.3.6B show, respectively, the averaged spectra in the medulla and at an

arbitrary point in the kidney cortex sampled by MALDI imaging. In both spectra ion counts relative to *m/z = 558.1* are given. The total [Gadoteridol-H]$^-$ of *m/z = 558.1* ion count in medulla and the cortex were 1.2 x 10^4 and 3.0 x 10^3, respectively. The lipid profile of the cortex region can be also observed on the right side of Figure 5.3.6B. Figure 5.3.6C shows the molecular image of the main species [Gadoteridol-H]$^-$ *m/z = 558.1* as well as the H&E image. In MALDI-MSI, the molecular map did not show the presence of Gadoteridol in the entire kidney tissue as revealed by PIR-LAESI analysis in Figure 5.3.2.

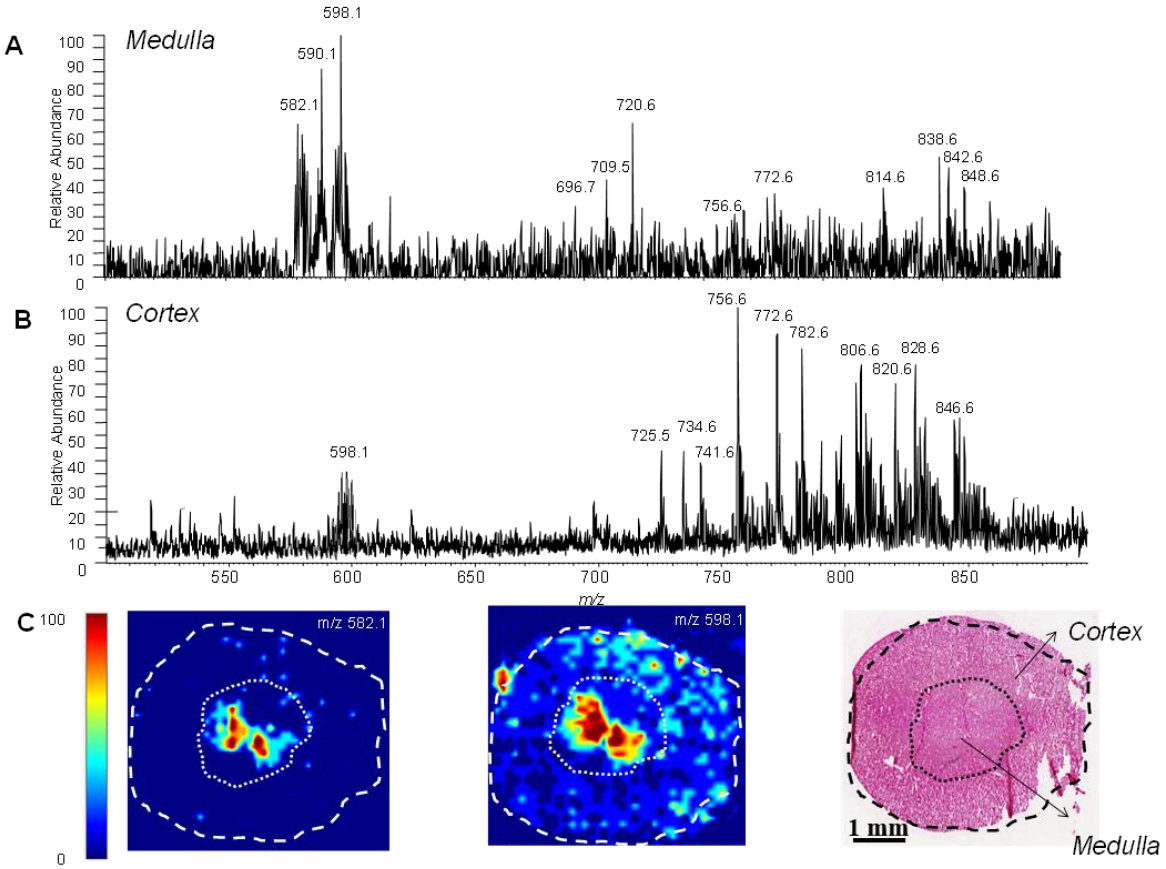

Figure 5.3.7 Contrast-agent DESI-MS imaging of the mouse kidney using Gadoteridol in the positive ion mode. (A) DESI-MSI averaged spectrum of the medulla region; (B) DESI-MSI averaged spectrum of the cortex region (C) DESI-MS image of [Gadoteridol+Na]$^+$of *m/z 582.1* and [Gadoteridol+K]$^+$ of *m/z=598.1*. The dashed lines delineate the kidney and the medulla boundaries and are included to guide the eye [11].

Gadoteridol, accumulated in the kidney, appears as three cationized species [Gadoteridol+Na]$^+$, [Gadoteridol+K]$^+$ and [2Gadoteridol+Na+K]$^{++}$ of *m/z = 582.1*, *598.1* and *590.1*, respectively when subjected to DESI-MS. A kidney slice consecutive to the one analyzed in Figure 5.3.2 with PIR-LAESI was used for DESI-MS. Figure 5.3.7A and Figure 5.3.7B show the averaged

spectrum at an arbitrary point in the medulla and in the cortex, respectively. The ion count of $[Gadoteridol+K]^+$ of *m/z = 598.1* in the cortex (0.8×10^1) was significantly lower than the value of 7.3×10^1 observed in the medulla. The lipid profile of the cortex region can also be observed on the right side of Figure 5.3.7B. The Gadoteridol distribution in the kidney mapped by DESI-MSI is shown in Figure 5.3.7C. Adduct $[Gadoteridol+Na]^+$ is accumulated in the medulla. Adduct $[Gadoteridol+K]^+$ is highly accumulated in the medulla and is ubiquitously distributed in the rest of the tissue, delineating the entire shape of the kidney slice.

Both ambient mass spectrometry ionization techniques DESI and PIR-LAESI were found to have utility for *in situ* analysis of the distribution of Gadoteridol within biological tissues. While DESI and PIR-LAESI were demonstrated here to be able to track Gadoteridol distribution in tissues, MALDI-MSI using the matrix material employed in this study only reported Gadoteridol in the medulla where its concentration was the highest.

5.4 Conclusions and Prospects of PIR-LAESI as Ion Source

PIR-LAESI is an ion source for mass spectrometry that is capable of endogenous and exogenous small molecule imaging. Ionization of biological small molecules from plants and animal by PIR-LAESI was validated. Images of molecular distribution in both plant and animal sources match the optical image correctly. Lipid and protein profiling with MS is a powerful tool to characterize cancers and to also classify different types of human tumors [19]. Our proof of principle demonstration of the utility of PIRL-LAESI-MS in lipid analysis and protein analysis opens up a wide spectrum of applications in cancer characterization to this ion source. PIR-LAESI offers a 3 fold improvement in lateral resolution as a consequence of the improved beam quality for picosecond sources compared to nanosecond LAESI lasers.

Beyond the advantages in drug and metabolite distribution analysis PIR-LAESI-MS may offer additional, yet to be fully tested, possibilities. During intraoperative applications PIR-LAESI-MS could deliver molecular maps of the tissue without spraying solvent on open wounds as with DESI [20] [21] or burning the tissues as with electrocautery [22]. The compatibility with contrast agent imaging could allow surgical navigation from MS analysis of the plume of ablated tumors targeted with exogenous imaging agents. Through tightly focusing the PIRL laser beam intraoperative molecular maps could be available at a spatial resolution that exceeds that of

current DESI-MS methods. Reducing the size of the laser beam can open up new possibilities in more accurately delineating disease margins during surgery. Modulating the PIRL laser power may allow operation in “analysis” as well as “removal” modes to conserve healthy tissues. This feat is unmatched by the current implementation of the iKnife technology that requires active vigorous cutting by electrocautery to deliver molecular information. While effective cutting of bone and tooth enamel have been reported by PIRL [23] we are in the process of assessing the dependence of PIRL desorption on the water content of target tissues.

References of Chapter 5

[1] P. Nemes and A. Vertes, “Laser Ablation Electrospray Ionization for Atmospheric Pressure, in Vivo, and Imaging Mass Spectrometry,” Anal. Chem., vol. 79, no. 21, pp. 8098–8106, Nov. 2007.

[2] A. Vertes, P. Nemes, B. Shrestha, A. A. Barton, Z. Chen, and Y. Li, “Molecular imaging by Mid-IR laser ablation mass spectrometry,” Appl. Phys. A, vol. 93, no. 4, pp. 885–891, Jul. 2008.

[3] Y. H. Rezenom, J. Dong, and K. K. Murray, “Infrared laser-assisted desorption electrospray ionization mass spectrometry,” The Analyst, vol. 133, no. 2, pp. 226–232, Feb. 2008.

[4] Y. Li, B. Shrestha, and A. Vertes, “Atmospheric Pressure Infrared MALDI Imaging Mass Spectrometry for Plant Metabolomics,” Anal. Chem., vol. 80, no. 2, pp. 407–420, Jan. 2008.

[5] P. Nemes, A. A. Barton, Y. Li, and A. Vertes, “Ambient Molecular Imaging and Depth Profiling of Live Tissue by Infrared Laser Ablation Electrospray Ionization Mass Spectrometry,” Anal. Chem., vol. 80, no. 12, pp. 4575–4582, Jun. 2008.

[6] P. Nemes, A. A. Barton, and A. Vertes, “Three-Dimensional Imaging of Metabolites in Tissues under Ambient Conditions by Laser Ablation Electrospray Ionization Mass Spectrometry,” Anal. Chem., vol. 81, no. 16, pp. 6668–6675, Aug. 2009.

[7] B. Shrestha, P. Nemes, J. Nazarian, Y. Hathout, E. P. Hoffman, and A. Vertes, “Direct analysis of lipids and small metabolites in mouse brain tissue by AP IR-MALDI and reactive LAESI mass spectrometry,” The Analyst, vol. 135, no. 4, p. 751, 2010.

[8] P. Nemes, A. S. Woods, and A. Vertes, “Simultaneous Imaging of Small Metabolites and Lipids in Rat Brain Tissues at Atmospheric Pressure by Laser Ablation Electrospray Ionization Mass Spectrometry,” Anal. Chem., vol. 82, no. 3, pp. 982–988, Feb. 2010.

[9] B. Shrestha, R. Javonillo, J. R. Burns, Z. Pirger, and A. Vertes, “Comparative local analysis of metabolites, lipids and proteins in intact fish tissues by LAESI mass spectrometry,” The Analyst, vol. 138, no. 12, p. 3444, 2013.

[10] B. Shrestha, P. Sripadi, B. R. Reschke, H. D. Henderson, M. J. Powell, S. A. Moody, and A. Vertes, “Subcellular Metabolite and Lipid Analysis of Xenopus laevis Eggs by LAESI Mass Spectrometry,” PLoS ONE, vol. 9, no. 12, p. e115173, Dec. 2014.

[11] J. Zou, F. Talbot, A. Tata, L. Ermini, K. Franjic, M. Ventura, J. Zheng, H. Ginsberg, M. Post, D. R. Ifa, D. Jaffray, R. J. D. Miller and A. Zarrine-Afsar, "Ambient Mass Spectrometry Imaging with Picosecond InfraRed Laser Ablation ElectroSpray Ionization (PIR-LAESI)", Anal. Chem., submitted July 2015, under processing.

[12] L. M. L. Nollet, Food Analysis by HPLC, Second Edition. CRC Press, 2000.

[13] M.-I. Aguilar, HPLC of Peptides and Proteins: Methods and Protocols. Springer Science & Business Media, 2004.

[14] J. Zaia, “The correct molecular weight of myoglobin, a common calibrant for mass spectrometry,” Rapid Commun. Mass Spectrom., vol. 6, no. 1, pp. 32–36.

[15] E. Acquadro, C. Cabella, S. Ghiani, L. Miragoli, E. M. Bucci, and D. Corpillo, "Matrix-Assisted Laser Desorption Ionization Imaging Mass Spectrometry Detection of a Magnetic Resonance Imaging Contrast Agent in Mouse Liver," Anal. Chem., vol. 81, no. 7, pp. 2779–2784, Apr. 2009.

[16] M. Aichler, K. Huber, F. Schilling, F. Lohöfer, K. Kosanke, R. Meier, E. J. Rummeny, A. Walch, and M. Wildgruber, "Spatially Resolved Quantification of Gadolinium(III)-Based Magnetic Resonance Agents in Tissue by MALDI Imaging Mass Spectrometry after In Vivo MRI," Angew. Chem. Int. Ed., vol. 54, no. 14, pp. 4279–4283, Mar. 2015.

[17] J. Hankin, "Sublimation as a method of matrix application for mass spectrometric imaging," J. Am. Soc. Mass Spectrom., vol. 18, no. 9, pp. 1646–1652, Sep. 2007.

[18] L. S. Eberlin, A. L. Dill, A. J. Golby, K. L. Ligon, J. M. Wiseman, R. G. Cooks, and N. Y. R. Agar, "Discrimination of human astrocytoma subtypes by lipid analysis using desorption electrospray ionization imaging mass spectrometry," Angew. Chem. Int. Ed Engl., vol. 49, no. 34, pp. 5953–5956, Aug. 2010.

[19] L. S. Eberlin, I. Norton, A. L. Dill, A. J. Golby, K. L. Ligon, S. Santagata, R. G. Cooks, and N. Y. R. Agar, "Classifying human brain tumors by lipid imaging with mass spectrometry," Cancer Res., vol. 72, no. 3, pp. 645–654, Feb. 2012.

[20] S. Santagata, L. S. Eberlin, I. Norton, D. Calligaris, D. R. Feldman, J. L. Ide, X. Liu, J. S. Wiley, M. L. Vestal, S. H. Ramkissoon, D. A. Orringer, K. K. Gill, I. F. Dunn, D. Dias-Santagata, K. L. Ligon, F. A. Jolesz, A. J. Golby, R. G. Cooks, and N. Y. R. Agar, "Intraoperative mass spectrometry mapping of an onco-metabolite to guide brain tumor surgery," Proc. Natl. Acad. Sci. U. S. A., vol. 111, no. 30, pp. 11121–11126, Jul. 2014.

[21] D. Calligaris, D. Caragacianu, X. Liu, I. Norton, C. J. Thompson, A. L. Richardson, M. Golshan, M. L. Easterling, S. Santagata, D. A. Dillon, F. A. Jolesz, and N. Y. R. Agar, "Application of desorption electrospray ionization mass spectrometry imaging in breast cancer margin analysis," Proc. Natl. Acad. Sci. U. S. A., vol. 111, no. 42, pp. 15184–15189, Oct. 2014.

[22] J. Balog, L. Sasi-Szabó, J. Kinross, M. R. Lewis, L. J. Muirhead, K. Veselkov, R. Mirnezami, B. Dezső, L. Damjanovich, A. Darzi, J. K. Nicholson, and Z. Takáts, "Intraoperative tissue identification using rapid evaporative ionization mass spectrometry," Sci. Transl. Med., vol. 5, no. 194, p. 194ra93, Jul. 2013.

[23] K. Franjic, M. L. Cowan, D. Kraemer, and R. J. D. Miller, "Laser selective cutting of biological tissues by impulsive heat deposition through ultrafast vibrational excitations," Opt. Express, vol. 17, no. 25, pp. 22937–22959, Dec. 2009.

Chapter 6
Molecular Dynamics Simulation of Ablation by Desorption Impulsive Vibrational Excitation (DIVE): For Mass Spectrometry at the Fundamental Limits of Biodiagnostics

6.1 Introduction and Motivation

The innovation of the most widely used ion sources, Matrix Assistant Laser Desorption/Ionization (MALDI) [1][2] and Electrospray Ionization (ESI) [3][4], immediately brought MS technology into an era of biochemical analysis. The techniques allowed, for the first time, the identification of large molecules including proteins, which directly led to the emergence of proteomics as a new branch of research in the last decade of the 20th century [5]. The importance of this development cannot be overstated. Given that proteins are the biological endpoints which control most biological processes, it is not surprising that most of the MS-based proteomics studies are focused on discovering novel biomarkers [6]. However, the number of biomarkers entering the clinic has not increased in the past 20 years due to relatively high false-positive rates. One of the main reasons causing the high false-positive rates is the lack of rigorous validation over vast variability of sample collection and preparation [7]. But without quantitative information, most changes resulting from any perturbation during sample collection/preparation is not detectable [8]. Limited by the nature of chemical ionization, neither MALDI nor ESI is inherently a quantitative analysis tool as discussed in Chapter 2. Scientists have made extraordinary progress towards making MALDI and ESI more quantitative by chemical modification of the proteins or by adding internal standard to the sample [9][10], which introduces complexity thus variability in sample preparation and also the ion sources more expensive. Moreover, the chemical modification is usually only valid for a certain type of molecules, which prevents ESI and MALDI to be a general quantitative ion source. To overcome this barrier, an intrinsically quantitative ion source is needed, with a design that is based on deterministic ionization process which is usually based on physical ionization mechanism. The most widely used physical ionization ion source is atmosphere pressure laser ionization (APLI) which utilizes a UV laser to strip off an electron from gas phase molecules [11]. APLI can only

ionize small volatile molecules since large molecules like proteins are difficult to be brought into gas phase intact without being denatured.

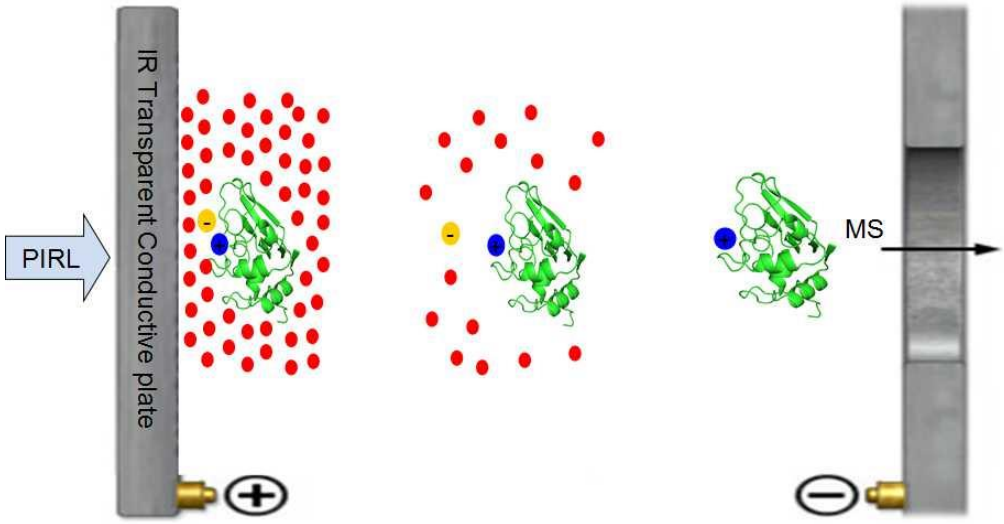

Figure 6.1.1 Ablation of an ionic aqueous protein solution driven by DIVE and ion separation. Red: water molecules (only oxygen shown); blue: Na^+ ion; yellow: Cl^- ion; green: lysozyme molecule.

The new desorption method developed in our group, Desorption Impulsive Vibrational Excitation (DIVE) [12], has made it possible to create an ion source that can bring even large protein molecules, intact, into the gas phase directly from their native environment, e.g serum, urine, lymph fluid etc. The details of the DIVE process have been discussed in Chapter 2 and a possible scenario of the ablation process to be simulated is shown in Figure 6.1.1. Proteins in biological solutions exist with salt ions attached with counter ions nearby the charged site. In our simulation system, lysozyme was used as a representative protein (green in Figure 6.1.1) with water molecules surrounding it (red in Figure 6.1.1). To simplify the calculation, single positive charge was attached on the surface of each lysozyme molecule and single negative charge was attached to the same amount of water molecules to ensure the system was neutral. To make the charge separation process clearer, in Figure 6.1.1, the blue ball represents the positive charge attached on lysozyme and the yellow ball represents the negative counter charge. The breaking of hydrogen bonds in the solution during ablation releases the lysozyme with its attached positive charge, leaving the counter negative ions available to be stripped off. If an external electric field is applied, the protein ions and the counter ions can be separated. The protein ions are guided into MS by the electric field for analysis and detection. The remaining water vapor and counter ions can then be pumped out by the vacuum system. This process is independent of the type or

size of the molecules, and eliminates ion suppression in the ionization process. Because ion recombination is eliminated by the electric field, almost 100% of the salted protein ions will survive during their trip from the source to the mass analyzer, which consequently could increase the sensitivity of MS by several orders of magnitude based on just the solid angle for collection. The ion source will allow for quantitative MS for biochemical analysis without complex sample preparation and will push current MS technology down to the fundamental limit of biodiagnostics according to a particular analyte's abundance of 10^{-22} mole within single cells. Currently, most commercial mass spectrometers can only detect analyte within the range of attomole (10^{-18} mole) [13] and only a few reports indicate that their instrument has sensitivity of zeptomole (10^{-21} mole) with a special design of the matrix for MALDI [14].

Molecular level simulations are necessary to completely understand the prescribed ablation and ionization process. Numerous MD simulations have been performed for ablation by short laser pulses on solid matrixes in order to understand the mechanism in MALDI [15]. The plume characteristics (temperature, pressure, etc.) following DIVE ablation have been determined both experimentally and from numerical simulation of the dynamic equations of state for pure liquid water [12]. However, to our knowledge none of these simulations have been applied to study the ablation process of ionic aqueous solutions and most important not in the presence of a high extraction field to enable both isolation of the intrinsic ions and unit collection efficiency.

The presented MD simulation in this chapter is aimed at providing the microscopic details of the ablation of aqueous ionic protein solutions under DIVE conditions and the necessary extraction field conditions to attain single molecule collection/detection efficiency：the ultimate limit to bio-diagnostics. These parameters will be critical for the development of ion sources based on DIVE with the distinct possibility of enabling single molecule detection.

Specifically, the simulation will answer the following two questions:

Q1: What are the characteristics of the ablation process when ions are present in the solution? With charges present, the Coulomb forces must be taken into account in the equations of motion of each molecule. Due to the long distance of the Coulomb forces, ions will not only interact with ions inside the computation volume but also interact with ions outside. Extended boundary

conditions will be applied for calculation of this long distance force. Simulations will reveal the plume characteristics such as temperature, pressure etc.

Q2: What is the effect of the external electric field on the ablation process? Comparable simulation will be performed with external electric field applied parallel to the incident PIRL laser beam in the ablation area with different field strength. The simulation will provide insight into the plume propagation with an electric field present and the required magnitude of the electric field needed to strip off counter ions from salted protein ions and prevent the recombination of the two. Simulation on the same system without electric field applied will also be performed for comparison.

Under the same electric field, the concentration of ions determines the ionization efficiency. The highest ion concentration in a biological system is the potassium ions (K^+) in the cell and sodium ions (Na^+) in the blood, both on the level of 400 mM [16]. The normal protein number density in cells is on the order of ~ 5 million proteins per cubic micron, that is 8.3 mM [17]. For simplicity, the simulation presented in this thesis was performed at the protein concentration of 8.3 mM with each protein singly charged, which means the ion concentration was the same as the proteins rather than 400 mM. Instead of adding salt ions into the system, each protein was attached with a single positive charge (e^+) and the surrounding water molecule was attached with a single negative charge (e^-) to keep the system neutral. Under this condition, computation volume of size 20 nm × 20 nm × 70 nm contained 140 proteins and ~ 1 million water molecules. For such a large system, coarse-grain methods and parallel calculations were utilized to increase the calculation efficiency. Simulation with different electric field strengths, 10^5 V/m, 10^6 V/m and 10^7 V/m anticipated experimental conditions. Each simulation ran for 1 ns with a 100 ps laser pulse applied.

6.2 Model Description

6.2.1 Coarse-grained MD Model

A coarse-grained MD model that combines the breathing sphere (BS) model developed for simulation of laser interactions with molecular systems [18] [19] [20] with the bead-and-spring model commonly used in modeling of polymers was employed to model the laser ablation of polymer solutions [18] [21]. The technical details of this coarse-grained model can be found in

the recent publication [22] and the main point are briefly detailed here. Figure 6.2.1 shows the sketch of the BS model.

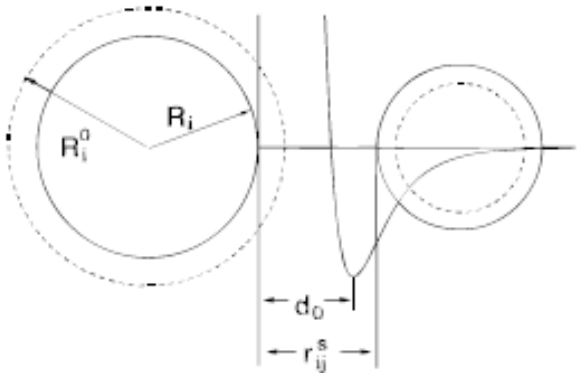

Figure 6.2.1 Sketch of the BS model. R_i^0 and R_i are the equilibrium and instantaneous radii of the particle i; d_0 and r_{ij}^s are the equilibrium and instantaneous distances between the edges of the spherical particles. Reprinted with permission from ref. [19] Copyright © 1997, American Chemical Society.

As shown in Figure 6.2.1, the BS model adapts a coarse-grained representation of molecules by spherical particles each having one dynamic internal degree of freedom, allowing the particle size R_i to change or to "breathe", besides the three degrees of freedom corresponding to its translational motion (r_i: x, y, z). The breathing motion is controlled by an inertia parameter (or effective mass) M_I ascribed to the corresponding breathing degree of freedom and an anharmonic potential [19]

$$U_R(R_i) = k_1(R_i - R_i^0)^2 + k_2(R_i - R_i^0)^3 + k_4(R_i - R_i^0)^4 \tag{6.2.1}$$

where R_i is the instantaneous radius of particle i and k_1, k_2 and k_3 are parameters of the potential. The translational motion is defined by the intermolecular interactions that are described by the Morse potential, originally developed for description of diatomic molecules [23], and later adopted for intermolecular non-bonding interactions, *e.g.*[18] [19] [20] [24] [25]. The functional form of the Morse potential is

$$U_r(r_{ij}^s) = D_e\{\exp[-2\beta(r_{ij}^s - d_0)] - 2\exp(-\beta(r_{ij}^s - d_0)]\} \tag{6.2.2}$$

where r_{ij}^s is the distance between edges of two breathing sphere particles i and j : $r_{ij}^s = |\vec{r}_i - \vec{r}_j| - R_i - R_j$, $\vec{r}_i$ and $\vec{r}_j$ are positions of particles i and j, respectively, R_i and R_j are their

radii. The parameters of the Morse potential, D_e, β, and d_0, along with the mass M and the equilibrium radius R_i^0 of a breathing sphere particle, are defining the physical properties of the model material. Thus, the forces exerted on the translational (r) and breathing (R) freedom of particle i are

$$\vec{F}_1(r_i) = -\sum_j \frac{\partial U_r(r_{ij}^s)}{\partial r_{ij}^s}\frac{\partial r_{ij}^s}{\partial r_i}, \vec{F}_1(R) = -\frac{\partial U_R(R_i)}{\partial R_i} - \sum_j \frac{\partial U_r(r_{ij}^s)}{\partial r_{ij}^s}\frac{\partial r_{ij}^s}{\partial R_i} \tag{6.2.3}$$

where the summation is over all neighboring particles of particle i within interaction distance.

It can be seen that the breathing motion and the translational motion are coupled with each other, with the coupling strength controlled by the parameters k_1, k_2 and k_3 .The choice of the parameters, therefore, can be used to ensure that the rate of the energy equilibration between the optically-excited molecules and their surroundings matches the results of pump-probe experiments or atomistic simulations [19][20].

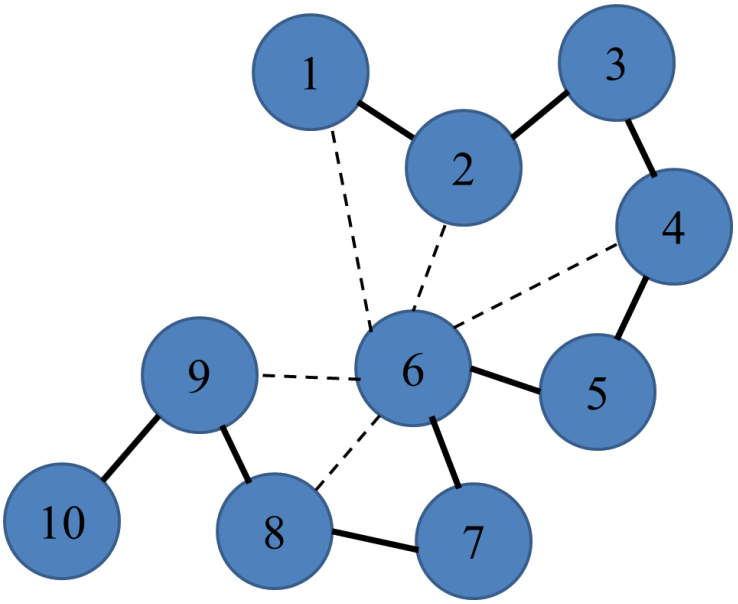

Figure 6.2.2 Sketch of an example polymer chain of 10 beads. The chemical bond is represented by the solid line. Except the bead at the end of polymer chain, such as the bead 1 and 10, all other beads can be chemically bonded with 2 beads. Non-bonded beads, if they are within interaction distance, interact with nonbonding interaction, are indicated by the dashed lines.

In the present work of modeling the polymer-water system, both water and polymer beads were represented by BS particles. The polymer was modeled as a chain of polymer beads with neighboring beads chemically bonded as in the Fig. 6.2.2.

The parameters of the internal potential given by Eq. (6.2.1), $k_1 = 10$, $k_2 = -20$ and $k_3 = 20$ were chosen to ensure that the equilibration time between the translational and breathing modes is ~ 20 ps for both water and lysozyme at room temperature. The rate of the vibrational equilibration is faster at higher temperatures and under conditions of optical excitation of the breathing mode. Under any conditions, the equilibration time is much shorter than the laser pulse duration of 100ps used in the simulations.

The parameters of the intermolecular potential, Eq. (6.2.2), for the water component, *M = 50 Da*, $R_0 = 0.8$ Å, D_e = *-0.045 eV*, $d_0 = 3.0$ Å, and $\beta = 1.3$ Å^{-1}, were chosen and found to provide a satisfactory semi-quantitative description of the experimental properties of water. The parameters of the Morse potential for non-bonding interactions between polymer beads, *M = 111 Da*, $R_0 = 1.4$ Å, D_e = *0.15 eV*, $d_0 = 2.8$ Å, and $\beta = 0.9$ Å^{-1} were chosen to roughly reproduce the typical strength of non-bonding interactions in proteins and the equilibrium dimensions of a lysozyme globule [26]. The intramolecular "springs" in the bead-and-spring model, corresponding to the chemical bonds between the polymer units, were described by the same Morse potential given by Eq. (6.2.2), with parameters D_e = *3.48 eV*, $\beta = 2.37$ Å^{-1} and $d_0 = 1.54$ Å chosen to represent a typical carbon-carbon bond in a polymer molecule [18].

6.2.2 Heat Bath

As discussed above, each BS particle in the coarse-grained model represents a group of atoms. For example, a BS water particle of mass of 50 Da models a cluster of ~ 3 water molecules as a unit. However, each BS particle has only four dynamic degrees of freedom corresponding to the radial breathing and translational motions, which are drastically reduced, as compared to real molecular systems, leading to a substantial underestimation of the heat capacity. To reproduce the experimental heat capacity of the modeled material, "heat bath" variables representing the energy content of the vibrational modes that are not explicitly represented in the coarse-grained model were introduced [27]. Technically, a heat bath temperature is associated with each BS particle, with the heat capacity C^{HB} obtained by subtracting the contributions of the dynamic degrees of freedom from the experimental specific heat of the group of atoms represented by the BS particle, $C^{\exp}$, i.e., $C^{HB} = C^{\exp} - C^{TR} - C^{R}$, where $C^{TR} = 3k_B$ is the contribution to the heat

capacity from the three translational degrees of freedom of the dynamic unit and $C^R = k_B$ is the contribution from the radial breathing motion of the unit (k_B is the Boltzmann constant).

The heat bath is directly coupled with the breathing motion of the BS particle, by allowing the energy exchange between the heat bath and the breathing mode at each time-step of the MD integration:

$$C^R \frac{dT_{BS}(i)}{dt} = A(T_{HB}(i) - T_{BS}(i)) \tag{6.2.4}$$

$$C_i^{HB} \frac{dT_{HB}(i)}{dt} = -A(T_{HB}(i) - T_{BS}(i))$$

where A is a constant that controls the rate of the energy exchange, and can be related to the characteristic time τ of the energy exchange between the heat bath and the breathing mode, defined as a time constant of the exponential decay of the difference between the heat bath temperature $T_{HB}(i)$ and the BS temperature $T_{BS}(i)$, as $A = \frac{C_i^{HB}\left(C^{TR} + C^R\right)}{C_i^{HB} + \left(C^{TR} + C^R\right)} \frac{1}{\tau}$.

Note that the coupling between the heat bath and the breathing mode is achieved at the level of individual BS particles. Namely, the heat bath temperature and the BS temperature in the above equations are defined for each BS particle, i.e., $T_{HB}(i)$ and $T_{BS}(i)$ for BS particle *i*. Technically, the BS temperature of each particle is calculated by averaging the total energy over the neighboring particles within the distance of the sum of cutoff and skin depth ($T_{BS}(i) = \frac{\sum_{j=1}^{N} E_j}{Nk_B}$, where N is the number of neighboring atoms and atom *i* itself). For the heat bath, the energy exchange (or coupling) leads to the HB temperature evolution. While for the breathing mode, the energy exchange results in an additional "friction" force, $\varepsilon(i) M_I(i) v_R(i)$ applied to the breathing motion, $M_I(i) \frac{d^2 R(i)}{d^2 t} = F_R(i) + \varepsilon(i) M_I(i) v_R(i)$, where *ε(i)* should be chosen to ensure the desired energy transfer and energy conservation as detailed below. The basic idea is that if we have the energy *ΔE* transferred to BS mode of particle *i* at a time step of *Δt*, we need to require that the

kinetic energy increase of the BS mode due to the additional force of $\varepsilon(i)M_I(i)v_R(i)$ be as close to ΔE as possible, i.e., $\varepsilon(i)M_I(i)v_R(i)\times v_R(i)\Delta t = \Delta E$.

During a single time step Δt, the ideal energy that will be transferred from the HB to BS for a particle i is $\Delta E(i) = \Delta E_{HB\to BS} = A\times(T_{HB}(i) - T_{BS}(i))\times\Delta t$. This amount of energy will be transferred to the particle *i* itself and also its neighboring particles, as the BS temperature is obtained by averaging over neighboring particles. As mentioned above, the energy transferred to the BS mode will induce an additional "friction" force to the Breathing motion. Thus, for the particle *j* (*j* can be particle *i* itself or particle *i*'s neighboring particle), it will have an additional force $\varepsilon_{ij}M_I(j)v_R(j)$ due to this energy transfer, where $\varepsilon_{ij} = \frac{\varepsilon_i}{N}$, $\varepsilon_i = \frac{\Delta E(i)/\Delta t}{k_B T_{BS}(i)}$, which results in a work of $\varepsilon_{ij}M_I(j)v_R(j)\times v_R(j)\Delta t = \frac{\Delta E(i)}{Nk_B T_{BS}(i)}M_I(j)v_R(j)^2$ done on particle *j*. Thus, due to the temperature difference between the heat bath and breathing mode of particle *i*, it results in the total work done on particle *i* itself and its neighboring particles, $\Delta W = \sum_{j=1}^{N}(\frac{\Delta E(i)}{Nk_B T_{BS}(i)}M_I(j)v_R(j)^2) = \frac{\Delta E(i)}{Nk_B T_{BS}(i)}\sum_{j=1}^{N}(M_I(j)v_R(j)^2) = \frac{\Delta E(i)}{Nk_B T_{BS}(i)}\sum_{j=1}^{N}(2K_j)$, where K_j is the kinetic energy of particle *j*. If we calculate the BS temperature of each particle by averaging the kinetic energy over the particle itself and all its neighboring particles, $T_{BS}(i) = \frac{2\sum_{j=1}^{N}K_j}{Nk_B}$, then we will have $\Delta W = \frac{\Delta E(i)}{2\sum_{j=1}^{N}K_j}\sum_{j=1}^{N}2K_j = \Delta E(i)$ and the ideal energy transfer can be achieved. However, the issue is that the BS temperature can be a problem if the density of particle is very low. In the extreme case, there are no neighboring particles around, and the BS temperature can be calculated to be 0, which will lead to an artificial force of infinity.

If we calculate the BS temperature of each particle by averaging total energy over the particle itself and all its neighboring particles, $T_{BS}(i) = \frac{\sum_{j=1}^{N}E_j}{Nk_B}$, then $\Delta W = \frac{\Delta E(i)}{2\sum_{j=1}^{N}E_j}\sum_{j=1}^{N}2K_j \neq \Delta E(i)$ and the ideal energy transfer is not achieved for each atom and each time step. But it is still approximately ideal since our breathing mode is close to harmonic. To ensure energy conservation, $\Delta W(i)$ is then used to update heat bath temperature $T_{HB}(i) = T_{HB}(i) - \Delta W(i)/C_{HB}^i$. In

our implementation, the BS temperatures were calculated for particles with N≥30 by averaging kinetic breathing energy, while for particles with N<30 by averaging total breathing energy. Just as it will distribute energy to its neighbors from HB to BS, particle *i* will also receive energy from its neighbors due to the energy transfer from HB to BS happening at all its neighboring particles *j*. Thus, the Newton equation for the BS mode of the particle *i* should be, $M_I(i)\frac{d^2R(i)}{d^2(t)} = F_R(i) + \varepsilon(i)M_I(i)v_R(i)$, where $\varepsilon(i) = \sum_{j=1}^{N}\varepsilon_{ji}$.

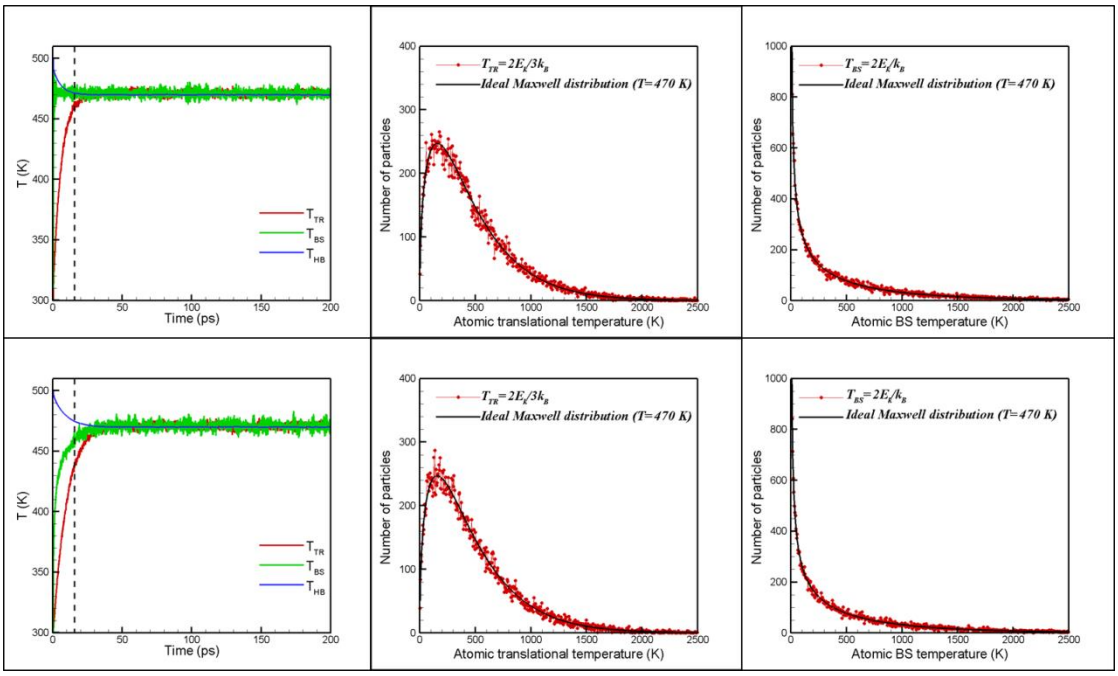

Figure 6.2.3 Coupling of the translational degrees of freedom to the breathing mode and the heat bath. The water system is firstly equilibrated at 300 K without heat bath. Then the heat bath is switched on to run constant energy free dynamics, with the heat bath temperature set initially to be 500 K. The system is expected to be equilibrated to 470 K. The 1st row is the result by choosing $\tau = 1$ *ps*, and the 2nd row is by choosing $\tau = 5$ *ps*. The 1st column is the system temperature evolution. The 2nd and 3rd columns show the distribution for the BS kinetic energy and translational kinetic energy respectively after equilibration with the ideal distribution derived from classical mechanics also shown for comparison. Effectively, perfect agreement is achieved, indicating good implementation.

Overall, vibrational relaxation of the excited molecules proceeds in the model through the energy transfer from the heat bath to the breathing motion and through the dynamic coupling between the breathing and translational modes. In this work, we aimed at the time of tens of picoseconds for the vibrational relaxation, to be consistent with the timescale of vibrational energy relaxation in proteins determined in atomistic simulations and measured in pump-probe experiments [28][29][30]. As discussed in the last section, the equilibration between breathing mode and

translational mode takes ~ 20 ps. Thus the time constant of equilibration between heat bath and breathing motion was set to be ~ 1 ps, to achieve the desired time scale of vibrational relaxation. The test results of the heat bath approach are shown in Figure 6.2.3, showing that the vibrational relaxation time of ~ 20 ps was achieved with $\tau = 1\ ps$, and a perfect agreement with the classical mechanics.

6.2.3 Charge-Charge Interaction

A simple method was applied to prepare the ionized polymer solution. The polymer was made positively charged, by attaching a positive charge (1 e^+) to a polymer bead, typically the surface bead if the polymer was in the shape of a globule. For each positively charged polymer bead, a negative charge was then randomly attached to a neighboring BS water particle with a distance around RBOUND to make the whole system have a zero net charge. The value of RBOUND was taken from the minimum distance between salt ions and counter ions in salt saturated solution, which is 5.4Å [31]. The charges interact with each other through Coulomb interaction. Because of the long range of the Coulomb force, simple periodic boundary conditions could become inadequate, particularly for free, unscreened ions. Conventionally, the Ewald Summation technique is applied for the treatment of such long range interaction [32]. However, its implementation requires extensive effort and we employed an easy alternative of utilizing the extended boundary conditions to calculate interionic interactions [33], where each individual charged particle interacts not only with the other charged particles in the original volume (1 in the following figure), but also with charges in 8 (2 to 9 in the following figure) or 24 (2 to 25 in the following figure) replicated volumes surrounding it in the *x* and *y* lateral directions, as in Figure 6.2.4. Due to the effect of screening and nearly zero net charge density, Coulomb forces and potentials are dominated by relatively nearby ions. Thus, such simple method provides a reasonable description for interionic interaction and the change in net forces and potential energies was small, below 1%. In our program, we had the option to choose between 8 and 24 replicates.

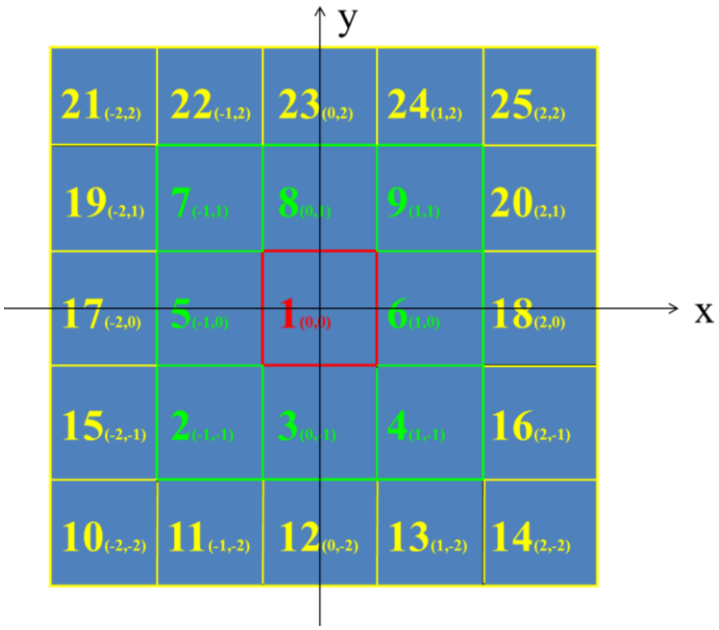

Figure 6.2.4 The extended boundary conditions to calculate interionic interactions by considering charges in 8 or 24 replicated volumes surrounding the current computational cell.

6.2.4 Parallelization for Molecular Dynamics (MD) Simulations

Coarse-grained MD model, Heat Bath and Charge-Charge interaction was first implemented into the classical MD simulation in serial code. However, to simulate a system containing > 1 million particles, serial calculation is not efficient enough. Parallelization of the serial code was thus realized by applying the Message Passing Interface (MPI) communication library to enable this large scale simulation. The basic idea of the parallelization is to divide a “big” calculation into many “small” ones, which are executed by many computer cores in parallel. The calculation speed is increased due to the reduction of calculation load for each core. Information exchange is required between different computer cores during calculation.

System Division into Subdomains

The first step to parallelize MD is to divide the whole computational system into a number of small subdomains as shown in Figure 6.2.5. Particles are assigned to the appropriate subdomains according to their positions. Each particle in the system is assigned a global ID in reference to the whole computational system and also a local ID in reference to the current subdomain where the particle is located. The global ID of each particle is fixed, but the local ID can change as particles can migrate from one subdomain into its neighboring subdomains during system evolution. The subdomains are mapped to a grid of computer cores with each computer core

responsible for the calculation (MD integration) of its corresponding subdomain. The communication between neighboring computer cores has to be performed in order to achieve correct MD integration, especially for the particles near the subdomain boundaries. To ensure that each subdomain communicates with the correct neighboring subdomains, each subdomain (or computer core) is assigned a "global" ID and also the projected IDs in *x*, *y* and *z* directions. This way, each subdomain (or computer core) can easily identify the ID of its neighboring subdomains (computer cores) for communication.

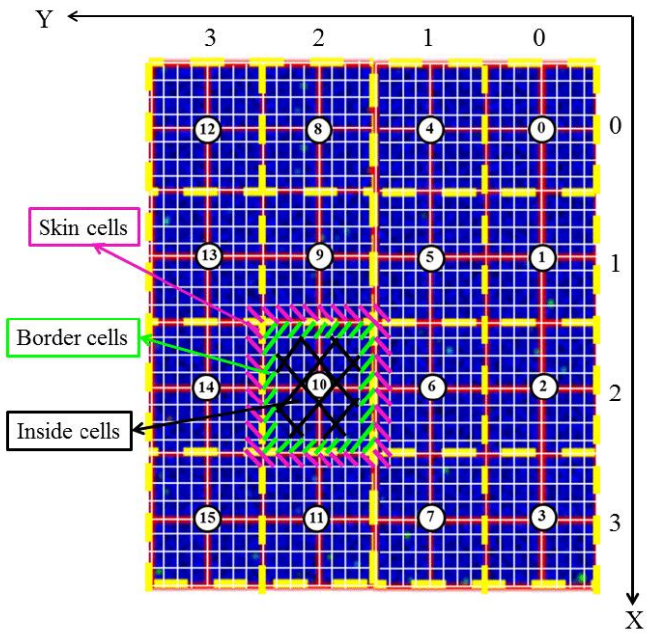

Figure 6.2.5 Spatial division of the MD computational system into subdomains outlined by yellow dashed lines for parallelization. While 3-dimensional division is really performed, 2-dimensional even division is shown here for the only reason of easy presentation. Each subdomain is corresponding to a single computer core. Each subdomain is further divided into MD link cells (white squares). For the convenience of communications with neighboring subdomains, a single-link-cell border layer (green slashes) and a single-link-cell skin layer (purple slashes) are identified for each subdomain, shown for the subdomain 10 as an example.

Subdomain Communication: Link cells, Linked List and Neighbor List

When each subdomain is communicating with its neighbors, it is important to make sure they are exchanging the information of the correct particles. Moreover, sometimes particles near the border of the current subdomain can interact with particles near the border of its neighbor subdomain. To ensure exchange of information or proper interaction between particles in neighboring subdomains, each MD subdomain is further divided into link cells (white squares), with the size a little greater than the particles interaction cutoff distance plus a buffer distance

(1Å), as shown in Figure 6.2.5. The link cells of each subdomain are also assigned with link cell IDs and particles are assigned to the link cells based on their positions. Particles in each link cell are linked in a chain, so called “linked list” [34] [35]

A single border layer of link cells (green slashes) and a single skin layer of link cells (purple slashes) are identified for each subdomain and shown for the subdomain 10 as an example. The communication between neighboring subdomains is actually to exchange information of particles in border and skin cells. It can be seen that the border cell of the current subdomain is the skin cell of its corresponding neighboring subdomain, and vice versa. The information of particles in the border cell of the current subdomain is sent to the corresponding neighboring subdomains, updating the information of particles in their corresponding skin cell.

Taking advantage of the linked list algorithm, the neighbor list of each particle can be constructed by first going through the linked list of the current link cell it is located in and then the 26 neighboring link cells. The particles are counted as neighbors within the range of interaction cut-off distance plus a buffer size ~ 1 Å. Because if particle A is a neighbor of particle B, the particle B must be also a neighbor of the particle A, we can further improve the efficiency of neighbor list generation by only going through 13 neighboring link cells. As the system is evolving, the particles can move from one link cell to another link cell and from one subdomain into another subdomain, thus requiring to renew the linked list and neighbor list, and to reassign (or migrate) particles to its correct computer core(subdomain) from time to time. To save the computational time (the particle’s neighbor list generation is very time consuming), the linked list and neighbor list was renewed every 10 time steps (~ 10 fs), assuming that the particles cannot move beyond 1 Å during 10 fs, i.e., the particle velocity cannot be higher than 10^4 m/s. Thus the link cell must have a size greater than the interaction cut-off distance plus a buffer size. The “migration” process is performed in order to put particles into the correct computer core, by sending particles that move outside of the current subdomain to its neighboring subdomains and receive particles that move into the current subdomain from its neighboring subdomains. The information of particles in the skin cells are updated by communication every time step to ensure the correct MD integration.

MD Integrator

The MD integration was performed with the application of Nordsieck fifth-order predictor-corrector algorithm [34]. This algorithm is one of the most efficient integrators with also good accuracy. As the name of the algorithm suggests, the integration is realized via two steps, the prediction of the particles coordinates for the next time step and the correction of the coordinates according to the force applied on particles. Assume the particle has the coordinate *r(t)* with the corresponding time derivatives $q_1(t) = h\frac{dr}{dt}$, $q_2(t) = \frac{h^2}{2}\frac{d^2r}{dt^2}$, $q_3(t) = \frac{h^3}{6}\frac{d^3r}{dt^3}$, $q_4(t) = \frac{h^4}{24}\frac{d^4r}{dt^4}$, $q_5(t) = \frac{h^5}{120}\frac{d^5r}{dt^5}$, where *h* is the time step of MD integration.

Step 1 Prediction (Nord5_Step1): the particles are moving "by inertia", thus the interactions between particles and any other forces are not taken into account. New values of coordinates and their time derivatives are obtained through Taylor series:

$$
\begin{aligned}
r^p(t+h) &= r(t) + q_1(t) + q_2(t) + q_3(t) + q_4(t) + q_5(t) \\
q_1^p(t+h) &= q_1(t) + 2q_2(t) + 3q_3(t) + 4q_4(t) + 5q_5(t) \\
q_2^p(t+h) &= q_2(t) + 3q_3(t) + 6q_4(t) + 15q_5(t) \\
q_3^p(t+h) &= q_3(t) + 4q_4(t) + 10q_5(t) \\
q_4^p(t+h) &= q_4(t) + 5q_5(t) \\
q_5^p(t+h) &= q_5(t)
\end{aligned}
\qquad (6.2.5)
$$

Step 2 Correction (Nord5_Step2): in this step, the predicted value of particles coordinates are corrected by force which is calculated with the predicted value of particles coordinates. If the corrector is defined as

$$\delta q_2(\mathrm{t}+\mathrm{h}) = \frac{F(t+h)}{2m}h^2 - q_2(\mathrm{t}+\mathrm{h}) \qquad (6.2.6)$$

then the corrections of the predicted coordinates are:

$$
\begin{aligned}
r(\mathrm{t}+\mathrm{h}) &= r^{p}(\mathrm{t}+\mathrm{h}) + \mathrm{C}_0\delta q_2(\mathrm{t}+\mathrm{h}) & C_0 &= \frac{3}{20} \\
q_1(\mathrm{t}+\mathrm{h}) &= q_1{}^{p}(\mathrm{t}+\mathrm{h}) + \mathrm{C}_1\delta q_2(\mathrm{t}+\mathrm{h}) & C_1 &= \frac{251}{360} \\
q_2(\mathrm{t}+\mathrm{h}) &= q_2{}^{p}(\mathrm{t}+\mathrm{h}) + \mathrm{C}_2\delta q_2(\mathrm{t}+\mathrm{h}) & C_2 &= 1 \\
q_3(\mathrm{t}+\mathrm{h}) &= q_3{}^{p}(\mathrm{t}+\mathrm{h}) + \mathrm{C}_3\delta q_2(\mathrm{t}+\mathrm{h}) & C_3 &= \frac{11}{18} \\
q_4(\mathrm{t}+\mathrm{h}) &= q_4{}^{p}(\mathrm{t}+\mathrm{h}) + \mathrm{C}_4\delta q_2(\mathrm{t}+\mathrm{h}) & C_4 &= \frac{1}{6} \\
q_5(\mathrm{t}+\mathrm{h}) &= q_5{}^{p}(\mathrm{t}+\mathrm{h}) + \mathrm{C}_5\delta q_2(\mathrm{t}+\mathrm{h}) & C_5 &= \frac{1}{60}
\end{aligned}
\tag{6.2.7}
$$

Implementation of MD Integration with MPI Communication Interface

In parallel simulation, both communication between neighboring subdomain and the MD integration are time consuming. To make an efficient parallelization, the communication and computation needs to be overlapped as much as possible. To achieve this, a specific algorithm for implementation of Nordsieck fifth-order predictor-corrector MD integrator was developed as shown in Figure. 6.2.6 and discussed in steps as below. To calculate the force of the particle, we need to know both the coordinates of the current particle and its neighboring particles.

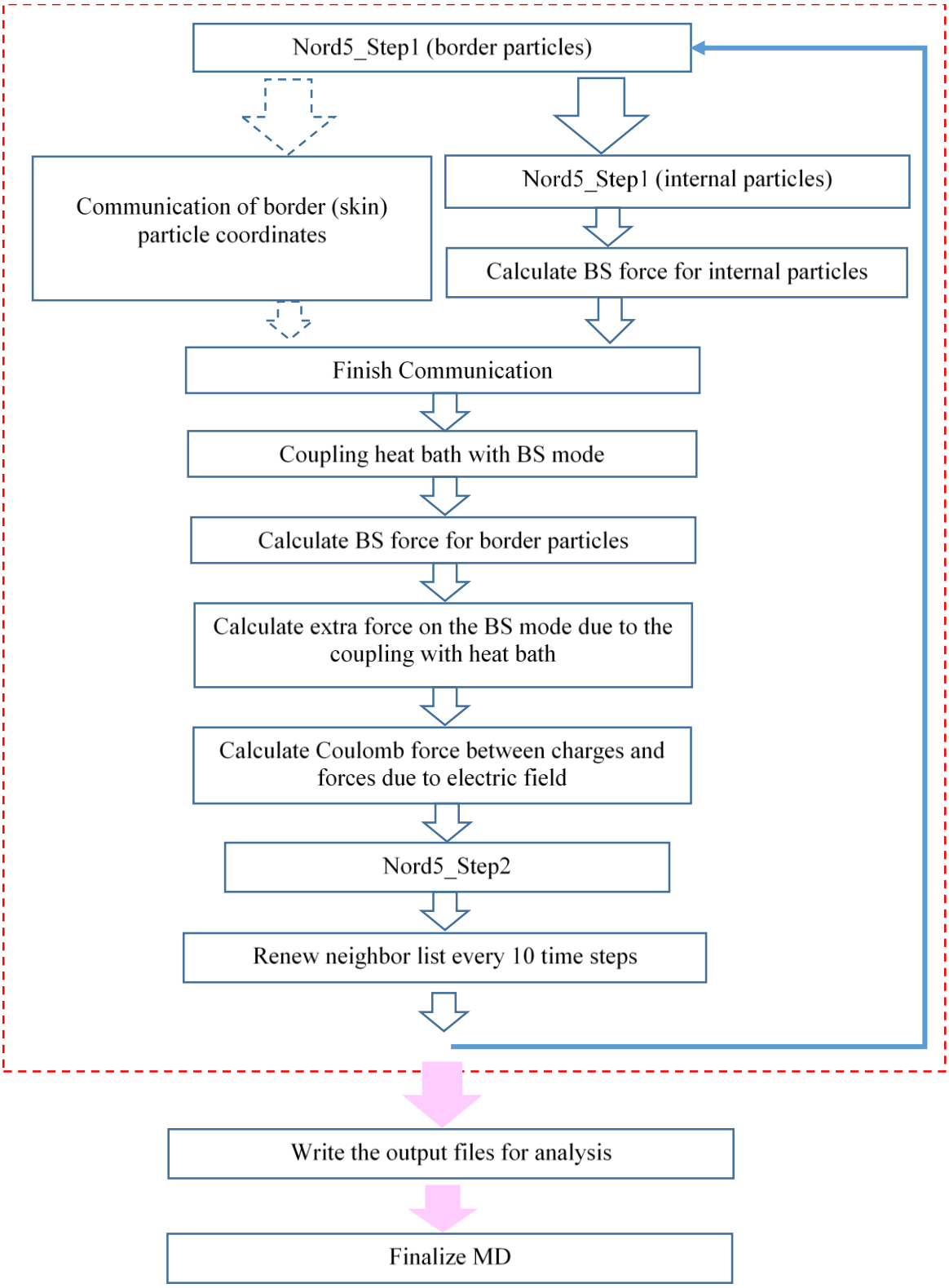

Figure 6.2.6 Algorithm for implementation of Nordsieck fifth-order predictor-corrector MD integrator to achieve MPI parallelization with the overlap of communication and computation.

Step 1: Perform ***Nord5_Step1*** for the particles in border cells, which doesn't require the information of neighboring particles.

Step 2: Sending the above (step 1) newly calculated coordinates of particles in the border cells to the corresponding neighboring subdomain as its skin cells. At the same time, receiving the newly calculated coordinates of particles in the skin cells from the corresponding neighboring subdomains. The computer cores process the communications in background while the computations of Step 3 and 4 are running, allowing the overlap of computation and communication.

Step 3: Perform ***Nord5_Step1*** for the rest of particles in the inside cells of the current subdomain. (During this computation, communication initiated at Step 2 is processed in background.)

Step 4: Calculate the breathing sphere (BS) forces for internal particles with the updated particle coordinates obtained in Step 1 and 3. This does not require the updated coordinates of particles in skin cells, since they must not be the neighbors of particles in the inside cells ensured by the size of the link cell. (During this computation, communication initiated at Step 2 is still processed in background.)

Step 5: "Wait" for the Step 2 communication to complete and update the coordinates of particles in the skin cells of the current subdomain.

Step 6: Coupling heat bath with BS mode using coordinates obtained in Step 1 and 2 for both internal particles and border particles.

Step 7: Calculate breathing sphere forces for border particles as required particle's information in skin cells of neighboring subdomain is already received in Step 5 for this calculation.

Step 8: Calculate extra force on the BS mode due to the coupling with heat bath.

Step 9: Calculate Coulomb force between charges and forces due to applied electric field.

Step 10: Perform ***Nord5_Step2*** to update coordinates, velocities and higher order derivatives for all particles in the current subdomain as all the forces involved have been calculated.

Step 11: Update particles neighbor list with coordinates obtained in Step 10 and go back to Step 1.

6.3 Results and Discussion

Preliminary results were obtained by parallel MD simulation on 8.3 mM lysozyme aqueous solution under three different electric fields (10^5 V/m, 10^6 V/m and 10^7 V/m) and the irradiation PIRL fulence 1 J/cm^2 with each lysozyme chain singly charged. The ablation process was simulated up to 1.15 ns after the incident laser pulse with the irradiation pulse having a Gaussian temporal power profile. The energy of the pulse was converted into number of photons in order to deposit photon energy into the heat bath of the absorbing molecules at each integration time step. The time profile of number of deposited photons is shown in Figure 6.3.1 showing a Gaussian distribution with the peak around 250 ps and pulse width of 100 ps.

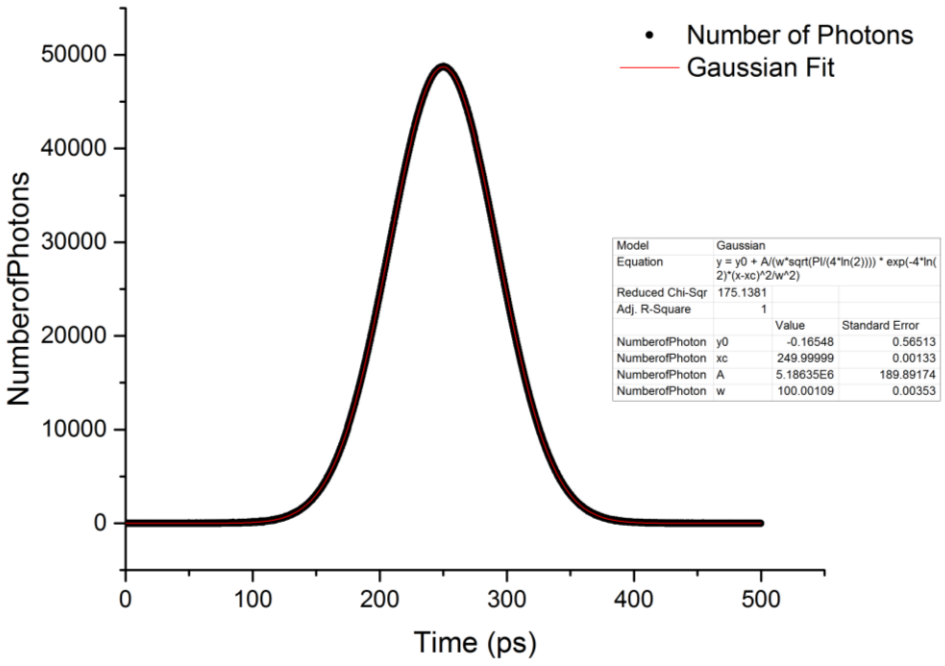

Figure 6.3.1 Time profile of number of deposited photon to the system.

The photon energy was deposited into the heat bath of the absorbing molecules, which was coupled with the breathing mode of the absorbing molecules as well as the corresponding neighboring molecules. In the meantime, the breathing mode was coupled with the mode for the translational motion. Thus, the system's temperature associated with the translational motion (*Ttrs*), breathing motion (*Tbs*) and heat bath (*Thb*) must evolve with the photon deposition.

Figure 6.3.2 shows the evolution of *Ttrs*, *Tbs* and *Thb* with the ablation under electric field of 10^7V/m. In Figure 6.3.2, the heat bath temperature *Thb* (green line) rapidly increased reaching its maximum around 300 ps, which was a 50 ps delay from the peak of deposited photon energy. Since heat bath and breathing mode were coupled together, the breathing sphere motion temperature *Tbs* (purple line) followed the trend of *Thb* with a slight delay in the rising edge. The two temperatures finally converged with each other with the absorbed energy transferred to the translational motion which is coupled with the breathing motion, leading to the ablation and plume formation. As a consequence, the translational motion temperature (*Ttrs*, black line) increased sharply first and then gradually reaching to about 4000 K at *t = 1 ns*. Note that the collective velocity was not excluded during the calculation of *Ttrs*. *Ttr* is thus simply a measure of total kinetic energy of the plume, not really the thermal translational temperature.

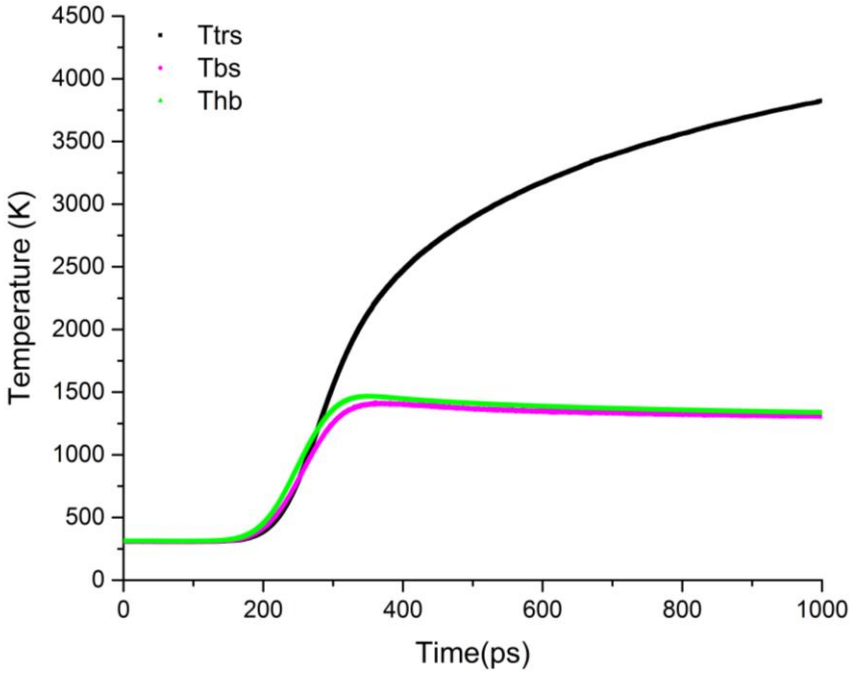

Figure 6.3.2 System temperature evolution of ablation under electric field of 10^7 V/m. Black curve: system's temperature associated with the translational motion; purple curve: system's temperature associated with breathing motion; green curve: system's temperature associated with heat bath.

The contour plot of the temporal evolution of temperature corresponding to the thermal translational motion (motion relative to the center-of-mass of each molecule) *Ttr* (here the collective velocity was removed for the calculation of *Ttr* of each layer) along the plume expansion direction is shown in Figure 6.3.3. The front layer of the plume moved 1500 nm within 1.15 ns, which means the plume expanded at velocity of 1300 m/s, similar to the results

(1500 m/s) obtained by continuous simulation of liquid water under a slightly lower fluence (0.7 J/cm2)[12]. The thermal kinetic temperature Ttr started to increase at 200 ps followed by a peak around 1300 K at 500 ps, then it gradually decreased due to the plume expansion

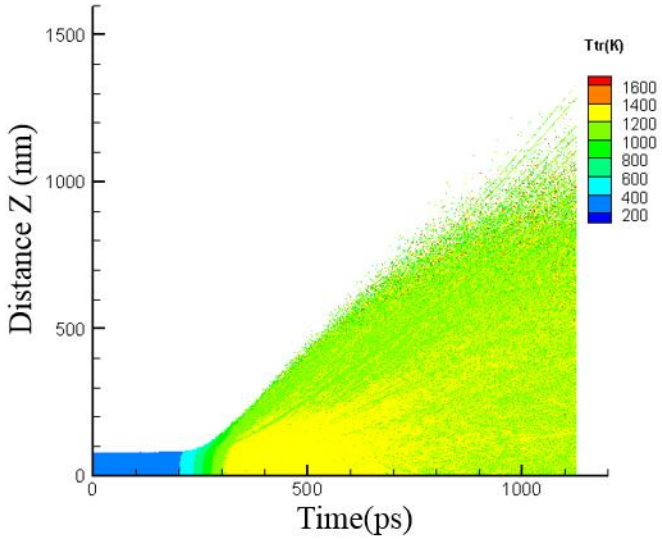

Figure 6.3.3 Contour plot showing Temperature spatial-temporal evolution of ablation under electric field 10^7 V/m.

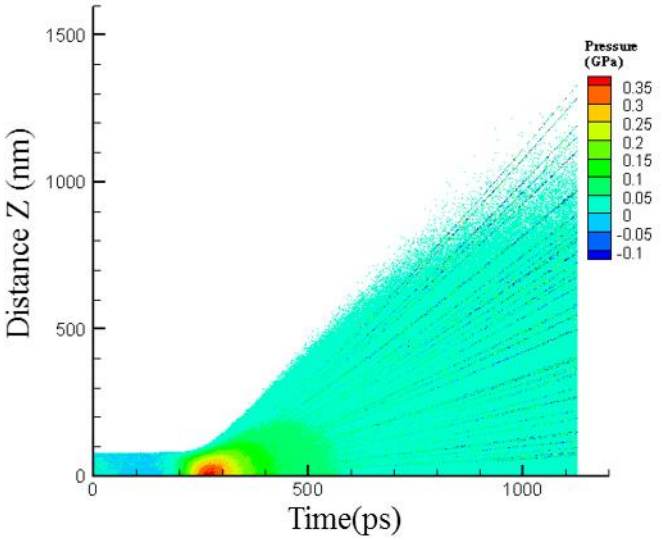

Figure 6.3.4 Counter plot of Pressure spatial-temporal evolution of ablation under electric field of 10^7 V/m.

The contour plot of the system pressure spatial-temporal evolution is shown in Figure 6.3.4. The laser irradiation was along Z positive direction, thus the pressure in the bottom of the system

rapidly built up to 0.35 GPa at *t ~ 270 ps*, which initiates the expansion of the top layers with lower pressure (0 ~ 0.05 Gpa). The system pressure gradually reduced due to the plume expansion.

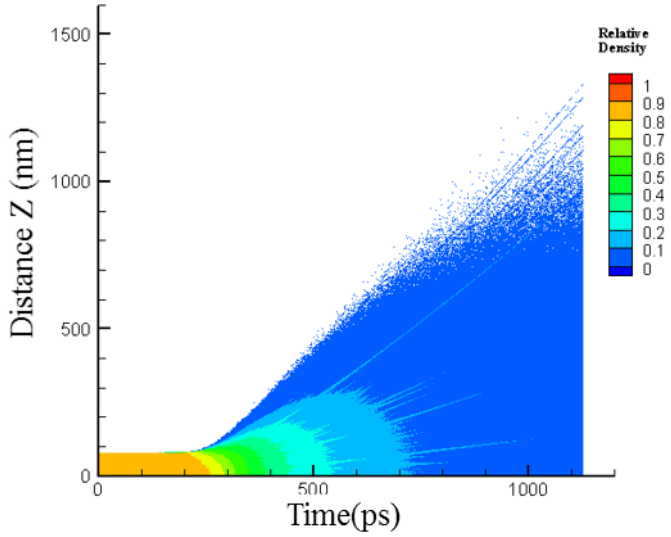

Figure 6.3.5 Counter plot of Density spatial-temporal evolution of ablation under electric field of 10^7 V/m.

The density spatial-temporal evolution is shown in Figure 6.3.5. The density is calculated relative to that of pure liquid water at 300 K at zero pressure. It can be seen in 6.3.5 that the density of the system was initially kept around 0.8 until 250 ps and then decreased rapidly to <0.05, revealing a rapid phase-transition from condensed phase to vapor phase.

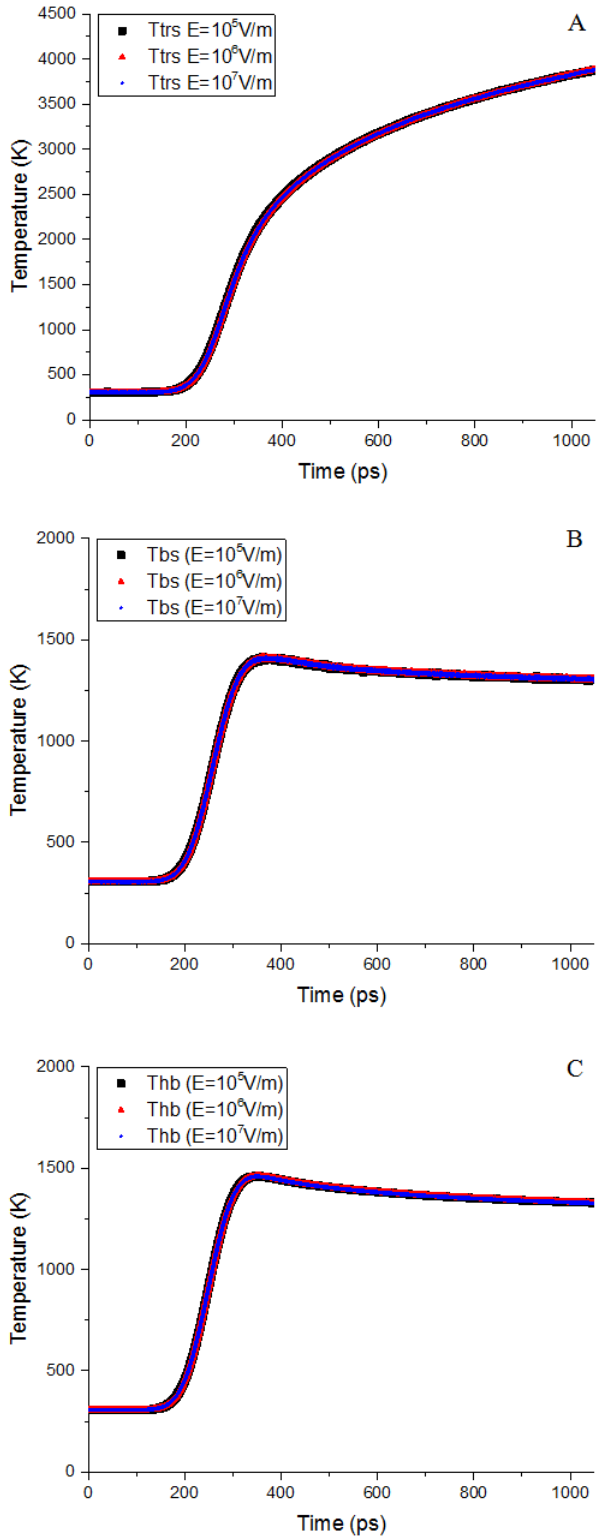

Figure 6.3.6 System's temperature evolution under three different electric field: A: temperature of system total kinetic energy; B: temperature of system breathing motion; C, temperature of system heat bath.

In order to investigate the electric field effect on the ablation process, simulation on the same system under two other different electric field (10^6 V/m, 10^5 V/m) was performed respectively. The system temperature evolution of *Ttrs*, *Tbs*, *Thb* under the three electric field is shown in Figure 6.3.6. From figure 6.3.6, *Ttrs*, *Tbs* and *Thb* follows exactly the same evolution under the three different electric field. This might be because compared to ~ 1 million of neutral BS water, there are only 140 positive ions and 140 negative ions in the system. The number of ions that can be affected by electric field is so small that the effect of the electric field cannot be revealed by the character of the entire plume.

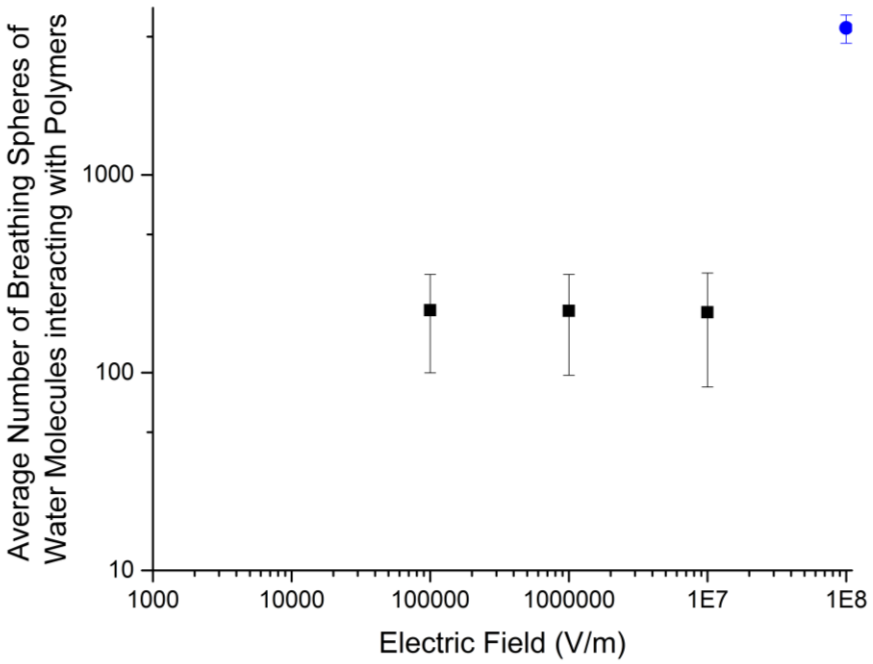

Figure 6.3.7 Average number of interacting water molecules around lysozyme at 1.15 ns after laser incidence under different electric field. The blue dot indicates the initial value of this number before laser irradiation.

As a result of ablation, the number of water molecules interacting with lysozyme was also reduced as the plume propagated. The average number of interacting water molecules around the 140 lysozyme polymer at *t = 1.15 ns* under three different electric fileds is shown in Figure 6.3.7, with the blue dot indicates the value of the same parameter before laser irradiation. It can be seen in Figure 6.3.7 that there were initially ~ 5000 water molecules within the interaction distance with lysozyme while the number reduced to ~ 300 at 1.15 ns after laser incidence. The number of interacting water molecules around lysozyme at 1.15 ns wasn't affected by the applied

electric field, further implying the ablation process in this phase is dominated by laser irradiation rather than the electric field.

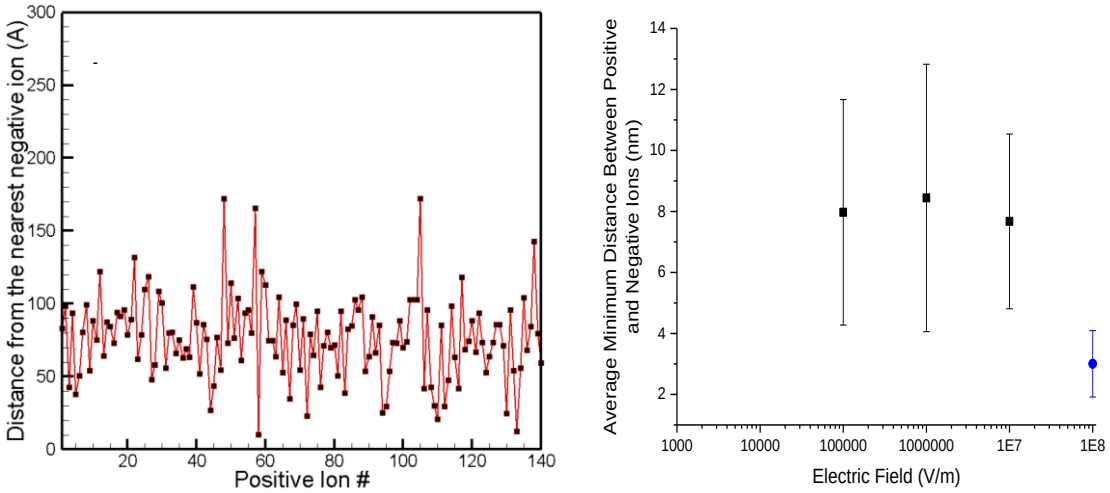

Figure 6.3.8 Distance between positive ion and nearest negative ion: A, distance from the nearest negative ion to each positive ion at $t = 1.15$ ns, $E=10^7$ V/m; B, average distance from the nearest negative ion to positive ion at 1.15 ns of three different electric field, the blue dot is the average of the same value before laser irradiation.

To look at the ions' reaction to the applied electric field, we further analyzed the minimum distance between each positive ion to its nearest ion under three different electric field, and the results are shown in Figure 6.3.8. Figure 6.3.8A is the distance between each positive ion and its nearest negative ion under electric field $E = 10^7$ V/m with the average distance between positive and negative ions around 8.0 nm. The statistics of this distance are shown in Figure 6.3.8B with all the three electric field with the blue dot in the graph is the average of this distance before laser irradiation. Figure 6.3.8B shows, as the plume propagates, the distance between positive and negative ions are increased, whereas this enlargement doesn't seem to be due to the electric field, but more likely due to the perturbation of the laser irradiance. As discussed above, the plume expands at a velocity about 1300 m/s with displacement of molecules position within 1 ns to be around 1 μm, whereas for a singly charged polymer like lysozyme with mass 14319 Da, an electric field of 10^7 V/m applied on such a molecule for only 1 ns will only change its position along z direction a few nm. Thus the electric field effect on positive ions are negligible at this stage of ablation. Singly charged water molecules are more strongly affected by the electric field due to its lighter mass 50 Da compared to lysozyme. However, the electric field is applied along the plume expansion direction (Z positive in counterplots) resulting in an electric force towards Z

negative direction on the negatively charged water molecules. This means the electric force is trying to pull the 140 negatively charged water molecules to move backwards among a crowd of ~1 million neutral water molecules, moving forward at a speed of 1300 m/s. The interaction between charged water molecules with neighbor neutral water molecules will dominate the Coulomb force as the number of neutral water molecules are overwhelming. Thus the effect of electric field on the ion separation cannot be revealed in this stage of ablation. However, if the simulation continues to longer time delay after laser irradiation where the plume expands further, the electric field effect may be observable since with much lower density plume, the inter-molecular interaction between negative charged water molecules and neutral water molecules is weaker and the charge can feel much stronger effective electric field due to the reduction of dielectric constant.

6.4 Conclusion

The ablation process in ionic solution driven by PIRL laser irradiation was performed with parallel MD simulation under three different electric field up to 1ns after laser incidence. The plume expands at a velocity of 1300 m/s with a thermal kinetic temperature about 1000 K. Pressure of 0.35 Gpa was built up in the bottom of the system initiating plume expansion. Both temperature and density of the plume decreased as the ablation proceeded. The number of interacting water molecules around a charged lysozyme was reduced from ~5000 before laser irradiation to ~ 300 at 1.15 ns after laser incidence. The distance between the charged lysozyme and the nearest negatively charged water molecules increased from ~ 3 nm before laser irradiation to ~ 8 nm at 1.15 ns after laser incidence. The effects of electric field is not observable from the simulation results of the system temperature, pressure or density as well as the distance between positive ions and nearest negative ions, indicating the ablation at this stage is dominated only by the perturbation of deposited laser energy. Further simulations in latter stages of the ablation as well as ablation without electric field or under electric field along direction opposite to plume expansion need to be done to investigate the effects of electric field in terms of separating charges critical to charge detection. There is a possibility that the PIRL driven ablation process itself is already vigorous enough to shake off the counter ions from the charged polymer, which will simplify the design for quantitative mass spectrometer based on this ablation mechanism. The great reduction of water molecules surrounding the protein in just 1 ns illustrates the excitation of the water is sufficient to strip the water solvation shell from the

proteins. The question is whether all the waters will be unbound at some point in the expansion as the system is undergoing adiabatic cooling. The present results suggest so in which case the proteins inherent charge state will suffice for mass spectrometry detection and PIRL-DIVE will emerge as a quantitative mass spectrometry method. The implications in dramatically increasing the sensitivity of mass spectrometry by several orders of magnitude is evident and will be greatly assisted by more extensive MD calculations

References of Chapter 6

[1] M. Karas and F. Hillenkamp, “Laser Desorption Ionization of Proteins with Molecular Masses Exceeding 10000 Daltons,” *Anal. Chem.*, vol. 60, no. 20, pp. 2299–2301, Oct. 1988.

[2] K. Tanaka, H. Waki, Y. Ido, S. Akita, Y. Yoshida, T. Yoshida, and T. Matsuo, “Protein and polymer analyses up to m/z 100 000 by laser ionization time-of-flight mass spectrometry,” *Rapid Commun. Mass Spectrom.*, vol. 2, no. 8, pp. 151–153, Aug. 1988.

[3] J. B. Fenn, M. Mann, C. K. Meng, S. F. Wong, and C. M. Whitehouse, “Electrospray ionization for mass spectrometry of large biomolecules,” *Science*, vol. 246, no. 4926, pp. 64–71, Oct. 1989.

[4] J. Fenn, M. Mann, C. Meng, S. Wong, and C. Whitehouse, “ELECTROSPRAY IONIZATION-PRINCIPLES AND PRACTICE,” *MASS Spectrom. Rev.*, vol. 9, no. 1, pp. 37–70, Jan. 1990.

[5] P. James, “Protein identification in the post-genome era: the rapid rise of proteomics,” *Q. Rev. Biophys.*, vol. 30, no. 04, pp. 279–331, Nov. 1997.

[6] M. P. Pavlou, E. P. Diamandis, and I. M. Blasutig, “The Long Journey of Cancer Biomarkers from the Bench to the Clinic,” *Clin. Chem.*, vol. 59, no. 1, pp. 147–157, Jan. 2013.

[7] I. E. deVera, J. E. Katz, and D. B. Agus, “Clinical proteomics: the promises and challenges of mass spectrometry-based biomarker discovery,” *Clin. Adv. Hematol. Oncol. HO*, vol. 4, no. 7, pp. 541–549, Jul. 2006.

[8] S.-E. Ong and M. Mann, “Mass spectrometry-based proteomics turns quantitative,” *Nat. Chem. Biol.*, vol. 1, no. 5, pp. 252–262, Oct. 2005.

[9] M. Bantscheff, S. Lemeer, M. M. Savitski, and B. Kuster, “Quantitative mass spectrometry in proteomics: critical review update from 2007 to the present,” *Anal. Bioanal. Chem.*, vol. 404, no. 4, pp. 939–965, Sep. 2012.

[10] A. Leitner and W. Lindner, “Current chemical tagging strategies for proteome analysis by mass spectrometry,” *J. Chromatogr. B*, vol. 813, no. 1–2, pp. 1–26, Dec. 2004.

[11] M. Constapel, M. Schellenträger, O. J. Schmitz, S. Gäb, K. J. Brockmann, R. Giese, and T. Benter, “Atmospheric-pressure laser ionization: a novel ionization method for liquid chromatography/mass spectrometry,” *Rapid Commun. Mass Spectrom.*, vol. 19, no. 3, pp. 326–336, Feb. 2005.

[12] K. Franjic and R. J. D. Miller, “Vibrationally excited ultrafast thermodynamic phase transitions at the water/air interface,” *Phys. Chem. Chem. Phys.*, vol. 12, no. 20, pp. 5225–5239, 2010.

[13] N. Forsgard, M. Salehpour, and G. Possnert, “Accelerator mass spectrometry in the attomolar concentration range for 14C-labeled biologically active compounds in complex matrixes,” *J. Anal. At. Spectrom.*, vol. 25, no. 1, pp. 74–78, Dec. 2009.

[14] M. E. Belov, M. V. Gorshkov, H. R. Udseth, G. A. Anderson, and R. D. Smith, “Zeptomole-sensitivity electrospray ionization--Fourier transform ion cyclotron

resonance mass spectrometry of proteins," *Anal. Chem.*, vol. 72, no. 10, pp. 2271–2279, May 2000.

[15] R. Knochenmuss and L. V. Zhigilei, "Molecular dynamics simulations of MALDI: laser fluence and pulse width dependence of plume characteristics and consequences for matrix and analyte ionization," *J. Mass Spectrom. JMS*, vol. 45, no. 4, pp. 333–346, Apr. 2010.

[16] H. Lodish, A. Berk, S. L. Zipursky, P. Matsudaira, D. Baltimore, and J. Darnell, "Intracellular Ion Environment and Membrane Electric Potential," 2000.

[17] R. Milo, "What is the total number of protein molecules per cell volume? A call to rethink some published values," *Bioessays*, vol. 35, no. 12, pp. 1050–1055, Dec. 2013.

[18] E. Leveugle and L. V. Zhigilei, "Molecular dynamics simulation study of the ejection and transport of polymer molecules in matrix-assisted pulsed laser evaporation," *J. Appl. Phys.*, vol. 102, no. 7, p. 074914, Oct. 2007.

[19] L. V. Zhigilei, P. B. S. Kodali, and B. J. Garrison, "Molecular Dynamics Model for Laser Ablation and Desorption of Organic Solids," *J. Phys. Chem. B*, vol. 101, no. 11, pp. 2028–2037, Mar. 1997.

[20] L. V. Zhigilei, E. Leveugle, B. J. Garrison, Y. G. Yingling, and M. I. Zeifman, "Computer simulations of laser ablation of molecular substrates," *Chem. Rev.*, vol. 103, no. 2, pp. 321–348, Feb. 2003.

[21] "Computer Simulation of Polymers by E A Colbourn, Editor.: Longman Scientific & Technical 9780582083745 Hard Cover, First Edition. - Mollie's Loft Books." [Online]. Available: http://www.abebooks.com/Computer-Simulation-Polymers-Colbourn-Editor-Longman/8275077882/bd. [Accessed: 27-Aug-2015].

[22] M. Tabetah, A. Matei, C. Constantinescu, N. P. Mortensen, M. Dinescu, J. Schou, and L. V. Zhigilei, "The Minimum Amount of 'Matrix' Needed for Matrix-Assisted Pulsed Laser Deposition of Biomolecules," *J. Phys. Chem. B*, vol. 118, no. 46, pp. 13290–13299, Nov. 2014.

[23] P. M. Morse, "Diatomic Molecules According to the Wave Mechanics. II. Vibrational Levels," *Phys. Rev.*, vol. 34, pp. 57–64, Jul. 1929.

[24] R. J. Abraham and R. Stõlevik, "The morse curve as a non-bonded potential function," *Chem. Phys. Lett.*, vol. 58, no. 4, pp. 622–624, Oct. 1978.

[25] Y. G. Yingling, L. V. Zhigilei, and B. J. Garrison, "The role of the photochemical fragmentation in laser ablation: a molecular dynamics study," *J. Photochem. Photobiol. Chem.*, vol. 145, no. 3, pp. 173–181, Dec. 2001.

[26] B. Gavish, E. Gratton, and C. J. Hardy, "Adiabatic compressibility of globular proteins," *Proc. Natl. Acad. Sci. U. S. A.*, vol. 80, no. 3, pp. 750–754, Feb. 1983.

[27] W. M. Jacobs, D. A. Nicholson, H. Zemer, A. N. Volkov, and L. V. Zhigilei, "Acoustic energy dissipation and thermalization in carbon nanotubes: Atomistic modeling and mesoscopic description," *Phys. Rev. B*, vol. 86, no. 16, p. 165414, Oct. 2012.

[28] R. Diller, "Vibrational relaxation during the retinal isomerization in Bacteriorhodopsin," *Chem. Phys. Lett.*, vol. 295, no. 1–2, pp. 47–55, Oct. 1998.

[29] L. Bu and J. E. Straub, “Simulating Vibrational Energy Flow in Proteins: Relaxation Rate and Mechanism for Heme Cooling in Cytochrome c,” *J. Phys. Chem. B*, vol. 107, no. 44, pp. 12339–12345, Nov. 2003.

[30] H. Fujisaki and J. E. Straub, “Vibrational energy relaxation in proteins,” *Proc. Natl. Acad. Sci. U. S. A.*, vol. 102, no. 19, pp. 6726–6731, May 2005.

[31] G. T. Ibragimova and R. C. Wade, “Importance of Explicit Salt Ions for Protein Stability in Molecular Dynamics Simulation,” *Biophys. J.*, vol. 74, no. 6, pp. 2906–2911, Jun. 1998.

[32] D. Frenkel and B. Smit, Eds., *Understanding Molecular Simulation: From Algorithms to Applications*, 1st ed. Orlando, FL, USA: Academic Press, Inc., 1996.

[33] R. Knochenmuss and L. V. Zhigilei, “Molecular Dynamics Model of Ultraviolet Matrix-Assisted Laser Desorption/Ionization Including Ionization Processes,” *J. Phys. Chem. B*, vol. 109, no. 48, pp. 22947–22957, Dec. 2005.

[34] M. P. Allen and D. J. Tildesley, *Computer Simulation of Liquids*. Clarendon Press, 1989.

[35] W. Mattson and B. M. Rice, “Near-neighbor calculations using a modified cell-linked list method,” *Comput. Phys. Commun.*, vol. 119, no. 2–3, pp. 135–148, Jun. 1999.

Chapter 7
Summary and Prospects

In this work, Picosecond Infrared Lasers (PIRL) was firstly applied to ablate various types of tissues, including pure liquid water, frozen ice layer, 2% agarose gel, pig skin and tendon. Dark field imaging of the plume dynamics on these tissues reveals the ablation started with gas phase molecules followed by ejections of particulates in water rich samples. In samples with less water fraction, the plume is mostly composed by small droplets and particulates. If post photon-ionization of the ablated molecules is under consideration for the design of new ion sources, the fluence of the PIRL laser needs to be selected to maximize the vapor portion in the ablation plume. If the ejected molecules/droplets/particulates are subjected under other ion sources such as electrospray, the fluence of PIRL pulse needs to be adjusted for the finest particulate ejection to maximize the interaction area of the particulates with the ion source.

The PIRL system was further modified to develop an Imaging Mass Spectrometer with the ion source named as PIR-LAESI. The ion source showed its ability to ionize molecules from small drugs such as Reserpine (*m = 608.9 Da*) to large molecules such as proteins, e.g. Cytochrome C (*m ~ 12000 Da*). Characterization on PIR-LAESI proved a limit of detection of 100 nM on reserpine aqueous solution, which is 7.5 times lower than the conventional nanosecond version of LAESI under similar conditions. Imaging on standard samples made by 2% Agarose gel with 100 μM Rhodamine640 indicated the lateral spatial resolution of PIR-LAESI is about 100 μm under current beam focusing conditions. Each pulse can remove 3 ~ 4 μm layers of 2% Agarose gel, and 30 ~ 40 μm layers of agarose gel with 100 μM Rhodamine640 provides reproducible ion counts on the mass spectrometer, corresponding to a detection ability in the femtomole range. The interface can be further optimized by applying a nebulizer gas in the electrospray to produce a mist of finer charged droplets. With this improvement, the amount of molecules removed by single pulse could be enough to provide a reproducible mass spectrum, which means the vertical resolution can be down to a few microns, the size of a single cell. This is very important in the application of PIR-LAESI as a promising tool for surgical guidance using iKnife as a comparative example. However, the PIRL scalpel and PIRL-DIVE MS have major advantages over iKnife. PIRL can not only remove layers of single cell, the minimum removal limit in

surgery, but the PIRL-DIVE Imaging MS also can distinguish the removed cell layer as being healthy or sick which is the extreme limit of biodiagnostics.

PIR-LAESI was further applied to image the molecular distribution of biological tissues. The experiments on Zebra leaf showed a spot size of ~ 100 μm, much smaller compared with the commercial nanosecond LAESI interface. Yet, the tissue mapping ability of PIR-LAESI is comparable with the nanosecond LAESI, confirmed by the similar mass spectrum and ion counts of indicator molecules on the same sample as well as the same molecular map quality. Taking into account the smaller size of the hole drilled by PIR-LAESI, there is less amount of ejected leaf material. Therefore, the ionization efficiency of PIR-LAESI is actually higher than nanosecond LAESI.

Molecular imaging of the MRI contrast agent Gadoteridol on mice kidney was constructed by PIR-LAESI and the results were supported by the molecular map imaged by DESI and MALDI on the sample from the same kidney as well as the optical image of the slide stained by H&E. The ability of PIR-LAESI in detecting lipid and proteins also open possibilities of its application in recognize different type of human cancerous tissues. Furthermore, during intraoperative applications, PIR-LAESI could deliver molecular information of the removed tissue without spraying solvent on open wounds as with DESI or burning the tissues as with electrocautery. With the help of a simple contrast agent, PIR-LAESI can further allow the surgeons “smell” what is inside the plume of ablated tumors targeted with exogenous imaging agents. While effective cutting of bone and tooth enamel have been reported by PIRL, the ability of tissue mapping with PIR-LAESI on tissues possessing different water content is going to be further explored.

PIRL has shown much less scar tissue formation in pork skin in comparison with microsecond IR lasers, but as far as I know there is no such comparison with nanosecond IR lasers at the same wavelength. A complete comparison between PIRL and nanosecond IR laser will be studied via experiments on the plume dynamics of ablations of various samples under the same irradiation fluence. The size of the ablation crater will also be under investigation to compare the wound introduced by the two lasers. Tissue imaging experiments will also be done on different animal tissues by the two lasers to see if PIR-LAESI can produce different molecule information than commercial nanosecond LAESI.

The ablation process driven by PIRL laser on ionic polymer water solution was also studied by parallel molecular dynamics simulation with the inclusion of an applied electric field. The simulation shows a fast plume expansion in the first ns after laser incidence. The number of interacting water molecules with polymer reduced along with the plume expansion, indicating a desorption process of the large polymer molecules. With simulation extended to longer time delays after laser incidence, the desorption efficiency of PIRL driven ablation process can be investigated. The system evolution and the distance between positive and nearest negative ions are not affected by the electric field, indicating at this short time stage (1 ns) the ablation is dominated by the perturbation induced by the laser energy deposition. Further studies of the ablation process without electric field or with electric field applied on the opposite direction will provide us information if external electric field is in need or not to separate counter ions from ionized polymers. This information is the key for the development of an ion source for quantitative mass spectrometer. PIRL-DIVE seems to have the correct attributes to reach this long sought objective.

Copyright Acknowledgements

Here I give my acknowledgement to Dr. Kresimir Franjic for the permission on using his Ph.D thesis “Studies of Laser Ablation of Liquid Water under Conditions of Impulsive Heat Desorption through Vibrational Excitations (IHDVE)”. Part of Chapter 2 in the present thesis is summarized based on his thesis work.